UNIVERSITÀ
DEGLI STUDI
DI PADOVA

DIPARTIMENTO
DI INGEGNERIA
DELL'INFORMAZIONE

DIPARTIMENTO DI INGEGNERIA DELL'INFORMAZIONE

CORSO DI LAUREA IN BIOINGEGNERIA

"Physics-Informed Neural Network per l'inversione di dati di Elastografia di Risonanza Magnetica per la predizione di rigidezza del cervello"

Relatore: Prof. Mattia Veronese

Laureanda: Chiara Da Villa

ANNO ACCADEMICO 2023 – 2024

Data di laurea 04/09/2024

Physics-Informed Neural Network per l'inversione di dati di Elastografia di Risonanza Magnetica per la predizione di rigidezza del cervello

Chiara Da Villa

4 settembre 2024

Contents

1 Abstract

Magnetic resonance elastography (MRE) is a powerful medical imaging technique that allows for the non-invasive assessment of the viscoelastic properties of body tissues, with significant potential as a diagnostic biomarker for various neurological conditions. However, current inversion methods for estimating stiffness from MRE data face challenges related to accuracy, resolution, noise sensitivity, and computational efficiency. This thesis investigates the use of physics-informed neural networks (PINNs) for inverting MRE data to estimate brain stiffness, a method that combines the benefits of deep learning with the incorporation of physical knowledge to enhance accuracy and reduce noise sensitivity.

The proposed method is first applied to a simple phantom dataset (training study) and then to in vivo human brain MRE data (testing study). The impact of including prior stiffness estimates and anatomical information from T1-weighted magnetic resonance imaging (MRI) into the PINN will be evaluated. Additionally, two optimization algorithms, Learning Rate Annealing and Multiadam, are developed to improve computational efficiency and reduce costs.

Results demonstrate that the novel methods significantly outperform traditional direct and finite element inversion techniques in terms of accuracy across both studies (MAV = 277.00 for PINN vs. MAV = 1117.87 and MAV = 561.19 for two other methods). Including anatomical information enhances performance, particularly in models assuming heterogeneous tissue properties (R^2 = 0.87 when included, R^2 = 0.62 when not), while incorporating prior stiffness estimates shows potential for accelerating convergence. MultiAdam reduces the computational time required for training compared to the commonly adopted Adam (8.6 h vs. 24 h).

However, challenges remain in accurately modeling the complex biomechanics of brain tissue. While the approach demonstrates promise, this work underscores the need for further research to develop more suitable physical models for brain MRE and to enhance the efficiency and reusability of PINN-based inversions for clinical feasibility.

L'elastografia a risonanza magnetica (MRE) è un'importante tecnica di imaging medicale che permette di valutare, in modo non invasivo, le proprietà viscoelastiche dei tessuti corporei, con un buon potenziale come biomarcatore diagnostico per diverse condizioni neurologiche. Tuttavia, i metodi di inversione attualmente utilizzati per stimare la rigidità dai dati MRE presentano difficoltà significative legate all'accuratezza, alla risoluzione, alla sensibilità al rumore e all'efficienza computazionale. Questa tesi testa l'applicazione di physics-informed neural networks (PINNs) per l'inversione dei dati MRE e la stima della rigidità cerebrale, un approccio che combina i vantaggi del deep learning con l'inclusione di conoscenze fisiche per migliorare l'accuratezza e ridurre la sensibilità al rumore.

Il metodo proposto è stato inizialmente applicato a un semplice dataset di phantom (training study) e successivamente ai dati MRE del cervello umano in vivo (testing study). È stato valutato l'effetto dell'integrazione in una PINN di stime precedenti di rigidità e di informazioni anatomiche derivate dalla risonanza magnetica pesata in T1. Inoltre, sono stati sviluppati due algoritmi di ottimizzazione, Learning Rate Annealing e Multiadam, per migliorare l'efficienza computazionale e ridurre i costi.

I risultati dimostrano che i nuovi metodi superano in modo significativo le tradizionali tecniche di inversione diretta e agli elementi finiti in termini di accuratezza in entrambi gli studi (MAV = 277,00 per PINN contro MAV = 1117,87 e MAV = 561,19 per altri metodi). L'inclusione di informazioni anatomiche migliora le prestazioni, soprattutto nei modelli che assumono proprietà dei tessuti eterogenee ($R^2 = 0,87$ se inclusa, $R^2 = 0,62$ se non inclusa), mentre l'inclusione di stime precedenti di rigidità può potenzialmente favorire una convergenza più rapida. L'algoritmo MultiAdam riduce il tempo di calcolo necessario per l'addestramento rispetto al comunemente usato Adam (8,6 ore contro 24 ore).

Tuttavia, sono presenti delle limitazioni nel modellare accuratamente la complessa biomeccanica del tessuto cerebrale. Sebbene l'approccio proposto sia promettente, questo lavoro evidenzia la necessità di ulteriori ricerche per sviluppare modelli fisici più adeguati per la MRE cerebrale e per migliorare l'efficienza e il riutilizzo dei metodi di inversione tramite PINN, in vista di una loro applicabilità clinica.

2 Introduction and Project Aim

The clinical importance of understanding the stiffness properties of biological tissues has been recognized historically. Traditionally, these have been assessed qualitatively with palpation, limited to superficial regions and applicable in late disease stages, or quantitatively with the low cost and widely available ultrasound (US) technique [1]. Since the late 1990s, Magnetic resonance elastography (MRE), thanks to its ability to measuring stiffness parameters with a high sensitivity, has started to see numerous applications, quantifying also viscous behavior, in deeper tissues and with a larger and movable field of view.

MRE is a powerful medical imaging technique that allows for the non-invasive assessment of high spatial resolution viscoelastic properties of body tissues, such as storage and loss moduli. It uses a special sequence of magnetic resonance imaging (MRI) and additional equipment to generate low frequency mechanical vibrations in the body. The vibrations move through stiff and supple tissues at different rates and with different attenuations: tissue displacement is imaged through a phase-contrast mechanism, and a map of viscoelastic parameters can be reconstructed by mathematically solving an inverse problem.

MRE has great potential as a diagnostic biomarker. For instance, mechanical properties measured by this technique were shown to be significantly altered in neurological diseases such as Alzheimer's disease (AD) and Parkinson's disease (PD) [2] [3]. It also allows accurate assessment of tumors adhesion and their differentiation [4]. Nevertheless, additional equipment, time consuming estimation of the stiffness maps, ill-posedness and nonuniqueness solution of the inverse problem, low resolution and noise sensitivity of techniques makes conducting research in this field particularly challenging.

To estimate the stiffness map, one typically has to either resort to direct inversion (DI) methods [5] [6], that are fast but require several assumptions to reduce the complexity of wave equations, such as homogeneity, and use Laplacian operators that amplify noise; or one creates a more robust model with the use of a finite element model (FEM) with fewer assumptions and proceeds iteratively with a Nonlinear Inversion (NLI), which is computationally very costly, takes hours to converge and is not practically suitable in routine clinical MRE [4] [7].
For these reasons, there is a strong need for advanced inversion algorithms to estimate tissues stiffness, capable of relaxing tissue homogeneity hypothesis while maintaining efficiency, clinical feasibility, good resolution, and numerical stability. Some research groups have recently started to solve the inversion problem with artificial neural networks (ANNs) [8] [9] [10], and

have shown it has better accuracy and is more clinically feasible than traditional methods. Moreover, many studies are focusing on understanding how the assumption of material stiffness homogeneity worsens the spatial accuracy and noise sensitivity of estimates made by ANN [11] .

In this project, the attempt will be to boost the accuracy of a neural network-based inversion method by training on real brain MRE data, with the addition of imposing physics informed constraints on the inversion using so called physics informed neural networks (PINNs). Ragoza and Batmanghelich recently published open-source code where they implemented such a method for MRE-PINN inversion of the liver, incorporating information from anatomical images and using a dual-network approach [10]. The inversion method has shown promising results in the liver tissues: in this thesis, the algorithm provided by Ragoza's reference study will be first implemented and adapted in a training study on a MRE phantom, and then applied to a testing study, where the model will be trained on a cohort of brain tissues in an attempt to create a MRE PINN-based inversion algorithm to retrieve brain tissue stiffness maps. Data for the testing study are imported from the open - source MRE dataset from Neuroimaging Tools and Resources Collaboratory (NITRC) site, made by the University of Delaware (UDEL) and will be indicated as Delaware dataset [1].

In order to invert MRE data, a physics model should be formulated describing waves propagation in the tissue of interest. For the brain, the equation of a harmonic motion with linear, isotropic stress-strain relation and the assumption of incompressibility will be adopted. In practice, two partial differential equations (PDE) will be employed in this work: one assuming local homogeneity of viscoelastic parameters (homogeneous PDE) and one taking into account its local variations (heterogeneous PDE). Both homogeneous and heterogeneous models will be tested to validate previous findings related to the potentially adverse effects of assuming homogeneity. To assess models performances, a set of standard evaluation metrics will be computed, and a visual assessment of the results will be performed.

Different PINN configurations will be investigated. In the reference study, including information from MRI anatomical images improves reconstruction fidelity: T1 weighted (T1w) brain MRI images will be also included in this work to improve reconstruction, as they are standard practice to collect during a MRE exam. PINN can approximate extremely complex functions and are remarkably robust to noise, but the major PINN drawback is the slow training speed and

[1] `https://www.nitrc.org/frs/?group_id=1390`

the computational cost [12]. An hyperparameter analysis and two existing successful weights-adaptive algorithms, different from the commonly adopted Adam optimization, will be implemented to deal with this issue. Both of them will be tested to improve this aspect: Multiadam [13] and Learning Rate annealing [14].

Due to the various limitations and challenges of current state-of-the-art inversion techniques, this approach is expected to provide better accuracy, more efficiency, stability and more robustness to noise than previous ones, since it does not have explicit specification of physical relationships, it does not amplify the noise, [10] and is a suitable approach for a clinical workflow because, once validated and generalized on a set of real patients images, it can be applied to any input image similarly acquired, requiring a simple forward pass through the network. The technique also holds significant potential thanks to PINN's flexibility: by simply modifying the differential equations associated with a body compartment model, this approach can be adapted to invert data from different tissues.

3 Background

This section provides an overview to establish a foundational understanding for the subsequent topics. The section will cover MRE acquisition and processing, followed by a brief overview of its hardware and clinical applications. The final section is a brief explanation of deep learning (DL) and supervised models.

3.1 MRE Acquisition and Processing

In this section, all the steps that lead to a map representing viscoelastic properties through MRE acquisition and processing will be explained, which are illustrated in a flow diagram in Figure 1. Pictures in this diagram are also referenced in Figures 5 and 9. The process begins with mechanical vibrations applied to patient tissues, which are then scanned using MRI. The initial output is a raw phase image that captures the wave propagation within the tissues. The raw phase image is unwrapped, multiple images are acquired at different time offsets along the wave period, motion encoding and Fast Fourier Transform (FFT) techniques are applied to obtain wave images in different spatial directions. In the end, different computational techniques can be used to invert the wave data to compute the viscoelastic properties of the tissues: the result is a map of the viscoelastic parameters, showing the stiffness and elasticity of the tissues. The final viscoelastic maps are used to derive clinical biomarkers that can help in diagnosing and understanding various medical conditions.

3.1.1 Actuation

In MRE acquisitions, mechanical stress is introduced into biological tissues of interest as an oscillating harmonic vibration through an active driver that represents a dynamic source of motion, combined with a transducer, which transmits the mechanical waves into the target tissue. For brain MRE, this is placed underneath the head in the region of interest (ROI) [4] (Figure 2). Hence waves cause tissues to vibrate, which are assumed to experience an harmonic motion on the orders of microns (typically 5–50 μm [15]). A MRE acquisition does not determine directly this motion but measures first magnitude and phase of the displacement field caused by propagating mechanical waves in the tissue.

A specific actuation frequency is set for this harmonic oscillation: for brain scanning, MRE uses frequencies in the range 20-100 Hz and amplitude up to 1 mm at the skin surface [9]. Most common frequencies are 50 Hz and 60 Hz, but a standardised frequency still has not been es-

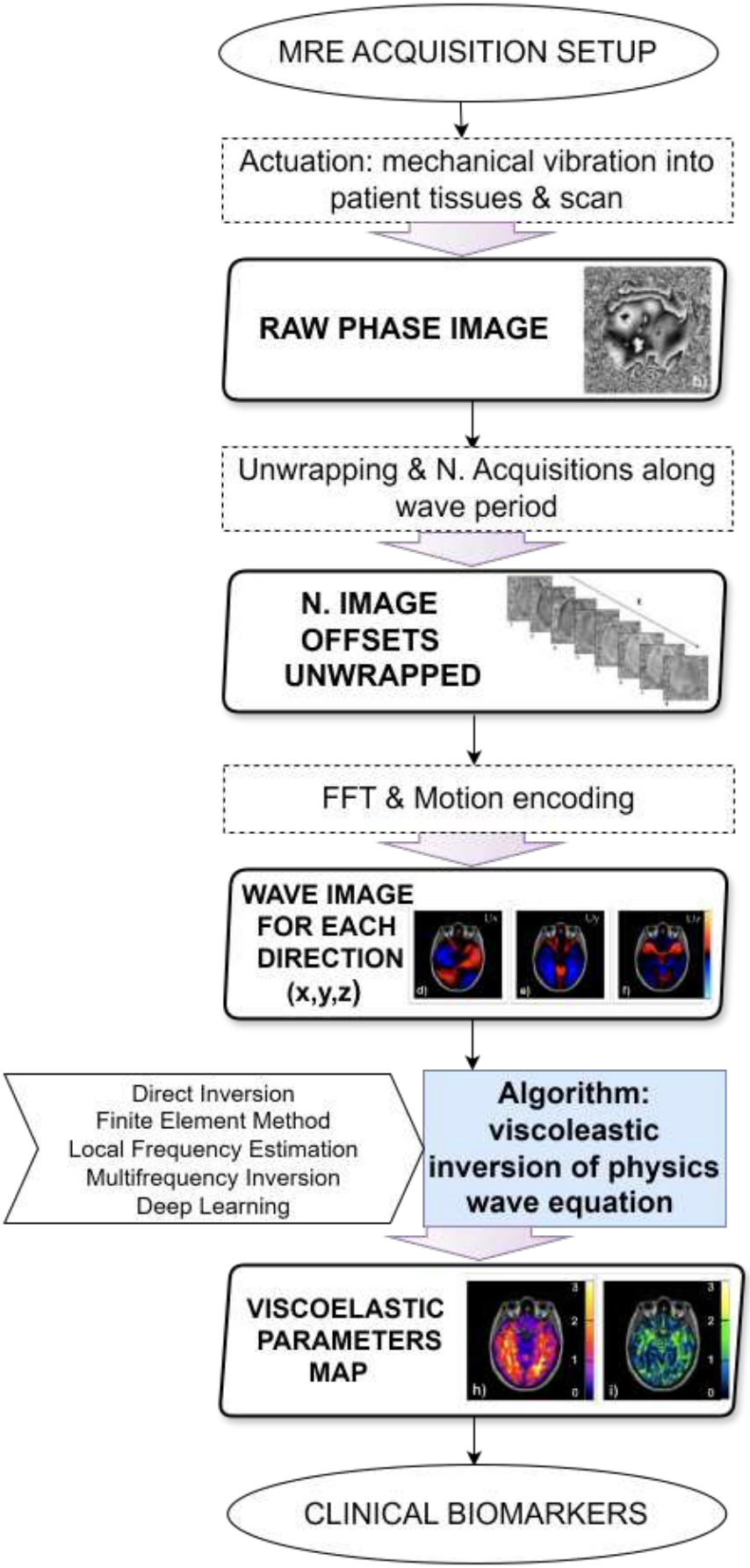

Figure 1: Diagram flow of MRE acquisition and processing.

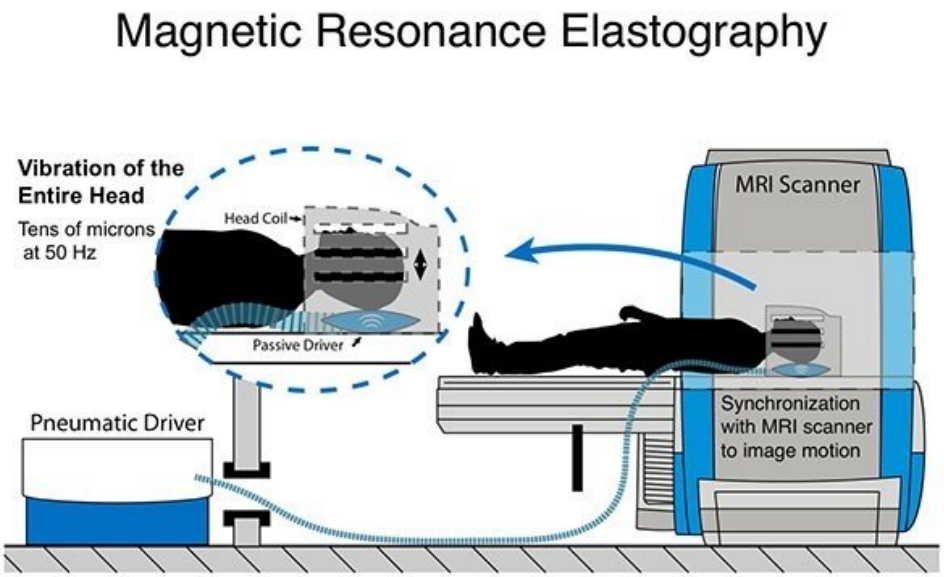

Figure 2: Experimental setup for brain tissue vibration with the Resoundant pneumatic actuator. The subject's head rests on a pillow-like passive driver that receives vibrations from the active driver located in the control room. Adapted from "Simultaneous, multidirectional acquisition of displacement fields in magnetic resonance elastography of the in vivo human brain" by Klatt et al, 2014, John Wiley and Sons.© 2014, Wiley. Used with permission.

tablished.

Higher frequencies waves are attenuated by the brain and for this reason they don't reach deep tissues and produce low displacement amplitude images where noise can dominate; they also necessitate higher amplitudes, which results in greater discomfort for the patient, and can also lead discretization artifacts [15]. But higher frequencies correspond to shorter wavelengths, which provide better spatial resolution and are more informative about the local mechanical properties of the tissues. On the other side, lower frequency vibrations do not attenuate but correspond to longer wavelength and vibrational exposure limits are imposed on these in clinical applications, with the EU whole body vibration limit guidelines [16] serving as a well-established, practical standard.

MRE sequences use traditional MRI ones with addition of motion encoding gradients (MEGs) and set a synchronization between oscillation transmission and signal readout, to encode tissue displacement into the measured signal phase. Both spin echo (SE) and gradient echo (GE) echo-planar imaging (EPI) sequences are commonly applied, thanks to the rapid acquisition of slices [4]. The most common brain MRE sequence is based on single-shot, spin-echo EPI, which allows for short imaging time for acquiring 3D data [2][17].

Some groups are working on finding an efficient MRE multi-shot sequence, where the acquisition is divided into multiple "shots" of excitations in order to improve signal to noise ratio

(SNR) efficiency [18]. In 2013, multi-shot, SE sequence with variable-density spiral readout gradients was introduced in [19]. One year later, the same group improved by capturing whole-brain displacement data at high resolution with a 3D multislab, multishot acquisition for MRE with whole-brain imaging coverage [18]. This sequence is used for Delaware dataset, employed as a testing set in this study. Recently, a rapid simultaneous multi-slice (SMS) MRE has brought accelerated data acquisition in the liver [20].

3.1.2 Single raw phase image and unwrapping

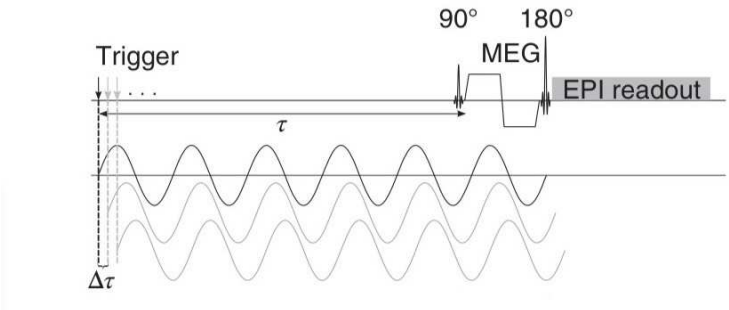

Figure 3: Diagram of a spin echo EPI-MRE sequence. Adapted from "Magnetic Resonance Elastography: Physical Background And Medical Applications", by Hirsch et al, 2016. © 2017 WILEY-VCH Verlag GmbH & Co. KGaA

To first measure a single wave phase image at a single time point, a trigger signal is sent to the vibration generator (Figure 3) ; the vibration propagates into tissues and after a time delay τ a MEG is applied and, through an EPI sequence readout, two images are acquired, phase and magnitude (see diagram in Figure 1). Only the single raw phase image is relevant for processing.

First, a step called phase unwrapping is required to accurate estimate motion [21], because the amplitude of the applied wave, close to tissue surface, should be set large to compensate wave attenuation through depth tissues, but large amplitudes cause the actual wave phase ϕ to be out of the [- π, π] range. In this case, the true phase values will be automatically and unavoidably mapped back to this range when measured, resulting in phase wraps: this produces a strongly discontinuous phase image (Figure 4) where the phase jumps from $-\pi$ to π (or viceversa) [9]. There are different approaches that can be used to remove these wraps in the raw phase image [21] and obtain the physically correct values, such as Flynn's Minimum Discontinuity Algorithm [22][23], Gradient Unwrapping [24] or Laplacian Unwrapping [25].

Signal phase is sensitive to the mechanical vibration applied, but responds also to magnetic field

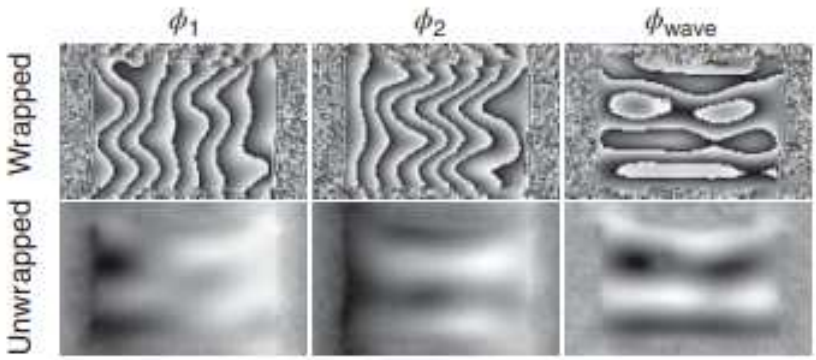

Figure 4: Two raws, wrapped phase images ϕ_2 and ϕ_2 with opposite vibration phase are shown. After unwrapping, each image is a superposition of the propagating wave and the static background. Taking the phase difference image removes most of the background while preserving the wave information. . Adapted from "Magnetic Resonance Elastography: Physical Background And Medical Applications", by Hirsch et al, 2016. © 2017 WILEY-VCH Verlag GmbH & Co. KGaA

inhomogeneities due to a spatially varying magnetic susceptibility. The detected raw phase single image ϕ, in fact, is a superimposition of a static background ϕ_0 and the wave-induced ϕ_{WAVE} contribution of interest: wave information should be isolated. This can be accomplished acquiring more than one phase image in one given MEG direction, as explained in subsequent formulas.

Two raw phase images are acquired so that they depict the wave at two different oscillation phases separated by 180 °, such that the second image contains an inverted sign wave:

$$\phi_1 = \phi_0 + \phi_{\text{WAVE}} \tag{1}$$

$$\phi_2 = \phi_0 - \phi_{\text{WAVE}} \tag{2}$$

By subtracting Equation 2 to Equation 1:

$$\phi_1 - \phi_2 = 2\phi_{\text{WAVE}} \tag{3}$$

Phase component ϕ_{WAVE} containing only wave information can be isolated and extracted from the measured ϕ_1 and ϕ_2 switching to the complex domain:

$$\frac{1}{2} angle\left(\frac{e^{\mathrm{i}\phi_1}}{e^{\mathrm{i}\phi_2}}\right) = \frac{1}{2} angle\left(e^{2\mathrm{i}\phi_{\text{WAVE}}}\right) = \frac{1}{2} angle\left(e^{2\mathrm{i}\phi_{\text{WAVE}}}\right) \tag{4}$$

In practice, more than two raw phase images along the wave period are actually acquired and

FFT is used to extract only the wave component of interest.

3.1.3 Acquisition of multiple (N) phase images along wave period

Image processing of N different raw phase images (usually N=4 or N=8), also called image offsets as they represent phase offset from the zero phase time point, is required to isolate wave information and to proceed with motion encoding.

Different raw phase images are obtained by changing the synchronization between vibration actuation and image acquisition, i.e. by applying (N) different time delays τ_i between the vibration trigger and the MEG in the MRE sequence (see Figure 3). These capture wave propagation at different oscillation phases spaced evenly over the period of the applied wave. Delays τ_i should be applied N times in steps of $\Delta\tau = \frac{1}{(f \cdot N)}$ where f is the mechanical frequency, so that the vibration cycle in equally intermitted in N points (Figure 5).

Subsequently, motion encoding is applied to compute tissue displacements after processing these images offsets. The additional MEG along a certain direction, peculiar of a MRE sequence, allows in fact to encode and compute the displacement created by the mechanical vibration in that direction, when wave phases measured at different time points are avaliable. The phases generated by an harmonically vibrating tissue indeed are directly proportional to its displacements and this linear relation will be presented in Equation 8. After this MEG step, an image showing micron-level displacement represents the coherent wave motion of brain tissues along the MEG direction (see diagram in Figure 1), which is defined as "wave image" along one given direction. Coherent motion is a motion that maintains a constant phase over time.

3.1.4 Fast Fourier Transform and motion encoding

These offsets are unwrapped and a temporal FFT is applied to the image series to extract the first harmonic phase image in the frequency domain (Figure 6). In fact, static inhomogeneity background of magnetic field is contained in the zero-frequency component, while wave information, intrinsically dinamical, falls into the first harmonic frequency image; higher harmonics contain no information because only the first harmonic frequency was stimulated [9]. The measured FF-transformed phase will be indicated as $\tilde{\phi}_i(r)$.
Through phase encoding, amplitude and phase of the complex harmonic displacement at each

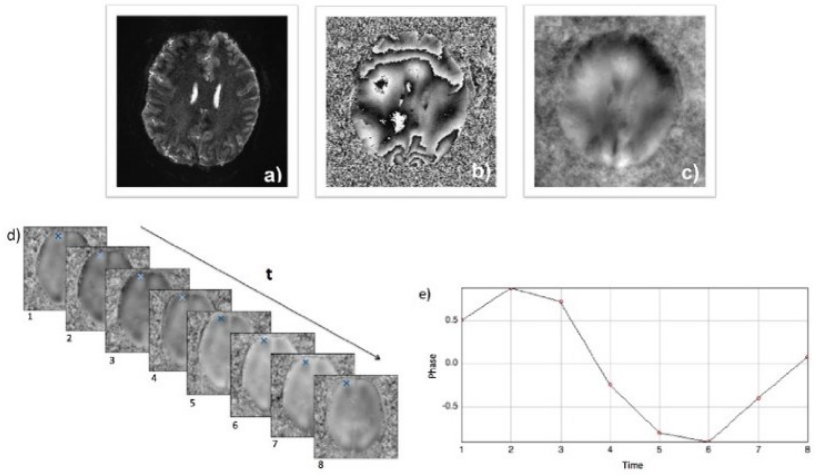

Figure 5: Phase unwrapping. (a) EPI magnitude; (b) EPI raw phase (wrapped) image; (c)EPI raw phase unwrapped image (d) image stack of eight phase offsets unwrapped, for a single brain slice. The blue crosses show the voxel where the phase displacement can be visualised in the corresponding graph (e) change in phase offset over the eight time-steps in one specific voxel, caused by the applied wave propagation. Adapted from "Magnetic resonance elastography (MRE) of the human brain: technique, findings and clinical applications", by Hiscox et al, 2016, Institute of Physics and Engineering in Medicine.© 2016 Physics in Medicine & Biology. Used with permission.

point in space, or its real and imaginary part, are computed. This is relevant for this study because Delaware dataset provides exactly the complex lagrangian displacement components (real and imaginary) in micron over time along the three orthogonal axes, determined from MRE phase after spatial and temporal unwrapping.

MEG can be applied on coronal, sagittal, and transverse directions (Figure 7) to detect the corresponding harmonic motion. A single MRE acquisition is able to capture displacement in only one direction; actually, three MRE acquisitions are usually executed to produce three wave images, indicating the degree of displacement in three orthogonal directions and capturing thus the full 3D wave displacement field.

In this subsection, calculations required to extract a wave image will be briefly outlined.
In the presence of a magnetic field gradient $\mathbf{G}(t)$, a spin with trajectory $\mathbf{x}(t)$ accumulates a phase $\phi(t)$:

$$\phi(t) = \phi(t_0) + \gamma \int_0^t \mathbf{G}(t') \cdot \mathbf{x}(t) dt' \tag{5}$$

where γ is the giromagnetic ratio characteristic of the nuclear isochromats under investigation.
If the spin is stationary, the product $\mathbf{G}(t') \cdot \mathbf{x}(t)$ and the integral of Equation 5 will be zero: spin will have no net phase shift $\phi(t)$, because the gradient is balanced. If a spin is moving in

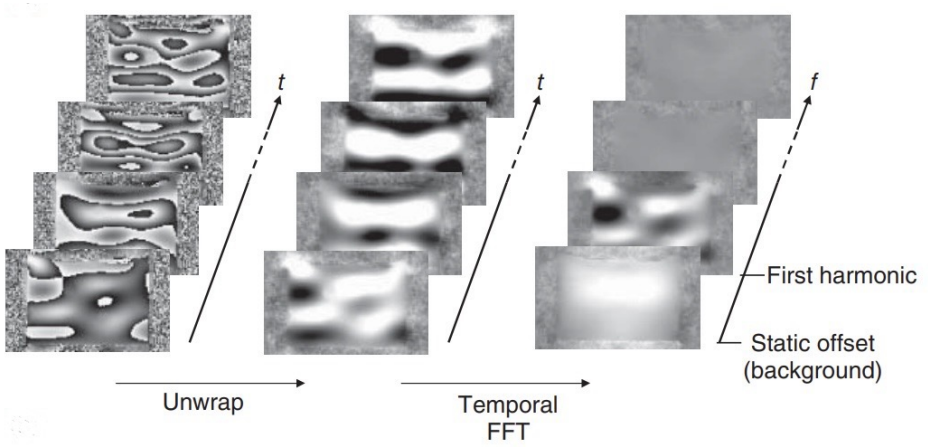

Figure 6: A stack of images, capturing the wave at different phases of the vibration cycle, is first subjected to unwrapping and then temporally Fourier-transformed. In the resulting frequency-resolved representation, the static offset caused by the susceptibility and magnetic field inhomogeneity background is contained in the zero-frequency component, whereas the wave information falls into the first harmonic frequency image. The higher harmonic frequencies contain no information, since only the first harmonic frequency was mechanically stimulated. Adapted from "Magnetic Resonance Elastography: Physical Background And Medical Applications", by Hirsch et al, 2016. © 2017 WILEY-VCH Verlag GmbH & Co. KGaA.

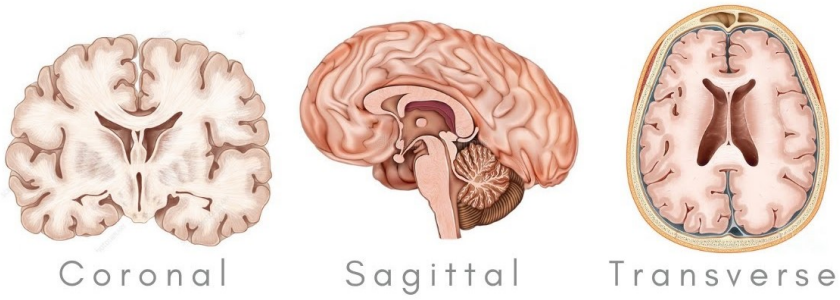

Figure 7: Neuroanatomical planes. Image taken from the video "Title of the Video" by Brainpsychlopedia, YouTube, January 2022, (accessed on August 2024). Available at `https://www.youtube.com/watch?v=peFn_6t9Kms`

synchronization with MEG $\mathbf{G}(t)$ switching, the product $\mathbf{G}(t') \cdot \mathbf{x}(t)$ will not be null and it will accumulate a net phase (Figure 8). Two acquisitions are made for each repetition with reversed MEG polarity to double the sensitivity to small displacements [9].

Assuming now that the net accumulated phase is nonzero, spin motion due to vibration in MRE is hypothesized to be an harmonic oscillation with pulsation Ω, initial and constant, phase ψ and initial polarization direction $\mathbf{u}_0$:

$$\mathbf{x}(t) = \mathbf{x}_0 + \mathbf{u}_0 \cdot sin(\Omega t + \psi) \quad . \quad (6)$$

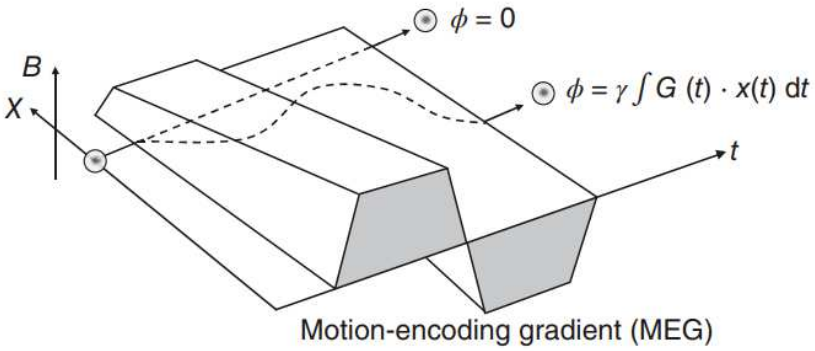

Figure 8: Illustration of phase accumulation for a moving spin in the presence of a MEG in the x-direction. For the static spin, the effects of the positive and negative lobes of the MEG compensate each other, so that the net phase after the MEG is zero. The moving spin experiences the two lobes at different locations, and hence with different strength, so that a net phase remains. Adapted from "Magnetic Resonance Elastography: Physical Background And Medical Applications", by Hirsch et al, 2016. © 2017 WILEY-VCH Verlag GmbH & Co. KGaA.

The total accumulated phase ϕ results to be a function of the oscillation phase ψ:

$$\phi(\psi) = \mathbf{u}_0 \bullet \hat{\mathrm{G}}_0 \int_{-T/2}^{T/2} g(t) \sin(\Omega t + \psi)\, dt \tag{7}$$

Through Equation 7, $\phi(\psi)$ can be easily computed from all these known parameters and values: gradient waveform *g(t)*, oscillation frequency through oscillation pulsation Ω, oscillation amplitude vector $\mathbf{u}_0$ and angle between the gradient and the oscillation polarization ($\hat{\mathbf{u}}_0 \bullet \hat{\mathrm{G}}_0$).

To understand now how to encode motion in the Fourier-transformed phase, the frequency-varying Encoding Efficiency ξ quantity must be introduced, defined as the maximum phase offset caused by the gradient waveform for a vibration with unit amplitude and polarization parallel to the gradient direction [9]. FF-tranformed oscillation amplitude can be derived from the measured FF-transformed phase through ξ from:

$$\tilde{u}_i(\mathbf{r}) = \xi(\mathbf{r})\tilde{\phi}_i(\mathbf{r}) \tag{8}$$

3.1.5 Wave images for each direction (x,y,z)

Collection of phase images across all vibrational phase offsets and in three physical MEG directions gives the full 3D displacement field image (wave images in Figure 9d, 9e, 9f). The local displacement depends on the stress, here represented by the propagating mechanical wave, and on the material stiffness. Waves travel faster in stiffer materials, while their amplitudes are more

attenuated in suppler materials.

Dynamic measures of displacements are the basis for dynamic elastography, that uses knowledge of displacement collected over time to ultimately estimate viscoelastic parameters: these wave images are usually used as input to inversion algorithms in order to obtain a map of viscoelastic properties. As explained in the introduction, the inversion of MRE wave data is the central focus of this thesis.

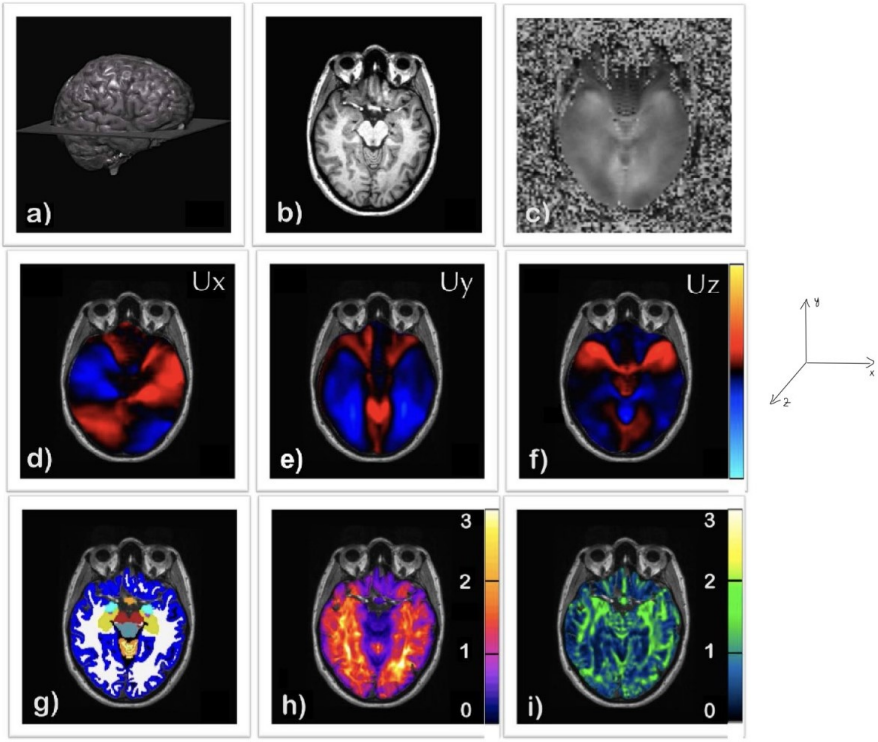

Figure 9: [15] (a) 3D reconstruction T1- weighted brain scan (b) the aforementioned T1 axial slice, (c) raw phase image, (d)–(f) wave images from three directions read-out (x), phase-encode (y), through-plane (z) , indicating the degree of displacement between - 5 µm and 5 µm, (g) segmented image (h) map of $|G^*(kPa)|$ and (i) phase image ϕ_1 (rad). Adapted from ”Magnetic Resonance Elastography: Physical Background And Medical Applications”, by Hirsch et al, 2016. © 2017 WILEY-VCH Verlag GmbH & Co. KGaA.

In Figure 9 [15], the top three images show displacement fields in three spatial directions after the curl operator has been performed to remove longitudinal components. A T1w image is displayed for anatomical reference to the stiffness map of the same brain slice, also called elastogram (Figures 9h and 9i), derived from MRE inversion.

3.1.6 Viscoelastic parameters

In MRE, biological tissues tissues serve as the medium through which waves propagate and attenuate. Mechanical laws and theories are used to model these phenomenons and the following semplifications and assumptions are usually adopted for brain MRE:

- Viscoelastic tissue behaviour: the response to an external force is described by a combination of elastic and viscous terms. The first assumes that the medium deforms when a force is applied but then immediately returns to its original state in a fully reversible process without energy dissipation. Viscosity hypothesis states that the medium does not immediately return to its original shape when force is removed, and work performed during deformation is partially dissipated and not available anymore.
- Infinitesimal strain theory and linear viscoelasticity. Deformations and displacements caused by MRE actuations are small compared to the size of the object. This allows to use linear mechanics formulations and to apply the first order truncation of Taylor series to express the deformation in terms of displacement field derivatives. Furthermore, the mechanical parameters are not dependent on strain or strain rate conditions.
- Isotropy. Mechanical response (i.e., viscoelastic properties) does not depend on the direction along which a force acts. This is considered a reasonable hypothesis for brain tissues.
- Incompressible media, i.e. mass density ρ constant throughout the brain and equal to 1000 kg/m^3. Compression modulus K, indicating how much a material permits volume change for a given pressure, differs little from that of the water (2.2 GPa) [26].
- A fourth-order elasticity tensor $\mathbf{C}$ describes the relationship between stress and strain in a linear elastic material. When deriving wave equations, elastic properties are assumed constant throughout the tissue by discarding the spatial derivative of the $\mathbf{C}$. It is therefore assumed that elastic parameters variation is too small to contribute significantly to the wave equation, making their spatial derivative negligible compared to the variation of displacement amplitudes.

Before describing main viscoelastic MRE parametres, the following notation is introduced that will be adopted:

- strain tensor $\boldsymbol{\epsilon}$
- stress tensor $\boldsymbol{\sigma}$

- shear wave speed (or velocity) ν_s
- wave attenuation coefficient α
- wavelength λ
- applied mechanical frequency of mechanical oscillation f
- applied angular frequency of mechanical oscillation ω
- mass density ρ
- real-valued shear modulus μ, also called Lamè's second parameter
- (complex-valued) shear modulus G^*
- Poisson's ratio ν
- Young modulus E
- Lamè's first parameter λ
- compression modulus K

Two independent constants are sufficient to characterize the elasticity (compliance) tensor of a linear isotropic medium, which is the assumption made here for brain tissues. Parametrizations are usually either (E, ν) or (λ,μ). Through mechanical laws, one can find all the constants defining mechanial behaviour when two of them are known: MRE-scanned tissues are usually descibed by λ and μ. μ is the real-valued shear modulus that quantifies the stiffness of a material in response to shear stress and relates to the material's ability to withstand changes in shape without a change in volume; Lamè's first parameter λ indicates how easily a material can be compressed and relates to volumetric deformation (perfect incompressibility $\lambda = \infty$, perfect compressibility $\lambda = 0$).

Through MRE inversion, spatially varying representation of the following viscoelastic parameters are obtained:

- complex shear modulus G^*, measured in [kPa]. This parameter encapsulates elastic and viscoelastic properties of a medium in a single complex number.
  One can conveniently switch to Laplace domain [9], where G^* (s) represents the ratio of Laplace-transformed stress to strain tensors: $\overline{G^*}(s) = \frac{\bar{\sigma}(s)}{\bar{\epsilon}(s)}$. It is possible to obtain a frequency resolved representation with s = jω, where w is the angular frequency (for $\omega = 0$, properties under static conditions are obtained): $G^*(j\omega)$ indicates that viscoelastic proper-

ties of a material depend on the frequency w of an oscillating strain. Two parametrization are used:

1. $G^*=G'+iG''$. The real part of the shear modulus G' is related to of the mechanical energy stored in the system (storage modulus, kPa) and can also be indicated as μ; the imaginary component G'' is related to the energy dissipated (loss modulus, kPa).

2. $G = |G^*| \cdot e^{i\theta}$, where $\tan(\theta)=\frac{G'}{G''}$. The phase angle θ is a common measure of relative tissue viscosity; its tangent is referred to as loss tangent and it quantifies the ratio of viscous to elastic behavior.

For purely elastic materials, there is not energy loss and the complex shear modulus contains only its real component storage modulus: G'' and θ are zero. In general, G' and θ are considered primarily elasticity-related metric; G'' and $|G|$ are viscosity-related.

- damping ratio: attenuation of the wave α measured in [1/m]. After passing trough 1 meter of medium, wave frequency will attenuate by the factor $e^{-\alpha}$, thus, a new value of frequency would be equal to $\omega e^{-\alpha}$. α is a function of angular frequency (ω) of the external vibrations through from G^* and can be computed as:

$$\alpha(\omega) = \frac{\omega\sqrt{\rho(|G^*| - G')}}{\sqrt{2}G^*} \tag{9}$$

Angular frequency ω can be calculated from actuation frequency f by: $\omega = 2\pi f$.

- shear wave speed ν_s measured in $[\frac{m}{s}]$, is function of ω and is affected by both elastic and viscous properties; it can be retrieved from G^* through

$$\nu_s^2(\omega) = 2\frac{|G^*|^2)}{\rho(G' + |G|)} \tag{10}$$

For details on these viscoelastic constants and laws, please refer to the book [15].
In this neuroimaging-focused work, maps of the complex shear modulus G^* will be computed through MRE inversion, because its real and imaginary part have a closer correlation to clinical outcomes. Some studies about generical elastography inversion focus on damping ratio and wave speed estimation, which are easily computable from G^*, as illustrated in the previous laws.

3.1.7 Physics Equations

To understand how to invert MRE data, which relies on mechanics differential equations, one should describe physically how waves propagate and attenuate in materials. Considered the assumptions made in the previous section (section 3.1.6), inserting the linear isotropic stress-strain relation into motion equation, one can derive the general harmonic motion equation for in an isotropic linear viscoelastic medium. This equation models waves behaviour in brain tissues, ignoring spatial derivatives of the material viscoelastic properties:

$$G^*\nabla^2\mathbf{u}(f) + (G^* + \lambda)\nabla(\nabla \cdot \mathbf{u}(f)) = -\rho\omega^2\mathbf{u}(f) \tag{11}$$

formulated also as:

$$\nabla \cdot [G^*(\nabla\mathbf{u}(f) + (\nabla\mathbf{u}(f)^T)] + \nabla \cdot (\lambda\nabla \cdot \mathbf{u}(f)) = -\rho\omega^2\mathbf{u}(f) \tag{12}$$

to distinguish the compression or pressure component $[\nabla \cdot (\lambda\nabla \cdot \mathbf{u}(f))]$ from the incompressible term $[\nabla \cdot [G^*(\nabla\mathbf{u}(f) + (\nabla\mathbf{u}(f)^T))]$. For details on the physical laws used and the calculations leading to these equations, please refer to the book [15].
Three parameters are contained in these equations: mass density ρ, Lamè's first parameter λ, associated with material's response to volumetric (compressive or tensile) stress, and complex shear modulus G^*, associated with the material's response to shear, or tranverse, stress. Shear waves are much slower than longitudinal ones because λ (orders of GPa) is approximately six orders of magnitude greater than G^* (orders of KPa), making λ estimation unnecessary and considerably challenging. MRE elastography is oriented toward shear waves and these two parameters can be decoupled [26]. But longitudinal (compressional) wave component must be necessarily taken into account and removed because it also contributes to the total measured displacement field, where the wave component of interest is the tranverse one.

One possible method to consider compressional waves is high-pass filtering, since the contribution of the longitudinal component is concentrated at low frequencies [4]. Alternatively, it can be assumed that displacement due to longitudinal waves is negligible because of the large differences between longitudinal and shear waves in tissue; this assumption can be formulated as $\lambda(\nabla \cdot \mathbf{u}(f)) = 0$. Equation 11 becomes:

$$G^*(\nabla^2\mathbf{u}(f) + \nabla(\nabla \cdot \mathbf{u}(f)) = -\rho\omega^2\mathbf{u}(f) \tag{13}$$

reformulated as (see Equation 12):

$$\nabla \cdot [G^*(\nabla \mathbf{u}(f) + (\nabla \mathbf{u}(f)^T)] = -\rho\omega^2 \mathbf{u}(f) \tag{14}$$

Expanding in Equation 17 the first divergence operator, one can finally obtain:

$$G^*\nabla^2 \mathbf{u}(f) + \left(\nabla \mathbf{u}(f) + \nabla \mathbf{u}(f)^T\right) \nabla G^* = -\rho\omega^2 \mathbf{u}(f) \tag{15}$$

This is a relevant equation for this work and will be referred as **heterogeneous wave equation**.

Actually, in [27], it is recommended not to ignore the entire second term of the left-hand side of Equation 12 ($\lambda(\nabla \cdot \mathbf{u}(f) = 0)$) because the small magnitude of the term $\nabla \cdot \mathbf{u}(f)$ is compensated by the large magnitude of λ in incompressible materials, which leads to a non-zero pressure term and errors in the reconstructed stiffness [28], but rather apply the curl operator to both sides of Equation 12 to get to Helmholtz equation (Equation 19) because the longitudinal component of the displacement field is curl-free according to Helmholtz decomposition. According to Helmholtz decomposition theorem [29], a vector (displacement field) $\mathbf{u}$ can be decomposed into two components, one vanishing curl longitudinal $\mathbf{u_L}$ and one divergence-free term tranverse $\mathbf{u_T}$, such that:

$$\mathbf{u} = \mathbf{u_L} + \mathbf{u_T} \tag{16}$$

$$\nabla \cdot \mathbf{u_T} = 0 \tag{17}$$

$$\nabla \times \mathbf{u_L} = 0 \tag{18}$$

Calculating the vector curl of the measured wave field is a very common approach [30] [9].

Another reasonable possibility is assuming strict tissue incompressibility, i.e. displacement due to longitudinal waves is absent ($\nabla \cdot \mathbf{u}(f) = 0$) in Equation 12, considered the high content of water in the brain, and get to Helmholtz equation. The Helmholtz equation is a general wave equation for a monofrequency wave field:

$$G^*\nabla^2 \mathbf{u}(f) = -\rho\omega^2 \mathbf{u}(f) \tag{19}$$

Equation 19 directly relates the measured displacements to the complex shear modulus G^* by the angular frequency ω and the material density ρ. This is another core relation for MRE inver-

sions developed in this thesis work and will be referred as **homogeneous** or **Helmholtz wave equation**.

In some papers, such as the reference study used in this research [10], the notation μ is used in place of G^*: they both express the same complex quantity, i.e. the shear modulus that provides a complete understanding of viscoelastic materials' behaviour by considering both the elastic and viscous responses over a range of frequencies.

3.1.8 Viscoelastic MRE inversion

A wave equation generally explains how wave propagate into tissues, if the parameter fields $G^*(\mathbf{r})$, $\lambda(\mathbf{r})$ and the boundary conditions on the surface of the objects are known[9]. In a typical forward problem, material parameters, pressure field and boundary conditions are known and necessary to estimate full displacement field generated by mechanical traction. Solving an inverse problem, on the other side, means deriving the spatial distribution of mechanical viscoelastic parameters from the extracted displacement field $\mathbf{u}(\mathbf{r})$, i.e, the wave image. The goal is to retrieve the complex shear modulus field, also called elastogram, $G^*(\mathbf{r}) : \Omega \to \mathbb{R}^3$, from the complex vector field tissue displacement $\mathbf{u}(\mathbf{r}) : \Omega \to \mathbb{C}^3$ measured by MRE scan, where Ω is the spatial domain where these physical quantities are defined. The resulting elastogram is usually of the same resolution as displacement images [31].

Strain characteristics of waves depend on the mechanical properties of the medium they are propagating and this should allow ideally to estimate mechanical parameters from strain data. Nevertheless, solution of this inverse problem is inherently ill-posed or nonunique, requiring either regularization methods or introduction of a priori knowledge [32]. Various algorithms have arisen through research: Direct Inversion (DI), Local Frequency Estimation (LFE), Nonlinear Inversion (NLI) and Multifrequency inversion will be briefly illustrated in section 4.

3.2 MRE Clinical applications

MRE-derived mechanical properties can be used to detect biological or functional brain changes from the normative state to the disease state and to characterize diseases. Storage modulus variation of biological tissues ranges up to four magnitude orders [26] varying as the molecular and intermolecular constituents change structure [32], while physical properties extracted by conventional medical imaging techniques vary over a smaller numerical range. The storage modulus G^* ranges from 0.1 to 5 kPa in the brain, varies between 4 and 7.5 kPa in the heart during different cardiac phases, and can reach up to 600 kPa in the intervertebral disc.

MRE is therefore a powerful imaging technique because it has a high sensitivity: tissues viscoelastic properties change significantly in many disease states and tumors are generally identified and located as areas of different stiffness.

Liver fibrosis is a response to injury resulting in extracellular matrix accumulation including fibrillar collagen and proteglycans [33]. It is well established that MRE is a valid biomarker for detection and staging of liver fibrosis with more sensitivity than other modalities because the disease causes a remarkable stiffness increase, leading the best diagnostic accuracy among various imaging modalities [34] [35]. MRE measures elasticity correlating well with the degree of liver fibrosis [36] [37] and discriminates patients with any fibrosis from significant fibrosis , advanced fibrosis and cirrhosis [38] . Hepatic fibrosis also leads to reduced viscosity, that can be measured through dispersion of the complex shear modulus [39]. MRE can also be exploited as a biomarker to assess portal hyperextension [40] and to detect and categorize [41] non-alcoholic fatty liver disease (NAFLD) patients, i.e. fat accumulation in the liver associated with alcohol abuse.

MRE holds also a significant diagnostic value for the prediction of esophageal varices by measuring splenic elasticity [42]. Moreover, kidney stiffness, which is strongly affected by hemodynamic factors, can be measured and provide information about blood circulation [43] [44]. MRE is also a good candidate for imaging the soft and viscous pancreas and staging chronic pancreatitis or pancreatic cancer monitoring.

Cardiac MRE potentially allows to quantify parameters describing mechanical action of the living heart for diagnosis and therapy monitoring in cardiology [45]. Through quantification of left ventricle (LV) ejection fration (EF) , it can act as an early detector of heart failure and discriminates systolic from diastolic heart failure [46].

Brain MRE holds significant promise for clinical applications as well. In intracranial tumors [4], knowledge of stiffness level is important to plan the surgery treatment, as concerns instrument selection, tumor resection strategy and postoperative course [47] and MRI does not allow to accurately grade it. Instead, MRE-measured stiffness can be exploited to predict intraoperative shift of brain tissues caused by surgical instruments [48]; many works have shown positive correlations of MRE output with surgeon's preoperative impressions rated on a 5-point scale (scores ranging from 1, indicating soft tumors removable with suction, to 5, meaning hard requiring scissors or ultrasonic aspiration) [49] [50] [51]. In [52], MRE examination for meningioma assessment, the most common primary intracranial tumor arising from meninges, provides a stronger correlation with the surgical assessment of stiffness compared with traditional T1w and T2w imaging, particularly for intermediate stiffness meningiomas. Data analysed in [51] show a tendency for greater storage modulus *G'* in firm adenomas compared to soft adenomas which is a valuable information for surgical planning, suggesting that the consistency of pituitary adenomas depends on the level of fibrosis.

Other possible applications are intra-axial tumor differentiation and grading. Tumors growth causes nonuniform deformation of brain structures, constrained by stresses of surrounding tissues and described by extremely complex mechanics [48]. Brain tumors are generally distinguished as benign, such as meningioma and pituitary adenomas, and malign, such as astrocytoma, glioblastoma and metastatic tumors. In [53] it is revealed that MRE biomechanical properties vary between tumors like benign meningioma, high-grade glioblastoma and oligoastrocytoma, while corresponding anatomical MRI images are much similar. In [51], mean and maximum MRE measured shear stiffness for meningioma is higher than pituitary adenoma ($p < 0.05$) and these values significantly correlate with the surgeon's qualitative assessment of tumor consistency. However, an important study [54] has shown that magnitude of complex shear stiffness has large variability among tumors and cannot discriminate tumors grades: this heterogeneity of values may be attributed to the fact that rapid tumor growth lacks sufficient nutrition and leads to a coexistence of solid tumor portions, central necrosis or haemorrhagic transformation and cystic components [54]. On the other side, relative difference of loss tangent $\delta\phi$ from areas not tumor-affected allows to distinguish clearly meningiomas from gliomas and metastatic brain tumors. This higher dissipative behaviour of meningiomas may be explained by the higher cellular network density within the tumor compared with other tumor entities [54].

Assessment of brain tumor adhesion can be obtained with a MRE scan by identifying discon-

tinuities in the displacement field on the tumor - brain boundary which reflects slip interface, through a technique called slip interface imaging (SII). The concept is: the greater is tumor adhesion, the more fixed it becomes, the less slipping and motion will occur at its boundary [55].

It is also possible to investigate non-localized brain biomechanics to understand the correlations of global and regional stiffness measurements in healthy and diseased states throughout life; many studies confirm that brain stiffness decreases with age but correlations are different throughout brain regions [56] [57] [58] [59]. Stiffness topography is under investigation, but it is well established that White Matter (WM) is stiffer and more viscous than Gray matter (GM) [60], the stiffest brain region is the deep GM and deep WM, and cerebellum is the most soft region [58]. WM contains oligodendrocytes which form the myelin sheath, astrocytes, microglia and has fiber bundles of aligned myelinated axons [61]; GM contains neurons, astrocytes and microglia and is less organized, lacking network support: topography stiffness differences agree with some research works which have shown tissue stiffness increases with myelination during development in WM [62] and negatively correlates with the density of cell nuclei [63]. Another work leveraged this technique and combined a nonmagnetic motion source with multifrequency dual elasto-visco inversion (MDEV)reconstructions [64], to provide the first normalized map of brain viscoelasticity at high spatial resolution to use as background data for clinical applications of cerebral MRE.

Diagnosis and management of patients with neurodegenerative disorders is another important field of application.

Normal pressure hydrocephalus (NPH) is a disease characterized by an abnormal accumulation of cerebrospinal fluid (CSF) in the brain's ventricles leading to an increase in intracranial pressure (ICP). Lots of research have pointed out that it causes a mechanical tissue damage that alters brain stiffness, but there are inconsistencies: some studies [65] have reported global reduction in shear elasticity μ on the order of 20% or [66] significant decrease of viscoelastic parameters μ and α compared to age-matched controls ($p < 0.001$). Other studies instead have shown increased stiffness in NPH patients[67], most in periventricular WM. A research [68] found significantly increased stiffness in NPH patients in cerebrum, occipital , and parietal ROIs and significantly decreased stiffness in periventricular ROIs (areas located around the ventricles in the brain). NPH pathophisiology is still under investigation: what is known is that increased intracranial pressure, which has been detected in patients with NPH, might play a role in brain

stiffening occurring because it causes ventricular dilation that compresses interstitial and intracellular fluids out of parenchymal pores. The tissue compression would lead to a nonlinear elastic response, causing stiffening.
Ventricular dilatation is not the only physiological cause of this disease. Corresponding cellular changes contribute to this stiffening: there is a reported increase in the ratio of cytoskeletal matrix to interstitial and intracellular fluids in NPH patients [69]: the cytoskeleton, composed of microtubules, provides structural support to the cell and a higher proportion of these elements and cytoskeletal proteins increases the cell's rigidity, while less fluid means less ability for the cell to deform easily under stress, as fluids can readily flow and redistribute. The study [70] suggests also that less densely packed axonal fibers and less compact myelin sheaths (demyelination) might be the cause of reduced WM stiffness in early-onset hydrocephalus. Moreover, a reduction of blood flow and of capillary density was observed in NPH WM: the chronic pressure exerted by CSF accumulation and ventricular dilatation might bring to prolonged compression and to these ischemia phenomenons. This may result in a breakdown of cellular structures and extracellular matrix (ECM) that further co-contribute to stiffness changes.
There is also an implication from inflammatory processes, which are common in hydrocephalus, that might lead to the degradation of ECM components and the disruption of normal tissue architecture.

Multiple sclerosis (MS) causes some structural modifications detectable by MRE: in [71], storage modulus μ and viscoelastic attenuation α results significantly reduced in patients with chronic progressive MS compared to healthy controls, while the relapsing-remitting disease shows only alteration of viscous effects ant not shear elasticity reduction. These alterations are caused by parenchimal degradation occuring in MS, which impacts both mechanical matrix brain and its volume (brain atrophy). Factors determining this parenchimal loss of integrity might be demyalination, the hallmark MS feature, degeneration of neurons and axons, incomplete remyelination (the process of restoring the myelin sheath), reduction of Mature Oligodendrocytes and reactive astrogliosis, a process where astrocytes become hypertrophic and proliferate in response to injury or disease.

Patients with Alzheimer's Disease (AD), a progressive disease that causes cognitive decline, show a significant stiffness decrease compared to age-matched healthy controls [15] [2]. Stiffness changes occur mostly in the frontal, parietal and temporal lobes. these regions viscoelastic properties are strongly affected by the disease and show great potential for detecting AD patients Possible reasons for this loss might be a significant reduction of neuroprotective perineuronal

nets (PNNs) that makes neurons withouth PPNs more susceptible to degeneration [72]; PNNs are unique ECM structures that wrap around the cell body of many neurons [73]. Cell body density correlates with tissue stiffness and cell numbers are reduced in AD patients compared to control which might me another cause of AD softness. Moreover, formation of Amyloid plaques is peculiar of AD, which are compounds stiffer than surrounding brain tissues that cause a loss of neuronal stiffness, induces oxidative stresses and alters membrane properties through mechanotransduction events.

Another analysis [74] revealed that brain stiffness is significantly and positively correlated with default mode network connectivity.

Another effort that led to significant discoveries was[3]: differential diagnosis of Parkinson's disease (PD) and Progressive supranuclear palsy (PSP) is still a challenge and it was found that viscoelasticity parameters are differenty affected by PSP and PD degenerations. In PSP all MRE constants are reduced, in PD changes of brain elasticity predominate viscosity ones. [75] supported this conclusions stating that reduced mesencephalic $|G^*|$ discriminates PSP from PD ($p < 0.05$) and that neurodegeneration is more pronounced in PSP patients ($p < 0.05$ vs PD). Biological underpinnings and correlations of these viscoelastic changes are consistent with MS ones: it was suggested axonal degradation, demyelination and degradation of the extracellular matrix can lead to a drop in G^* . The study [3] mentions that a drop in $|G^*|$ and μ without a change in α might suggest the presence of inflammatory processes. Varying degrees of extraneuronal involvement (glial cells, astrocytes) in PSP and PD might contribute to the differences in viscoelastic changes. In PD, there is also presynaptic accumulation of α-synuclein, which starts focally and affects axonal integrity only later in the degeneration process, and might explain why viscoelastic parameters remain largely unchanged in PD compared to PSP.

The complex mechanics of neurodegenerative diseases is still an open field of research that requires an understanding of the relationship between cell body density, cell type and tissue stiffness in different brain regions but presents some common denominators such as brain cells degenerations with cytoskeletal perturbations, ECM composition change, neuroinflammation and intervention of pathological proteins and peptides, such as amyloid plaques, which alter the mechanical properties of neurons and glia. [72].

Future perspectives include imaging the neuronal activity biomechanics response of tissue viscoelasticity to functional processes [4].

3.3 MRE Hardware

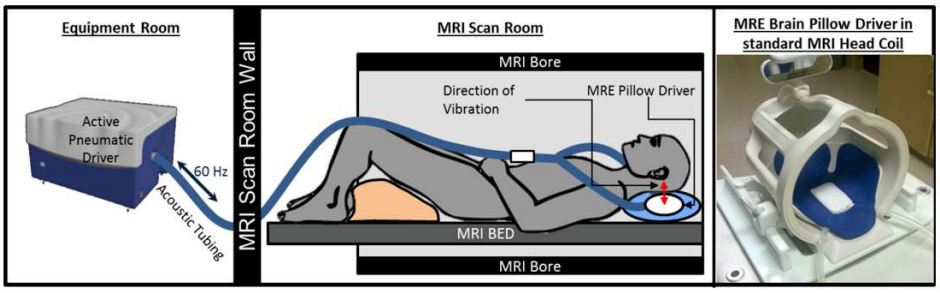

Figure 10: MRE hardware components. Adapted from " Harnessing brain waves: a review of brain magnetic resonance elastography for clinicians and scientists entering the field", by Arani et al, 2021, The British Journal of Radiology. @ 2021, Br J Radiol.

In MRE scanners, an active driver is combined with a transducer, which transmits the mechanical waves into the target tissue. MRE transducers can be either pillow-type passive devices or head cradle passive drivers. Active drivers are the source of motion and are externally power-supplied by either pneumatic vibrations, requiring waveguide ducts, piezoelectric or electromagnetic signals. Transducers cause tissues to experience a motion and are usually placed inside the scanner,while electrical and control units are outside the MRE room (Figure 10) . Connections through the MRI room can be nonconductive (e.g., plastic tubes for air or hydraulic fluid) or fitted with electronic filters.

Nonmetallic drivers are preferred to avoid interactions between actuators and MRE magnetic field. The device applies shear acoustic waves into the tissue of interest with a set frequency and transmits acoustic energy through the brain. The frequency is set according to attenuation, sensitivity and exposure constraints.

It is well known that wave delivery methodology can influence MRE brain displacement fields and lead errors in mechanical properties estimation. In [76], FEM based modal analysis and harmonic simulations have shown that displacement vector magnitudes depend on wave delivery method, which can lead to different resonance peaks at the natural frequency of the skull (determined by the anatomical components and boundary conditions); different loading methods of the skull also bring to different displacement amplitudes. The study pointed out that waves pattern reconstruction varies a lot between vibration frequencies of 50 Hz and 90 Hz for the same wave delivery method and that head-cradle and acoustic pillow delivery methods give the lower inversion error. To ensure consistency between studies and reproducible measures of these low brain mechanics variations, it's therefore important to use a common stable methodology [76].

MRE systems should respect some requirements to provide sufficient phase to noise ratio (PNR).

In fact, an homogeneous magnetic field to avoid phase wraps, high precision delivery gradients to guarantee a linear relationship displacement-phase (Equation 8) and good connection between generator and MRI computer to guarantee time synchronization sequence-motion are necessary to produce a fast and robust MRE signal.

3.4 Deep Learning

Deep learning is a type of machine learning based on artificial neurons connected into a network that form an artificial neural networks. Several layers and of different types (e.g. dense, convolutional) are included: one input layer, hidden layers and one output layer (Figure 12).

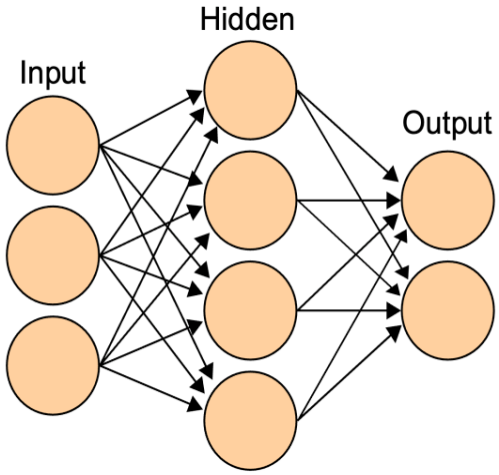

Figure 11: ANN include several layers.

DL methods are representation-learning methods that can be fed with raw data. A model, the neural network, is composed of multiple simple non-linear modules, the network layers, that progressively transform data representations at a higher and higher level in order to learn very complex nonlinear functions [77]. These layers do not require engineering by hand but learn directly from raw data; this makes DL techniques inherently based on data and very good at discovering patterns in high-dimensional data.

3.4.1 Artificial Neural Network

Within the network, each artificial neuron computes the weighted sum of the received input, adds a bias, and mediates the output with a nonlinear activation function that recalls the firing mechanism of biological neurons (Figure 12): this last step introduces non-linearity in the model and maps neuron outputs to a specific range, avoiding saturation (which can bring to vanishing/ exploding gradients, [78]). The number of layers and number of neurons per layer are the first relevant network parameters: the network used in this work has 5 layers with 128 neurons per layers (see Table 2 in section 5.1). Examples of common activation functions are the logistic function, hyperbolic tangent, sin function (used in this work's ANN), Rectified linear unit (ReLu) and Maxout[79]. Feedforward networks contain only fully-connected (or dense)

layers, in which each neuron is connected to every neuron of the previous layer. Another type of network is the convolutional neural network (CNN), based on convolution and developed to process data in the form of arrays, such as 2D images.

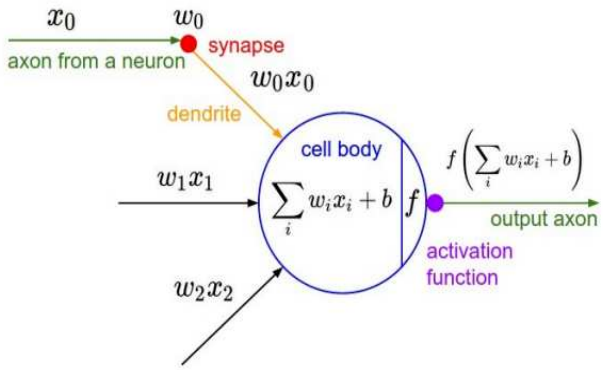

Figure 12: Each artificial neuron output is the sum of inputs received and a bias term, followed by an activation function. Adapted from "Backpropagation with Andrej Karpathy: Part 2", Kavishka Abeywardana, The Deep Hub, Medium

The neural network implemented in this work is an example of supervised deep learning. Supervised learning builds DL models from labeled training examples: an error function defines a cost function that quantifies the distance between the model predictions and the desired ground truth targets. The cost function, called loss function, should be minimized: network parameters, i.e. weights and biases of each neuron, are random initialized and iteratively modified to reduce it with a backpropagation algorithm. An example of cost function is Mean Squared Error loss (MSE), presented in Equation 39 (Section 5.2.1).

The learning algorithm computes a gradient vector that indicates for each parameter how fast the loss changes with respect to a change in that parameter and parameters are then adjusted in the opposite direction of the gradient, i.e. in the decreasing loss direction. To improve the efficiency and computation of the gradient descent, Stochastic Gradient Descent (SGD) optimization can be implemented, in which the gradient is calculated only on a random subset of training examples, called minibatch, and weights are adjusted accordingly; this increases the frequency of weight updates for each epoch. The number of samples for a minibatch is called batch-size and is an hyperparameter to be set also according to available computational resources. An epoch is one complete pass through the entire training dataset. SGD optimization can be further improved with momentum hyperparameter damping, such as in the method used in the reference study of this work for PINN development: Adaptive Moment Estimation (Adam)[80]. Adam is a method for efficient stochastic optimization that adjusts individual adaptive learning rates for different

parameters based on first and second gradients moments and presents various advantages, such as the magnitudes of parameter updates are invariant to gradient rescaling and that it works with sparse gradients [80].

The speed at which the network learns from data is determined by the hyperparameter Learning Rate (LR) that multiplies the weight update. LR has to be set carefully because it strongly affects the training phase: if the learner is too slow, it might never get to a loss minimum, if too fast, it might overshoot the minimum. For PINNs it is usally set to 1e-3 or 1e-4; the second option is chosen for this work's PINN. Other algorithmic parameters are weights initialization design, and for multiloss problems, such as PINNs, loss relative weights [81].

After training, the model is evaluated on a separate set of examples called test set, to assess its performances and its generalizability, namely, how it performs on new, unseen data.

4 State of The Art

When measuring MRE, it is fundamental to understand the extent at which the phase measured is accumulated because of spin motion scattered by the vibration, or it is due to noise, which in MRE is usually supposed gaussian and its effect depends:

- on the processing algorithm, because derivative tends to amplify it
- on the actuation frequency, because attenuation increases when this becomes high
- on the actual stiffness, because the stiffer the material, the longer the wavelength and the more the noise influence due to smaller derivatives

Noise limits MRE resolution because a high-resolution image leads to many pixels per wavelength and noise signal dominating over oscillating waves signal. This is is the main drawback of inverting MRE data with DI methods.

Discretization artifacts, on the other side, occur with calculation of the derivative of a discrete displacement field, as happens in many algorithms: a finite voxel spacing can impact subsequent mathematical operations. These failures are common for FEM inversions.
Discretization artifacts are dominant for low resolutions and cause overestimation of wave speed and viscoelastic moduli, noise occurs at higher resolutions and causes their underestimation.

Various algorithms have arisen through research to inverting MRE data: Direct Inversion (DI), Local Frequency Estimation (LFE), Nonlinear Inversion (NLI). Each technique relies on some assumptions and implementation choices [8] with varying robustness, accuracy, computation time and ease of use [1]. Time consuming estimation of the stiffness maps, ill-posedness and nonuniqueness solution of the inverse problem, low resolution and noise sensitivity make it challenging to extract accurate and high-resolution results. In this section, DI and FEM inversion methods will be detailed, serving as benchmarks against the innovative MRE inversion introduced in this study. LFE and Multifrequency inversion will be also briefly explained.

For these reasons, there is a strong need for developing advanced inversion algorithms capable of relaxing tissues homogeneity assumption, while maintaining efficiency, clinical feasibility, good resolution and numerical stability. Some research groups have recently started to solve the inversion problem with Artificial Neural Network inversion (Section 4.5).

4.1 Direct inversion (single frequency)

DI directly solves the Helmholtz equations of motion in a locally homogeneous, linear and viscoelastic material and produces a fast estimate of the complex shear modulus. The Helmholtz equation (Equation 19) relates directly displacement field to the complex shear modulus G^* and is formally obtained applying the general wave equation to a monofrequency wave field [33]. Only shear displacement field is accounted in computation. It is derivable from the wave equation (left) by applying FFT (right):

$$\Delta u(x,t) = \frac{1}{c^2}\ddot{u}(x,t) \quad \rightarrow \quad \Delta\tilde{u}(x,w) = -\frac{w^2}{c^2}\tilde{u}(x,w) \qquad . \ (20)$$

DI can handle both isotropic and anisotropic models: in the first case, the estimate of each vector component u_i of the tridimensional wave field yields the same value, while in anisotropic media the components u_i should accordingly yield different values.
Spatial distribution of G^* can be inferred:

$$G_i^* = -\rho\omega^2\frac{\tilde{u_i}}{\Delta\tilde{u_i}} \qquad . \ (21)$$

Wave fields are a superposition of shear and longitudinal waves, described by different wave speeds and complex shear moduli. DI can handle this superposition, either via multiparameters inversion, solving Equation 13 to calculate both moduli G^* and λ with matrix inversion, or via Helmholtz Decomposition, decoupling Equation 13 through the divergence and curl operators (Section 3.1.7) [9]. With the same calculations, through Equation 21 one can derive also the local wave number k from k=$\frac{\omega}{\nu_s}$, where ν_s is the phase speed of the shear wave.

The main drawback of this approach is the high noise sensitivity because DI algorithm contains Laplacian operation causing small noise fluctuations in the wave field to potentially be dramatically amplified with the double derivative contained in it. This numerical instability at the voxel-level can be solved by either decreasing spatial resolution or by additional smoothing. Estimation of spatial derivatives from noisy displacement data can be effectively computed [5] with Savitsky and Golay filter [82]. Moreover, to solve the equation, DI assumes local homogeneity of viscoelastic parameters which can negatively impact the final estimation's accuracy and sensitivity to noise.

Also data discreteness, not taking into account boundary conditions diffraction, transducer near field and reflections complicate the relationship local wave number - complex stiffness, assumed straightforward in the ideal case (Equation 21), leading only apparent phase speed estimates. This wave speed inversion-intrinsic dispersion can be minimized adopting an optimal spatial resolution, expressed as wavelenghts per pixel size $\frac{\lambda}{a}$.

A novel DI application with a variational formulation was presented in [32] where the DI problem is defined in an equivalent variational (or weak) form, from which a solution for material parameters can be obtained in a practical and computationally efficient way. Results in [32] show that local inversion is applicable but presents some issues, with inversion breaking down at the interface, high sensitivity to noise in the numerical calculation of the displacement data and lack of spatial variation in predicted displacements.

4.2 Nonlinear inversion (Finite Element Model)

Finite Element Models (FEM) are a numerical method of solving partial differential equations to achieve approximate solutions in a discretized form of the problem's spatial domain. FEM methods are used for forward modeling; elastography in contrast is an inverse problem, where the displacement field is given to determine the viscoelastic parameters distribution. This can be solved with FEM in an iterative way with nonlinear inversion by minimising the error between the FEM model and the acquired displacement field; iterations continue until the measured displacement is sufficiently closed to the FEM current displacement predicted by the forward model.

This approach has the advantages of being able to incorporate the full motion equation (Equation 12), and can release the assumptions of linear elasticity [83][84], it is more flexible and more robust than DI [4]. However, this method is computationally costly and has reconstruction times of the orders of hours, compared to seconds-minutes for DI, so it's not practically suitable for clinical workflows [4]. Moreover, most algorithms proposed [9] assume that the measured displacement field is purely transverse without any compression waves and this is not always the case (see Section 3.1.7).

In FEM modeling [85], the problem domain is divided into geometric units called finite elements. For example, in MRE data, a subzone-based technique has been proposed [86]. Within each finite element, a set of basis functions is used to interpolate the problem's parameters based on the values at the nodes. To reduce computational complexity, each basis function is designed

to have a small support, confined to the specific finite element it is associated with. The PDEs are then transformed into algebraic equations that apply to each finite element, known as element stiffness equations. These equations are assembled into a system of global stiffness equations. Finally, boundary conditions are applied before solving the global stiffness equations to determine the unknown nodal parameters.

4.3 Local Frequency Estimation

In the earliest approach [87], the local wavelength of the propagating wave was exploited, which depends on the material's real-valued shear modulus via

$$\mu = \rho\nu_s^2 = \rho(\lambda f)^2. \tag{22}$$

LFE estimates the wave number k by applying a pair of band-pass filters to the wave image and extracting k from the ratio of the filtered images, from which the shear wave speed and shear modulus can be computed.
This method is less noise-sensitive than DI as it does not require the second derivative operation. Nevertheless, the filter width determines the LFE spatial resolution, and consequently one big disadvantage of this approach is the limited spatial resolution: LFE accuracy is affected by tissue heterogeneities, tissue boundaries, where LFE estimates are blurred, small inclusions, and the presence of noise in the measured data [9].

LFE and DI have been tested on different simulations [26]: DI results sharper and more sensitive to noise and more affected by amplitude nulls while LFE estimate results to be smoother, with lower resolution and fewer artifacts. Additionally, LFE can trade off noise sensitivity and resolution by altering the local filter window size.

4.4 Multifrequency MRE

In high-noise regions, or deeper tissues where induced vibration amplitude is reduced, DI estimation process can become very unstable and this effect is greatly enhanced in the presence of standing waves. These occur when incoming and reflected waves within tissues interfere constructively or destructively, resulting in regions where the displacement oscillates with minimal or maximal amplitude (nodes and antinodes). Multifrequency approaches allow to deal with them and potentially introduce nodes with zero displacement, i.e. no deformation, but conversely require longer scanning times. One possible solution is averaging over several different

frequencies to make parameters estimation more stable, if it is assumed that viscoelastic properties are not dependent on the vibration frequency. However, absence of dispersion (different shear wave speeds at different frequencies) is true only for purely elastic material.

Another alternative could be apply an algebraic least-squares solution based on the springpot model, a technique proposed in [88], that provides a significant better resolution than single DI and less artifacts because it mitigates amplitude nulls due to standing waves and takes into account dispersion in the inversion procedure.

4.5 Inversion with Deep Learning

Some research groups have recently started to solve the MRE inversion problem with artificial neural network inversion.

Thanks to its high learning capabilities, DL targets high - dimensional nonlinear mapping problems, such as capturing the hidden relations between displacement field and elasticity field from MRE data [89]. Indeed, deep learning methodologies are increasingly becoming the preeminent choice for addressing the inverse problem of elasticity reconstruction: they are data-driven, straightforward, predictions are necessarily bounded by training data and this provides stability [8]. DL techniques are appealing because they relax many constraints of previous inversion methods, such as initial guesses, need for filtering, strong biomechanics assumptions, actuation frequency limitations on mechanical models [90]. It was demonstrated in different works the efficiency of DL in achieving high resolution and high accuracy elastograms, also when training over a limited portion of representative samples [89] [8] [91] [90] [8] [68].

DL methodologies can also diminish susceptibility to noise and offer a real-time and high-throughput solutions that is suitable in a clinical workflow.

One of the first work [8] pointed out that neural network inversions (NNI) can accurately compute stiffness from MRE simulated data, without and with the addition of Gaussian noise: NNI performs always better than DI on simulated data, by explaining twice the variance explained by DI estimates. The same NNI was tested on real brain data: a strong correlation between NNI and DI estimates of stiffness was found and both inversions detected biologically relevant signals, such as significant decreases in cerebral stiffness with increasing age. The study also found that repeteability error was lower in NNI than in DI and voxel-wise analysis suggested that NNI is more sensitive than DI at a given resolution. The study was constrained by a model that assumed tissue homogeneity within each patch and lack of information on attenuation. Despite these limitations, it highlighted the significant potential of NNI inversion for solving elasticity inverse problem.

In the same year another team [90] furthered the previous effort proposing a ANN that maps displacements to elastograms by directly including convolutional layers in order to skip the pre-processing steps of partitioning data that were present in Murphy's work [8]. In addition to the fitting data loss, there is an extra loss term which contributes to the overall loss function motivated by MRE mechanical models to ensures the generated images respected the mechanical relationship between displacement $\mathbf{u}$ and stiffness μ. The secondary loss was derived by

Navier's equation assuming the absence of longitudinal waves (expressed by $|\mu\nabla^2\mathbf{u} + \omega^2\rho\mathbf{u}|$). The results showed NNI inversion is able to recover high stiffness variations and performs better than NLI and showed the potential of CNN to retrieve tissues elasticity maps.

Two years later the first work [8], this NNI inversion was applied by the same group with some changes: first, a model was introduced to provide a viscoelastic material description (to produce both stiffness and damping ratio maps); secondly, mask patches were applied to data to test the inversion accuracy in the presence of missing data; finally, a convolutional framework was chosen to better leverage spatial information [68]. This ANN produced accurate estimates with missing data, proved to be less susceptible to partial volume effects than DI in simulated data, and reduced bias and variance, compared to DI. The work supported the feasibility and demonstrated flexibility of the NNI framework in MRE.

A recent retrospective study [91] proposed a CNN that predicts voxel-level stiffness in patients with nonalcoholic fatty disease, with only standard MRI sequences clinical data as inputs. The model was not applied to brain images but reached promising results and showed that both MRI images and clinical information contain necessary information for prediction of hepatic stiffness.

4.5.1 Physics-informed neural network

Physics-Based Deep Learning (PBDL) denotes the combination of physical modeling, or classical numerical techniques, with DL-based methods: both the benefits of accurate and robust NNs [92] are leveraged, and it is possible to incorporate domain knowledge, formulated as physical models. The data-driven approach is reconciled with the theory-driven method that relies on a priori models and assumptions [93]: on one side, mathematical and physical models formulated are always an idealized approximation of reality and most inversion techniques for parameters identification are applied to simplified models: DL methods can bridge the gap towards reality by fitting a ANN model to data [93]. On the other side, purely supervised DL frameworks yield good results when a large amount of data is available and their success depends on the quality and amount of data: the introduction of prior knowledge enhances the applicability of these black-box approximators.

Among the various methodology, the Loss-term based PBLD can be used to solve inverse problems, where certain measurements are avaliable for which a Partial Differential Equation (PDE) solution has to be solved. This class of PBDL is also called Physics-Informed Neural Network (PINN). The integration of DL and physics is made via PDEs: physical laws are incorporated into the loss function through an additional term that quantifies the adherence of data to the PDE

that models them.

A PINN model is made of two components that enter its loss term:

- Deep Learning and Neural Networks: the goal is to approximate with a NN *f(x,θ)* an unknown function that explains data

$$f(x;\theta) = y \tag{23}$$

The minimization problem can be set as:

$$\arg\min_{\theta} |f(x;\theta) - y^*|_2^2 \tag{24}$$

where *y** indicates ground truth.

- Physical models. PDE will be denoted as *P**. Their solution is usually defined on a spatial domain $\Omega \subset \mathbb{R}^d$ with d $\in$ {1,2,3} and on a finite time interval t $\subset \mathbb{R}^+$. The network inputs are space and time variables i.e, (**x**,*t*). The corresponding fields are for instance, displacement vector fields **u**: $\mathbb{R}^d \times \mathbb{R}^+ \rightarrow \mathbb{R}^d$ or stiffness field μ: $\mathbb{R}^d \times \mathbb{R}^+ \rightarrow \mathbb{R}$. Given a PDE for **u** (**x**,*t*), it can be expressed as function *F* of **u** derivatives as:

$$\mathbf{u_t} = F(\mathbf{u_x}, \mathbf{u_{xx}}, \mathbf{u_{xx\ldots x}}) \tag{25}$$

where the $\mathbf{u_x}$ and $\mathbf{u_t}$ subscripts indicate spatial and temporal derivatives. If the unknown **u** is well approximated with a NN by $\tilde{\boldsymbol{u}}$, the PDE residual *R* should be naturally satisfied.

$$R = \mathbf{u_t} - F(\mathbf{u_x}, \mathbf{u_{xx}}, \mathbf{u_{xx\ldots x}}) = 0 \tag{26}$$

The minimization problem (Equation 25) and the PDE residual (Equation 27) are integrated and the model is trained to minimize the combination of residual and data-driven loss.

$$\arg\min_{\theta} \alpha_0 \sum_{i=1}^{n} |f(x_i;\theta) - y_i|_2^2 + \alpha_1 R(x_i) \tag{27}$$

where hyperparameters α_0 and α_1 denote the contribution of the supervised and the residual term. Both objectives are simultaneously optimized such that the network learns to fit training data and capturing the PDE knowledge: after training , the network model should be able to provide a solution approximant the underlying PDE systems and to match data [94].

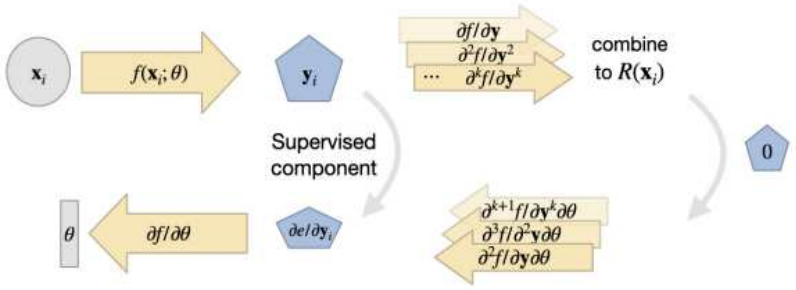

Figure 13: A supervised loss is combined with a set of derivatives from the NN. Adapted from "Physics-based deep learning", by Nils et al, 2021, eprint arXiv:2109.05237. @2021, eprint arXiv:2109.05237.

A PINN example is presented in Figure 13: in addition to the supervised loss term, a Residual term is formulated which collects additional evaluation of θ and its derivatives. Backpropagation algorithm can be leveraged to compute derivatives of the model with respect to learning parameters.

Many works have shown that this integration can substantially improve the training process of a purely DL based method for problems related to fluid dynamics, acustic, heat transfer, solid mechanics and elastodynamics [95] and is more easy to implement than the challenging numerical simulations, particularly with high dimension domain. The success of PINN in different physics problems relies on leveraging the capability of ANNs to become universal approximators and on ensuring the learning of the governing phyics [92]. Supervised DL typically yields inferior results to approaches that tightly couple with physics first because honoring physics, embedding some properties in the DL algorithm that would be almost impossible to inherit, leads to improved robustness and accuracy. Secondly, thanks to use to additional constraints, it is possible to utilize physical knowledge for solving these problems [92] and the training converges even on sparse, insufficient or low resolution datasets [81] [96].
The success of this method can be attributed to 1) the choice of the set of ANN inputs and outputs that allow impose governing equations to the correct solutions 2) algorithmic advances for accurate ANN differentiation 3) advanced ML software like Tensorflow and pytorch [81].

PINN methodologies also have some drawbacks. First, the accuracy of the derivatives relies on how well the representations are learned. Secondly, the training is often computationally expensive and incredibly slow as it requires backpropagation of possibly high-order derivatives; as a consequence, some examples in [93] show that because of the high reconstruction cost, it is not possible to capture a wide range of solution as in the supervised method. There is not yet much

knowledge on hyperparameters performance and the best training configuration [12] and these models tend to yield inaccurate results especially for nonlinear PDEs [94]. Last, it is difficult to control the gradient flow and to balance in an optimal way the different loss terms.

Considering the ideas put forth in [93], the introduction of a PDE loss term can be considered a *physical soft constraint* and not a *physical contrainst machine learning* because the final performance and generalizability of the model is not evaluated on a different unknown test set, as explained in Section 3.4.1, but instead a single solution in a known and given space-time region is produced. Samples from the test domain follow the same distribution of training set and there is little hope that the PINN generalises optimally on a sample out of the training set. With these *soft constraints*, there is no guarantees that the non-linear optimization will make the additional loss term *R* actually reach zero during training and large residual contributions could remain [93]. Such an approach, even with large training data, does not guarantee that the NN obeys the govering equations with convergence to reliable solutions [92].

The capability of PINN of solving inverse identification elasticity problems in nonhomogeneous materials was shown in [97] where, to deal with spatial dependency of mechanical properties, two independent neural networks were defined (respectively, displacement and stiffness predictions from spatial coordinates). The model described an hyperelastic material, adopting a slightly different model from the viscoelastic assumption of this work, but results still showed an overall error of 1 % in stiffness identification and this demonstrated PINN feasibility to solve elastography problems in spatially varying material parameters.

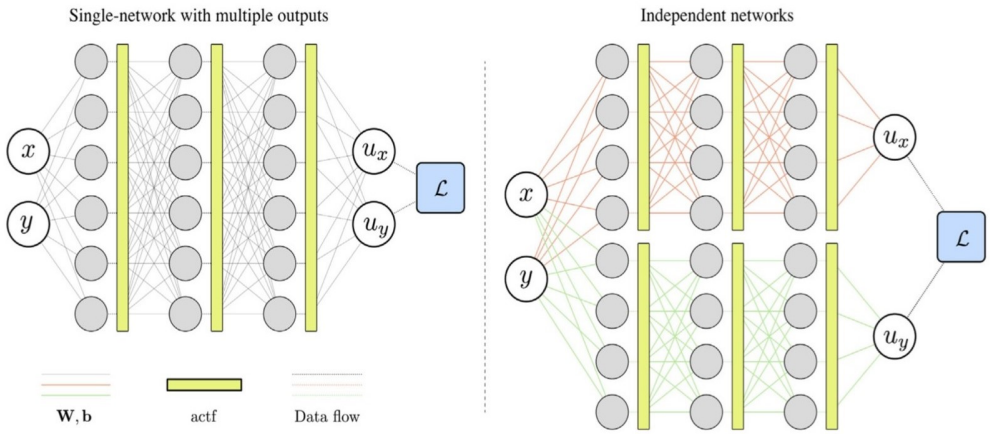

Figure 14: Two possible network structures: two outputs (u_x and u_y) from a single network (left) and from two separate networks (right). Adapted from "A physics-informed deep learning framework for inversion and surrogate modeling in solid mechanics" by Haghighat et al, 2021, Computer Methods in Applied Mechanics and Engineering. @2021 Comp Methods in App Mechanics and Engineering

A PINN was then proposed in [81] to solve inversion of a simple two-dimensional linear elasticity problem in solid mechanics. Two different architectures were proposed: one densely connected network with two outputs (u_x, u_y) or two densely connected independent networks with one output each associated with u_x and u_y (Figure 14) . As a result, defining a separate networks for each solution variable outperforms and is more effective for two reasons. First, the structure of the single feed-forward neural network leads to have the same last layer input for all outputs, thus making more challenging for the single - network to accurately represent all variables, unless solutions are linearly correlated. Secondly, weights and biases, which can be seen as Degrees Of Freedom (DOF) in a FE or meshfree model where each solution variable should employ a separate set of DOF, are accordingly not shared between solution variables in the separate networks model. PINN was validated on synthetic data (generated from low-order and high-order FEM) and on analytical data (Isogeometric Analysis (IGA)) and the importance of using high-order numerical methods or analytical methods for pretraining the network was shown. Incorporating physics into the network architecture enhanced its robustness, as shown by the correct identification of parameters even with a low availability of training data (despite requiring more epochs), and by the accuracy of predictions on new parameters, different from the training parameters. Another important contribution was the relevance of Transfer Learning (TL) applicability, which led to accelerated convergence: performing re-training on new datasets setting as starting parameters a previously trained network (on another dataset) led to lower initial losses and took far less time than training from scratch the model .

Ragoza and Batmanghelich [98] recently published open-source code where they implemented a PINN MRE inversion of simulated data and, for the first time not artificial, of in vivo data from patients with NAFLD. The network presented is dual in order to learn simultaneously representations of the measured displacement field and of the latent elasticity field and the solving of a PDE is incorporated in the learning process. Anatomical information is also included through T1w and T2w scans. Results reveal less sensitivity to various levels of Gaussian noise in simulations and more accuracy on real data compared to FEM and DI inversion; improved stiffness reconstructions thanks to the introduction of anatomical information in the model. This algorithm serves as a reference for the development of the brain PINN of this thesis work and is carefully presented in Section 5.1.

4.5.2 Homogeneity Assumption

Lots of research have tried to assess the negative impact of assuming homogeneity of viscoelastic properties on the accuracy and noise sensitivity of the final MRE brain stiffness estimates [99].

The PINN inversion introduced in [8] also explored how the homogeneity assumption changes the physics equation and consequently the final estimates: in elasticity reconstructions of simulated data with no noise, the PINN containing homogeneity assumptions showed textural artifacts and lower resolution than PINN associated to heterogeneous equation; on in vivo liver data the first one was overcome by the second in terms of Person's correlation with ground truth elastograms ($R^2 = 0.76$ and $R^2 = 0.84$). Another work [11] adopted the aforementioned assumptions but pointed out the restriction and tried to accounts for local inhomogeneity by training parameters on wave data generated by a Coupled Harmonic Oscillator (CHO). This neural network inversion, called Inhomogeneous Learned Inversion (ILI), was compared with Homogeneous Learned Inversion (HLI) and DI: ILI was more accurate than HLI and DI in predicting inclusion stiffness in case of high-noise phantom data, and Dice coefficient was significantly higher for ILI than DI; Dice coefficient is a measure of similarity ranging from 0 to 1 that quantifies the agreement between a model result and a ground truth; ILI offered also sharper transition at tumor edges than HLI and DI. The study confirmed that NNI algorithms for MRE can improve stiffness estimates in materials with spatially varying stiffness and showed advantages of inhomogeneous inversions in case of large stiffness gradient, but the model was trained on simulated data which may not have captured the full complexity and variability of real-world data. In fact, CHO simulations do not reproduce mode waves conversion at interfaces because they do not contain longitudinal waves.

Some years later, the same group evaluated the impact of homogeneity assumptions on stiffness gray matter estimates training two varieties of NNIs on homogeneous and inhomogeneous media of generated data. Instead of CHO, a new Finite Difference Model which incorporates the full physics of wave propagation was used for simulations [99]. ILI proved to be a more sensitive inversion as it showed significantly larger changes of stiffness in response to changes of both volume and stiffness ROI changes. Moreover, in vivo ILI produced stiffness maps with lower apparent spatial variance. This work demonstrated that inhomogeneous inversions offers advantages even when there are not large stiffness gradients, simulated on purposes.

Another study tried to overcome the limitation of homogeneity assumption by taking into account the first order spatial derivatives of the storage modulus [27]. Two equations were tested

in an in vivo liver cancer case study: when using Helmholtz equation, necrotic tissue was not visible and biases were present in areas where spatial derivative of G^* was not neglectable, when applying one equation containing a linear derivative of G', anatomical correspondence was definitely improved and the complex architecture of the lesion was revealed.

5 Training study: MRE Phantom

5.1 Reference Study

Ragoza and Batmanghelich [10] recently presented at 2023 MICCAI conferences the implementation of MRE PINN inversion for in vivo liver data, and published open-source code for this algorithm.

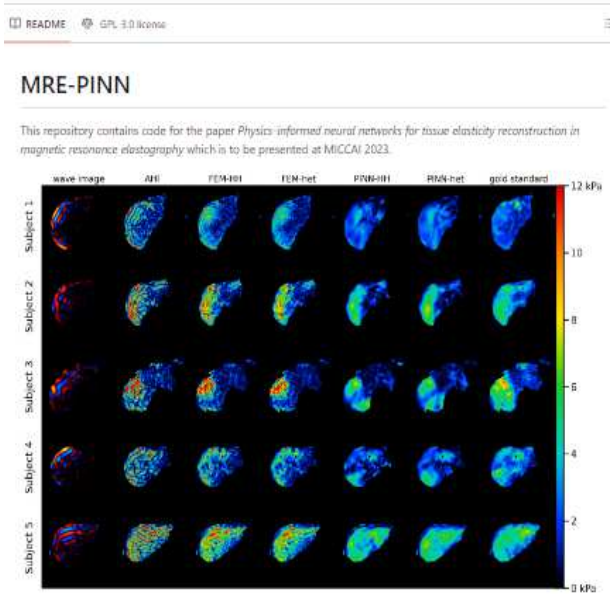

Figure 15: Github repository avaliable from Ragoza [10] work on PINN.

A GitHub repository is available from the work [2] by the BatmanLab team (2023) and the reference algorithm for this work is contained in a notebook within this GitHub folder (Figure 15) [3]. The notebook downloads the BIOphysical Quantitative Imaging Towards Clinical Diagnosis (BIOQIC) FEM box simulation and trains PINNs to reconstruct a map of shear stiffness from the displacement field. The BIOQIC simulation was provided through a collaboration with the Clinical Research Imaging Centre, University of Edinburgh [100].

The algorithm provided by this reference study will be first implemented and adapted in a training study on a MRE phantom, as illustrated in this section (section *Training Study:MRE Phantom*), and then applied in a testing study, as explained in the next one, where the model will be trained on a cohort of brain tissues in the attempt to create a MRE PINN-based inversion algorithm to retrieve brain tissue stiffness maps (section *Testing Study:Delaware Dataset*). Data for

[2] `https://github.com/batman`

[3] `https://github.com/batmanlab/MRE-PINN/blob/main/MICCAI-2023/MICCAI-2023-simulation-training.ipynb`

the testing study are imported from the open - source MRE dataset from Neuroimaging Tools and Resources Collaboratory (NITRC) site, made by the University of Delaware (UDEL) [4].

5.1.1 Reference study: BIOQIC simulation download and PINN inversion

In this section, the simulation code and the algorithm developed from Ragoza [10] in the Github notebook will be briefly presented .

The notebook downloads BIOQIC simulation, creates, trains and tests a PINN for MRE liver inversion. It takes roughly 2.5 h to train for 100,000 iterations on an RTX 5000 and uses 2.5 GiB of GPU memory.

BIOQIC simulation consists of a FEM box phantom made of a viscoelastic box with four targets of decreasing size (background material with storage modulus of 3 KPa, targets with storage modulus of 10 kPa). The waves are actuated by a traction force on the top xz plane and displacement is predominantly in the z direction (Figure 16).

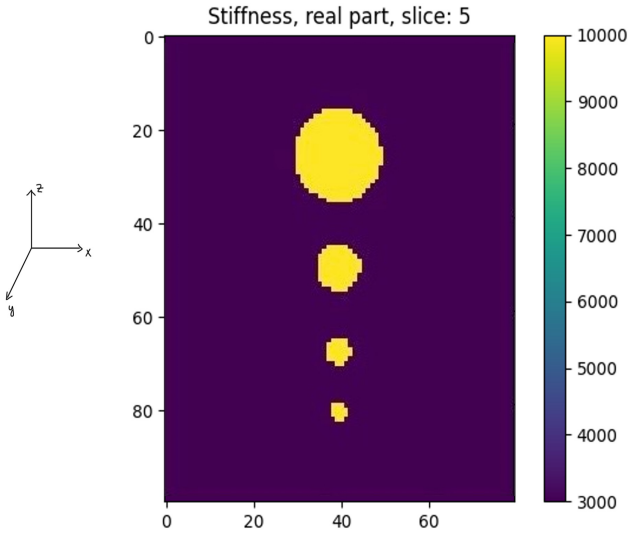

Figure 16: Simulated viscoelastic stiffness box with four targets of increasing size (Pa).

Harmonic MRE introduces a single frequency wave to generate harmonic motion: this phenomenon is modeled by an equation that implicitly contains the mechanical assumptions of linear and isotropic stress and strain behaviour of the medium. Physics equation used to define the PDE loss term included in the PINN are shown in Table 1. A complex scalar field $\mu(\mathbf{x}) : \Omega \to \mathbb{R}^3$ defines elasticity, while the complex vector field tissue displacement is expressed as $\mathbf{u}(\mathbf{x}) : \Omega \to \mathbb{C}^3$. Mass density ρ is assumed equal to 1000 kg/m^3, actuator frequency ω de-

[4] https://www.nitrc.org/frs/?group_id=1390

Name	Assumptions		Equation
	$\nabla \cdot \mathbf{u} = 0$	$\nabla \mu = 0$	$\mathcal{D}(\mu, \mathbf{u}, \mathbf{x}) = 0$
general form			$\nabla \cdot \left[\mu \left(\nabla \mathbf{u} + \nabla \mathbf{u}^\top\right) + \lambda (\nabla \cdot \mathbf{u}) \mathbf{I}\right] + \rho \omega^2 \mathbf{u} = 0$
heterogeneous	✓		$\mu \nabla^2 \mathbf{u} + \left(\nabla \mathbf{u} + \nabla \mathbf{u}^\top\right) \nabla \mu + \rho \omega^2 \mathbf{u} = 0$
Helmholtz	✓	✓	$\mu \nabla^2 \mathbf{u} + \rho \omega^2 \mathbf{u} = 0$

Table 1: Physical equations relating the displacement field **u** to the complex shear modulus of elasticity μ during a steady-state harmonic motion from the theory of linear elasticity. Adapted from "Physics-Informed Neural Networks for Tissue Elasticity Reconstruction in Magnetic Resonance Elastography" from Ragoza et al, 2023 Springer eBook. @2023, Springer Nature. Used with permission.

.

pends on the vibration purposely introduced. The general motion equation previously presented in Equation 12, is indicated as general form PDE (Table 1). Please note that here G^* is notated as μ: they both express the same complex quantity, i.e. the shear modulus that provides a complete understanding of viscoelastic materials' behaviour by considering both the elastic and viscous responses over a range of frequencies.

In section 3.1.7 it is explained how from this equation, by assuming pressure component is negligible ($\nabla \cdot \boldsymbol{u} = 0$), PDE is reduced to its heterogeneous form; by assuming local homogeneity of the complex shear modulus ($\nabla \mu = 0$), Helmholtz equation emerges (Table 1).

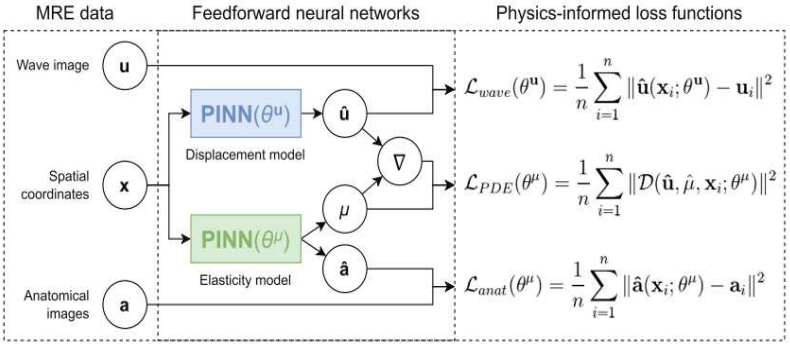

Figure 17: One PINN learns to map from spatial coordinates to displacement vectors by fitting to the wave image, while another learns to recover the shear elasticity at the corresponding position by minimizing a PDE residual. The elasticity model can also predict anatomical MRI features that are correlated with elasticity. Adapted from "Physics-Informed Neural Networks for Tissue Elasticity Reconstruction in Magnetic Resonance Elastography" from Ragoza et al, 2023 Springer eBook. @2023, Springer Nature. Used with permission.

PINN structure is presented in Figure 17. Two independent networks are effectively used, each one separately approximating a field variable to obtain accurate solutions [92]. One first NN

$\hat{\mathbf{u}}(\mathbf{x}, \theta^{\mathbf{u}})$ maps spatial coordinates $\mathbf{x}$ to displacement field $\mathbf{u}$ and forces the model to fit displacement provided data minimizing the loss function $\mathcal{L}_{\text{wave}}$. The second NN $\hat{\mu}(\mathbf{x}, \theta^{\mu})$ maps spatial coordinates $\mathbf{x}$ to stiffness field μ: output heads $\hat{\mu}$ and $\hat{\mathbf{u}}$ are then combined to minimize the residual of a PDE, defined as a differential operator D in Figure 17, minimized as a loss function $\mathcal{L}_{\text{PDE}}$. It ensures that the model adheres to the associated PDE: the lower it is, the better the PDE fit (see Table 1). T1w MRI is introduced with an additional output head $\hat{\mathbf{a}}(\mathbf{x}, \theta^{\mu})$ on the second NN and another optional loss function $\mathcal{L}_{\text{anat}}$ takes into account anatomical features forcing the model to fit and gain information from anatomical data.

Each network has five layers with 128 neurons; initialization is based on SIREN architecture and activation functions for both networks are sine to better represent high spatial frequencies [101] (Table 2).

The overall PINN loss function is composed of multiple terms: $\mathcal{L}_{\text{wave}}$, $\mathcal{L}_{\text{PDE}}$ and $\mathcal{L}_{\text{anat}}$.

$$\mathcal{L}(\theta^{\mathbf{u}}, \theta^{\mu}) = \lambda_{\text{wave}}\mathcal{L}_{\text{wave}}(\theta^{\mathbf{u}}) + \lambda_{\text{PDE}}\mathcal{L}_{\text{PDE}}(\theta^{\mu}) + \lambda_{\text{anat}}\mathcal{L}_{\text{anat}}(\theta^{\mu}) \tag{28}$$

$$\mathcal{L}_{\text{wave}} = \frac{1}{n}\sum_{i=1}^{n} |\hat{\mathbf{u}}(\mathbf{x}_i, \theta^{\mathbf{u}}) - \mathbf{u}_i|^2 \tag{29}$$

$$\mathcal{L}_{\text{PDE}}(\theta^{\mu}) = \sum_{i=1}^{n} |D(\hat{\mathbf{u}}, \hat{\mu}, \mathbf{x}_i, \theta^{\mu})|^2 \tag{30}$$

$$\mathcal{L}_{\text{anat}}(\theta^{\mu}) = \frac{1}{n}\sum_{i=1}^{n} |\hat{\mathbf{a}}(\mathbf{x}_i, \theta^{\mu}) - \mathbf{a}_i|^2 \tag{31}$$

Each one is multiplied by its relative weight: λ_{wave}, λ_{PDE}, and λ_{anat} represent the contribution of each loss term to the total cost function and to the training process. They will be denoted as loss weights and should be minimised simultaneosuly within a multiobjective optimization structure: it is necessary to properly balance loss terms with effective solvers that deal with imbalance between PDE and data losses and with the discrepancy between loss function and actual performance [13]. Algorithms that iteratively adapts these weights can be developed to balance efficiently the different objectives, on which a section of this work focuses (Section 6.2.1).

N. layers	N. neurons per layer	Weights initialization	Activation function	Loss	Optim.	Learning rate	Batch size	Loss weights
5	128	Siren	sin()	MSE	adam	1,00E-04	1024	[1, 0, 0, 1e-8]

Table 2: Table of PINN parameters

Loss optimization is carried out through Adam algorithm, with learning rate set to 1e-4 and batch size to 1024. All networks parameters of interest are reported in Table 2. Loss weights do not adapt during training but are fixed on initial values. In this table, they are expressed as a list of four values, because one of the PINN configurations tested in this work includes a further optional loss $\mathcal{L}_{\text{stiff}}$ designed to fit a pre-computed stiffness map. This will be thoroughly explained in section 5.2.3.

Displacement data to train the network are computed from the simulated stiffness box (Figure 18) by directly applying viscoelastic equations (forward problem). Once extracted, displacement maps are the only input data for the PINN, because spatial coordinates are automatically computed once provided the resolution numerical value and T1w MRI anatomical data are not avaliable for this viscoelastic box (see Figure 17).

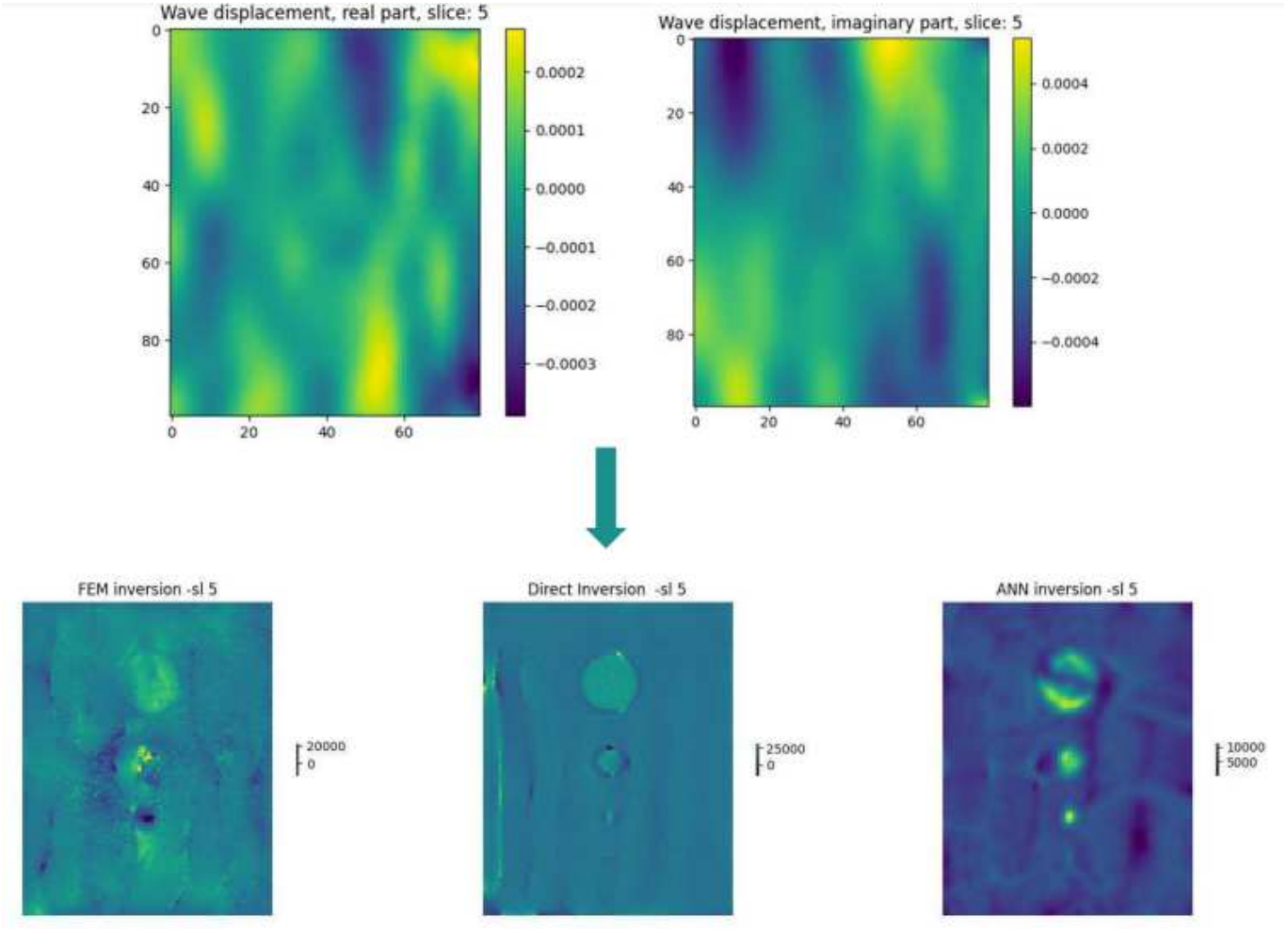

Figure 18: Stiffness maps can be retrieved from displacement with different inversion methods (ground truth stiffness in Figure 16)

.

Magnitude	DIRECT	FEM	PINN
MAV	1465.11	1568.88	850.19
RMSE	2734.03	1999.48	1293.89
MAXE	47035.35	21338.11	14917.67
SSIM	0.26	0.15	0.40
PSNR	9.88	11.34	16.52
R^2	0.54	0.43	0.76

Table 3: Evaluation metrics for three methods of MRE inversion.

The estimated stiffness map with FEM, Direct and PINN methods, once training is completed, are shown in Figure 18 and 19 (ground truth stiffness in Figure 16) and some evaluation metrics are reported in Table 3. It's evident that PINN inversion reconstructs more accurately the simulations and outperforms DI and FEM for all performance metrics. To have a detailed explanation of metrics computed, see section 5.2.1.

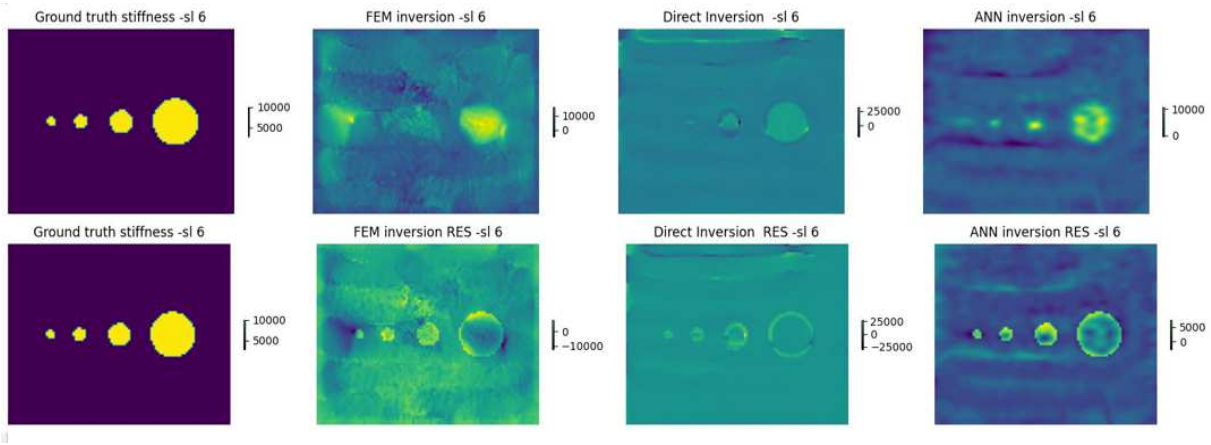

Figure 19: stiffness estimates (above) and residuals (below) for FEM, DI and PINN inversions

To compute parameters gradients when training neural networks, PyTorch has a built-in differentiation engine [102] called torch.autograd that supports automatic computation of gradient for any computational graph [5]: the continuous displacement representation of these data allow to use this autodifferentiation engine in Pytorch v1.12.1. and DeepXDE v1.5.1. DeepXDE is library for scientific and physics-informed learning [103] [6]

[5] https://pytorch.org/tutorials/beginner/basics/autogradqs_tutorial.html
[6] https://deepxde.readthedocs.io/en/latest/user/cite_deepxde.html

Before this reference study, most reconstruction techniques were primarily validated against in silico or in vitro phantoms [31]. In contrast, the novel approach introduced in this study was rigorously evaluated on both simulated phantoms, such as the viscoelastic stiffness box from BIOQIC, and real in vivo liver data. This dual validation enhances the credibility and applicability of the results, demonstrating a significant advancement over previous methodologies. In simulations, robustness to noise was tested and PINN demonstrated superior performance compared to both FEM and Direct inversions, maintaining higher reconstruction quality even with the addition of varying levels of Gaussian noise. For in vivo liver data, abdominal MRE was obtained from a study at the University of Pittsburgh including patients with NAFLD and they found that anatomical information from other MRI sequences can be leveraged to improve significantly reconstruction fidelity.

Figure 19 shows results of three stiffness reconstruction for one slice of this viscoelastic box (above) and correspondent residuals (below). The first images on the left (below and above) represent the reference standard.

5.1.2 Reference study: Direct Inversion

In order to compare PINN predictions and performances with state-of-the art inversion approaches, the reference study [10] also provides a code to apply Direct and Finite Element Inversion to the same displacement data used to train the PINN and, from this, estimate stiffness. The same algorithms and the same comparisons will be applied in the training and testing study of the current work.

DI method discussed in [5] is implemented: the central hypothesis of this work is that mechanical properties can be obtained by direct local inversion of a differential motion equation using local polynomial fits, with estimates of derivatives based on finite-window filters. The method transforms harmonic motion equation for isotropic materials into an algebraic equation that can be inverted to obtain an estimate of Lamè coefficients (λ and μ) for each position and frequency. Estimates of derivatives of noisy displacement data are carried out with a least-square fitting procedure by Saviitsky and Golay (Savgol) that fits data to 2^{nd} or 3^{rd} order polynomials in a local window, and computes derivatives of the best-fit polynomials [104]. Due to the inherent challenges in estimating reliably both Lamé coefficients, as detailed in Section 3.1.7, full incompressibility is assumed. Results from simulations and experimental displacement data show accurate quantification of wave parameters.

In Ragoza's code, data are also preprocessed before this DI implementation [5] using a Despeckle filter, which smoothes areas in which noise is noticeable while leaving complex areas untouched [7]. A DI-inverted complex stiffness field is returned, with polar complex representation. Since the DI approach involves ultimately a division with a denominator possibly near zero to estimate Lamè coefficients, an arbitrary low numerical value ϵ is introduced to avoid zero division.

5.1.3 Reference study: FEM Inversion

The notebook implements also the more accurate and efficient FEM inversion presented in [105]. The paper presents a novel flexible and general method to create arbitrary degree-of-freedom (DOF) maps for finite element spaces on various cell shapes, such as polygons, polyhedra or mixed cell. To ensure that the DOF maps are consistent across cells, which is crucial for accurately solving mathematical problems when using FEM, the authors propose a new method where neighboring cells of a FEM space agree on the layout of DOFs, such as vector orienta-

[7] `https://www.websupergoo.com/helpie/default.htm?page=source\%2F2-effects\%2Fdespeckle.htm`

tions on shared edges or faces. Overall, the paper introduces a more efficient and versatile way to manage DOFs in FEM analysis, making it easier to apply this method to complex geometries and higher-order problems. The method has been implemented in the open-source FEniCSx libraries [8], specifically in DOLFINx and Basix, which are tools used for finite element analysis.

Ragoza's code uses the same packages [10] and implements the same method to evaluate a FEM baseline for MRE data inversion, which will be used for comparison with other methods.. The function processes a wave field (potentially 3D) slice by slice along the z-axis. For each z-slice, it solves the FEM problem using the specified frequenc, evaluates the solution on the domain interior and combines the result of the whole volume. The FEM type implemented to efficiently handle heterogeneous materials has CG-3 elements for displacement, DG-1 elements for material property [106], node alignment with data points and no mesh scaling [105].

[8] `https://github.com/FEniCS`

5.2 Training study: methods

Before testing the network on patients brain data, data of a MRE phantom acquisition from Charité-Universitätsmedizin Berlin Germany will be used to pretrain the PINN. The MRE phantom data are reported in [88] and [107], and briefly descripted here.

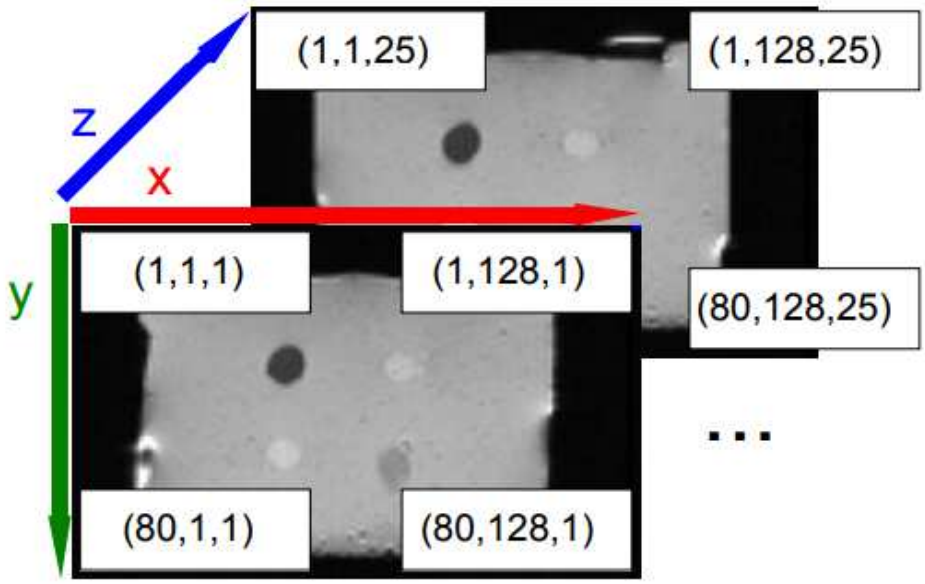

Figure 20: Pixel coordinates for MRE phantom acquisition

Shear modulus μ in kPa				
Matrix	Inclusion 1	Inclusion 2	Inclusion 3	Inclusion 4
1:3	1:1	1:4	1:3.5	1:2
10.830	43.301	5.228	6.001	16.281

Table 4: Table of matrix and inclusions storage modulus

The phantom is made from agar-based Wirogel (Bego Inc., Germany), has a size of 0.135 x 0.135 x 0.1 m^3 and contains four parallel cylindrical inclusions of a diameter of 12 mm. Gel/water ratios are 1:3, 1:1, 1:4, 1:3.5 and 1:2 in the matrix and inclusion 1 to 4, respectively. Viscoelastic parameters of inclusions and phantom matrix are reported in Table 4. The data were acquired in a 1.5 T scanner using a single-shot spin-echo EPI sequence with a sinusoidal MEG. Seven harmonic actuation frequencies were tested between 30 Hz and 100 Hz. Training data for this work were acquired with 60 Hz. For a complete description of MRE phantom data and imaging parameters, see *Downloads* section of BIOQIC site. [9].

[9] https://bioqic-apps.charite.de/downloads

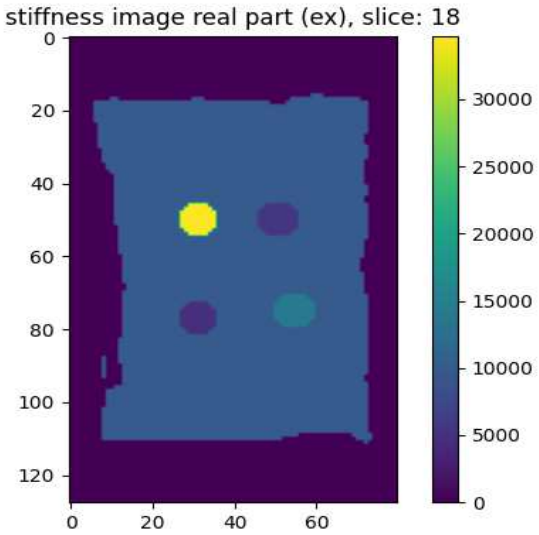

Figure 21: Storage Modulus (in Pa) measured in one MRE phantom slice with 60 Hz actuation frequency

.

The same PINN structure and assumptions presented in the reference work will be adopted for this training study: Adam optimization scheme will be followed and training will be stopped manually when the total loss and each single loss term do not improve and are stable with little oscilation.

Both Helmholtz and heterogeneous equations will be used in the model PDE term (see Table 1). Results of this step will be compared with algorithms of FEM and direct methods, presented in sections 5.1.2 and 5.1.3 and implemented in the reference study. A set of evaluation metrics presented in the next section will be adopted (section *Evaluation metrics*). First-PDE strategy will be used (section *First-PDE training*) for all the PINN configurations investigated in this training study. In addition, PINN structure will be adapted to include a further optional loss $\mathcal{L}_{\text{stiff}}$ designed to fit precomputed stiffness (section *Including prior Direct Inversion*)

5.2.1 Evaluation metrics

In these training study and subsequent testing study, performances of PINN, FEM and DI stiffness reconstructions will be compared evaluating difference and correlation with a ground truth. Stiffness values in Figure 21 will be taken as reference standard for these MRE phantom inversions. For each network configuration tested, the following evaluation metrics will be reported: MAE (Mean Absolute Error), MSE (Mean Square Error) , rMSE (root Mean Square Error), mERR (maximum Error) , SSIM (Structural Similarity Index), PSNR (Peak Signal to Noise Ratio).

$$\text{MAE} = \frac{1}{n}\sum_{i=1}^{n}|y_i - y_i'| \tag{32}$$

$$\text{MSE} = \frac{1}{n}\sum_{i=1}^{n}(y_i - y_i')^2 \tag{33}$$

$$\text{rMSE} = \sqrt{\frac{1}{n}\sum_{i=1}^{n}(y_i - y_i')^2} \tag{34}$$

$$\text{mERR} = \max_i |y_i - y_i'| \tag{35}$$

$$\text{SSIM}(y, y') = \frac{(2\mu_y\mu_{y'} + C_1)(2\sigma_{yy'} + C_2)}{(\mu_y^2 + \mu_{y'}^2 + C_1)(\sigma_y^2 + \sigma_{y'}^2 + C_2)} \tag{36}$$

$$\text{PSNR} = 20\log_{10}\left(\frac{y_{\text{max}}}{\sqrt{\text{MSE}}}\right) \tag{37}$$

where:

$y_i =$ the voxel value of the ground truth image

$y'_i =$ the voxel value of the model image

$n =$ total number of voxels

$\mu_y =$ mean of y

$\mu_{y'} =$ mean of y'

$\sigma_y^2 =$ variance of y

$\sigma_{y'}^2 =$ variance of y'

$\sigma_{yy'} =$ covariance of y and y'

$C_1 = (K_1 L)^2, K_1 = 0.01$ by default

$C_2 = (K_2 L)^2, K_2 = 0.03$ by default

$L =$ the dynamic range of the pixel-values (typically this is$2^{\text{num bits for voxel}} - 1$)

$y_{\text{max}} =$ the maximum value of the evaluated image

SSIM [108] and PSNR [109] are two widely used metrics for assessing the images quality used to compare the similarity between an original image and an estimated image.

SSIM is designed to measure the perceived quality of images by considering changes in structural information, which is more aligned with human visual perception than simple pixel-by-pixel differences. SSIM values range from -1 -1 to 1 1, where: 1 indicates perfect similarity (i.e., the images are identical). 0 indicates no structural similarity. Negative values can occur but are rare and typically indicate structural dissimilarity.
SSIM is more sensitive to changes that are perceptually important (like structure and texture) than simple metrics like MSE.

PSNR is an engineering term that quantifies how much noise or distortion is present in the image relative to the original. PSNR is based on the MSE and is expressed in decibels (dB): higher PSNR values indicate better quality, with less distortion, lower PSNR values indicate more noise or distortion. Typical ranges are [20 dB-50 dB], meaning good quality for most applications, and [0-15 dB], indicating poor quality and noticeable degradation. PSNR is simple to compute and widely used, making it easy to compare results across studies.

They both will be computed for each slice and averaged for the whole volume to assess similarity

between reconstructed and true stiffness. Two loss functions will be considered: MSE loss and L2RE ($\mathcal{L}_2$) Relative Error (L2RE) loss.

$$\mathcal{L}_{\text{2RE}} = \sqrt{\frac{\sum_i (y_i - y_i')^2}{\sum_i (y_i')^2}} \tag{38}$$

$$\mathcal{L}_{\text{MSE}} = \frac{1}{n} \sum_{i=1}^{n} (y_i - y_i')^2 \tag{39}$$

Computational training time will be also reported. For relevant results, images of loss decays, stiffness reconstructions and ground truth, PDE loss gradient and histogram of MAV volumes will be shown.

5.2.2 First-PDE training

In some empirical trials, starting the training procedure immediately with all the loss terms simultaneously causes the PDE loss to struggle with convergence. To solve this pathology, a strategy will be adopted for all the PINN configurations tested: start with training only PDE loss term for few epochs to force the network to fit physics equations and subsequently introduce additional loss terms in a multiobjective optimization. Pseudocode for this strategy, that will be indicated as ”first-PDE training”, is avaliable in Figure 22.

```
PSEUDOCODE FOR FIRST-PDE TRAINING STRATEGY

define lambda_PDE_init=1

set lambda_wave=0, lambda_anat=0
set lambda_PDE=lambda_PDE_init
set only_pde_iters to a fixed value, such as 10000,
number of iterations of only PDE loss training (first-PDE
phase)


WHILE TRAINING

pde_iter = current_iter - only_pde_iters to check if
first-PDE is finished


if pde_iter < 0 (first-PDE phase still on):
    pass
else: (first-PDE phase ended)
   set lambda_wave, lambda_anat to their initial values
```

Figure 22: Pseudocode for first-PDE training strategy

.

The algorithm from Ragoza [10] adopted an alternative approach where the first iterations, called ”warmup phase” do not account for PDE loss term to let the network learn a good solution approximation, and subsequently the physics-based constraint is incorporated at the end of warmup phase. With the new datasets (MRE phantom and Delaware datasets) the previous strategy led to faster convergence and stabilized training.

In fact, in some training studies, PINN was first trained immediately with two loss terms (loss weights fixed: [1,0,0,1]) and secondly starting with training only PDE (starting loss weights [0,0,0,1], later loss weights [1,0,0,1]). After 300000 epochs, total training and test losses values reached with Ragoza’s strategy were respectively 2.22 e+12, 2.19 e+12, with first-PDE strategy they were one order of magnitude lower, 1.49e+11 and 1.38e+11.

5.2.3 Including prior Direct Inversions

Applying DI to displacement data is clinically feasible because it does not require any computational effort and has a guaranteed existence and uniqueness of solution. In this work, it is proposed a slightly modified PINN structure based on Figure 17, along with an adjusted loss

formulation derived from Equation 29. An additional MSE loss term is defined as $\mathcal{L}_{\text{stiff}}$ and included in order to fit DI inversion computed before building the model, which should guide training to prior stiffness values provided to the model.

$$\mathcal{L}_{\mu}(\theta^{\mu}) = \frac{1}{n}\sum_{i=1}^{n} |\hat{\mu}(\mathbf{x}_i, \theta^{\mu}) - \mu_{\text{i}}| \tag{40}$$

Total loss becomes:

$$\mathcal{L}(\theta^{\mathbf{u}}, \theta^{\mu}) = \lambda_{\text{wave}}\mathcal{L}_{\text{wave}}(\theta^{\mathbf{u}}) + \lambda_{\text{PDE}}\mathcal{L}_{\text{PDE}}(\theta^{\mu}) + \lambda_{\text{anat}}\mathcal{L}_{\text{anat}}(\theta^{\mu}) + \lambda_{\mu}\mathcal{L}_{\mu}(\theta^{\mu}) \tag{41}$$

5.3 Training Study: results

5.3.1 PINN on MRE Phantom

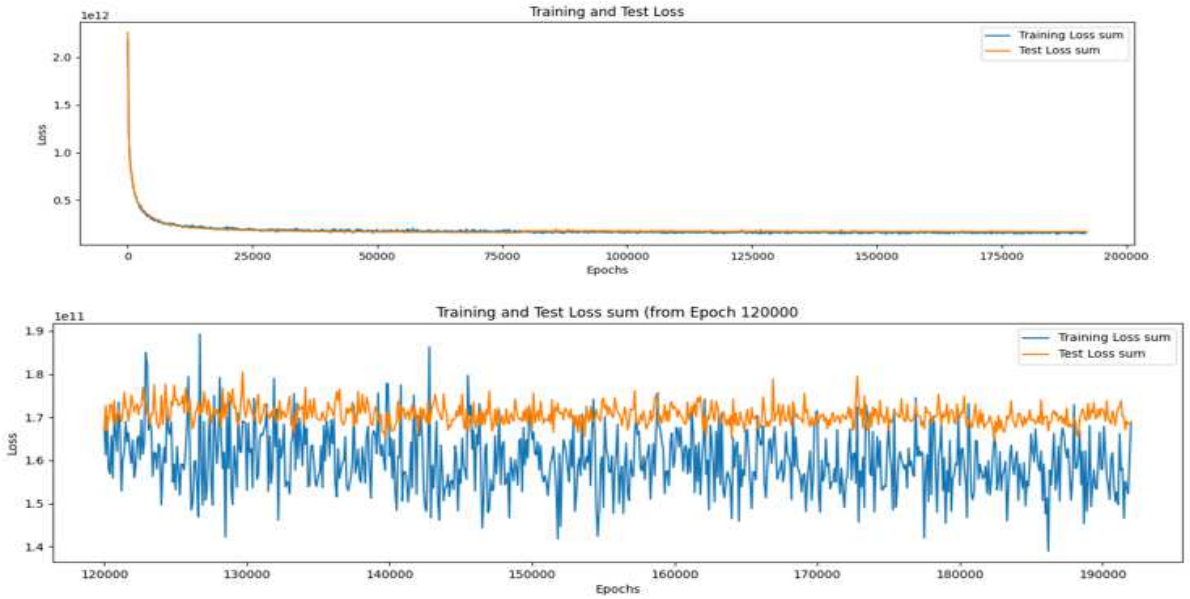

Figure 23: Loss decay for heterogeneous PINN for the whole training (above) and the last 70000 epochs.

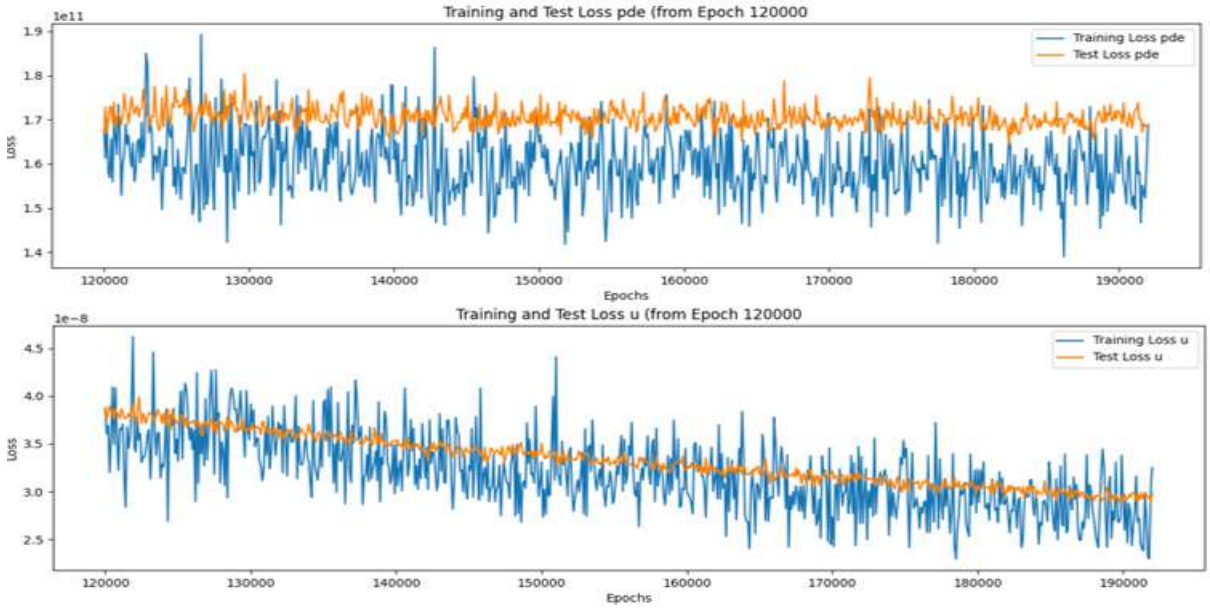

Figure 24: Displacement (below) and PDE (above) loss terms decays for heterogeneous PINN for some epochs

In Figure 23 (above), the loss drops fast to a lower value from random weights inizialization and starts to oscillate. Exactly as the PINN implemented in [81] for a mechanical problem inversion, all terms in the loss, i.e., data-driven and physics informed, show oscillations during the optimization: there is not one single loss responsible for total loss instability. These oscilla-

tions are attributable to the stochastic nature of SGD optimization that Adam executes, because minibatch gradients are noisier than whole-dataset batch but much more time-efficient and on average make good progress.

Without Direct Inversion as prior stiffness				
Magnitude(Pa)	**DIRECT**	**FEM**	**PINN (het)**	**PINN (homo)**
MAV	2861,17	3011,31	2716,03	2967,92
RMSE	5165,75	4882,53	4491,31	5145,17
MAXE	41112,72	34209,04	34042,27	38757,17
SSIM	0,48	0,51	0,6	0,44
PSNR	17,9	17,07	17,92	17,33
R^2	0,54	0,51	0,62	0,48
Real(Pa)				
MAV	2604,93	2999,68	2664,49	2815,29
RMSE	4926,98	4870,66	4442,92	5000,21
MAXE	40988,59	34116	33938,08	38660,95
Imaginary(Pa)				
MAV	725,66	216,81	293,77	549,43
RMSE	1552,34	340,3	657,56	1212,68
MAXE	24429,11	2513,22	8857,33	21575,18
Angle(rad)				
MAV	0.095 π	0.022 π	0.019π	0.064π
RMSE	0.229π	0.124 π	0.070 π	0.175π
MAXE	2π	2π	2π	2π

Table 5: Evaluation metrics for various inversion methods.

Computational time required	**Direct**	**FEM**	**PINN**
(s)	0.897	50.263	66.240.827
(h)	2.5e-4	0.014	18.4

Table 6: Computational time required for the inversion methods.

Table 5 shows evaluation metrics for Direct, FEM, PINN with homogeneous PDE (PINN (homo)) and PINN with heteregeneous PDE (PINN (het)). This last outperforms FEM and Direct inversions for all the performance metrics, as well as homogeneous PINN, for magnitude, real and imaginary parts. Image similarity of PINN heterogeneous inversion with ground truth is the highest and correlates well (0.62) with it. On the other side, Table 6 shows computational times required for computing direct inversion, for extraction FEM stiffness prediction and for training the network: PINN learning takes far much time, but once trained the network, prediction of a new volume should take just a forward pass through the network (~1min). Figure 25 shows

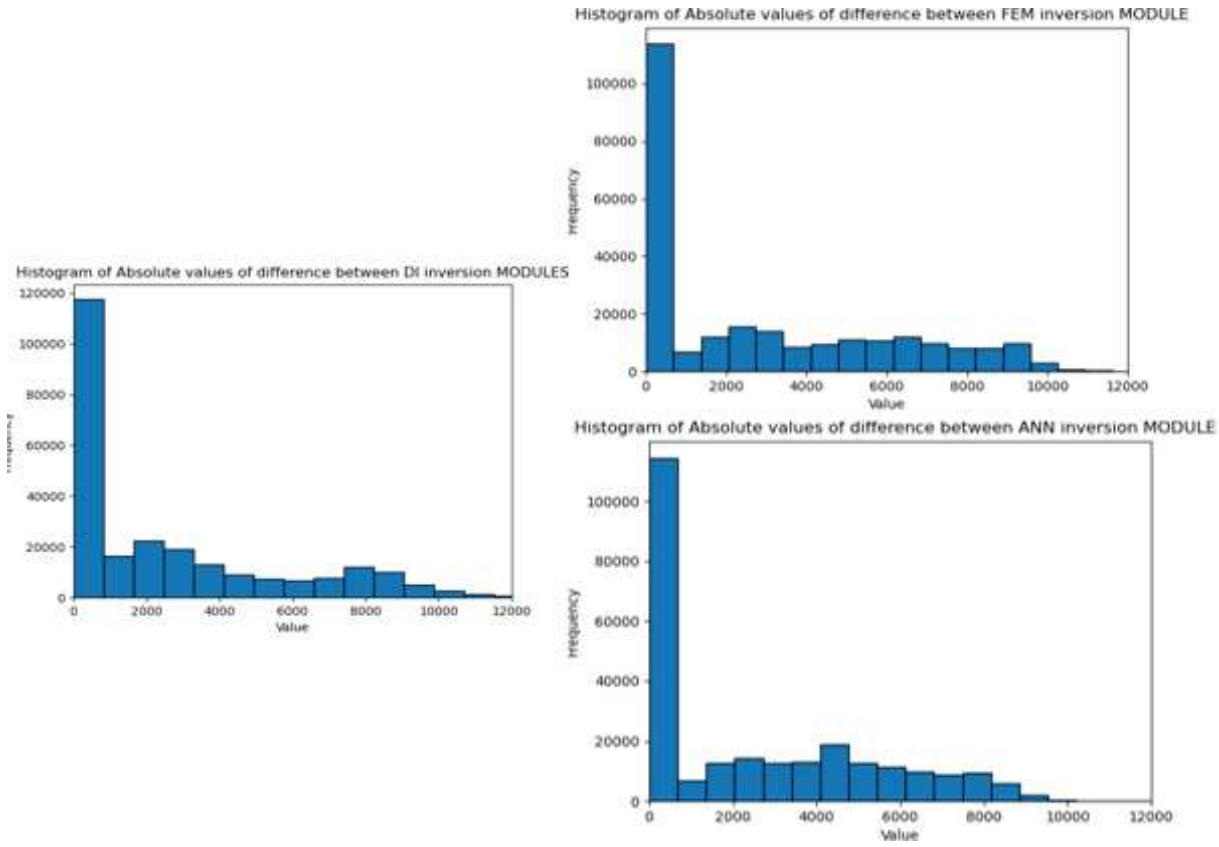

Figure 25: Histograms of $|G^*|$ differences between prediction and ground truth: DI (left), FEM (right above), PINN (right below)

histograms of MAVs of the magnitude of the complex shear modulus $|G^*|$ for the three inversion methods, while Figure 26 shows $|G^*|$ predictions and residuals. From these predictions one can realize the challenges of handling noisy data and capturing the hidden mapping between the two fields for all the methods proposed, even when applied to a relatively simple phantom model with four inclusions. All these predictions are prone to fail when strong stiffness discontinuities are present.

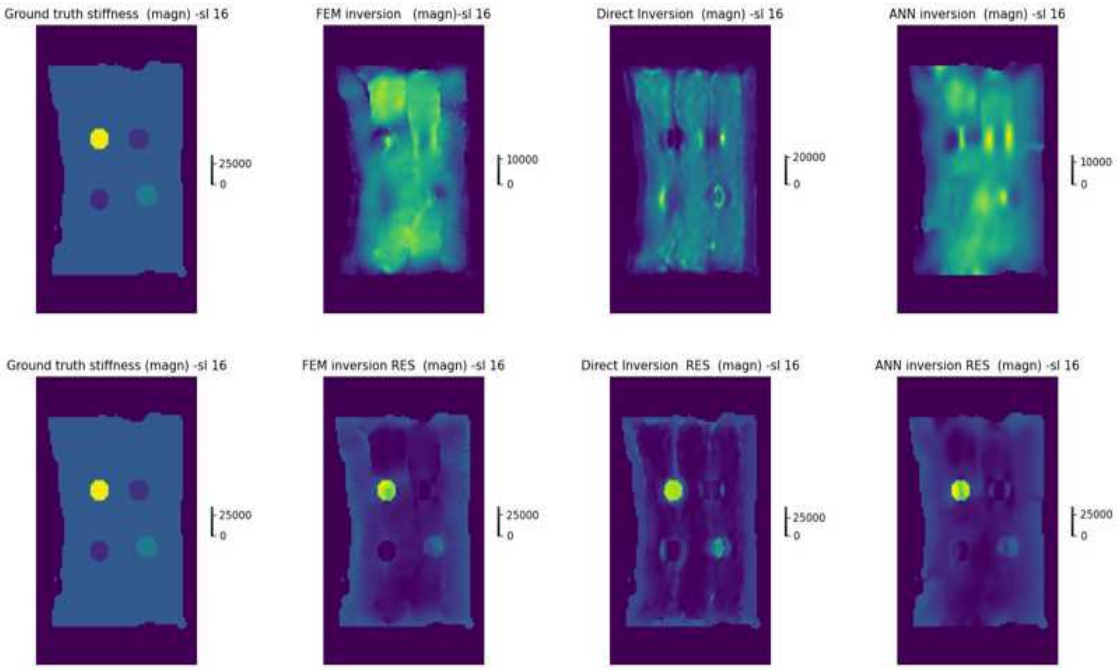

Figure 26: |*G**| stiffness estimates (above) and residuals (below) for FEM,DI and PINN heterogeneous inversions

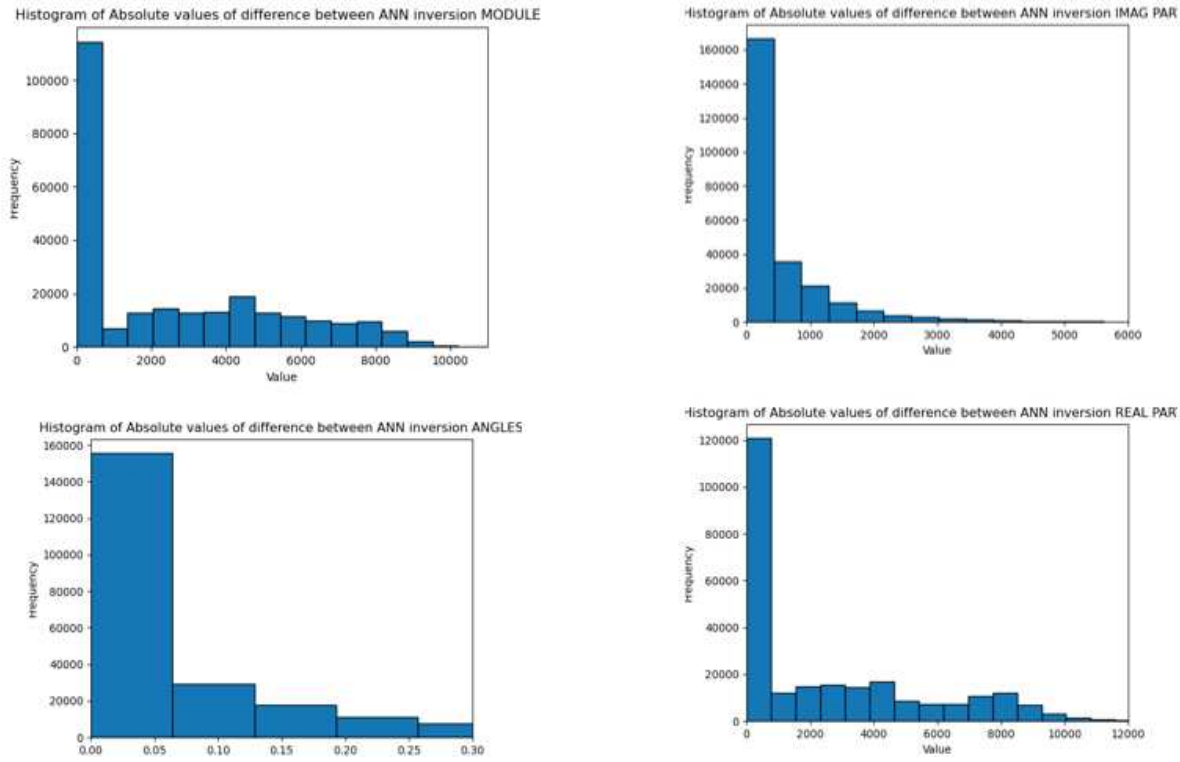

Figure 27: Histograms of differences between prediction and ground truth from heterogeneous PINN: magnitude (left above), angle (left below), imaginary and real part(right above and right below) of complex shear modulus *G**.

The following Figures refer to PINN heterogeneous predictions of the MRE phantom.

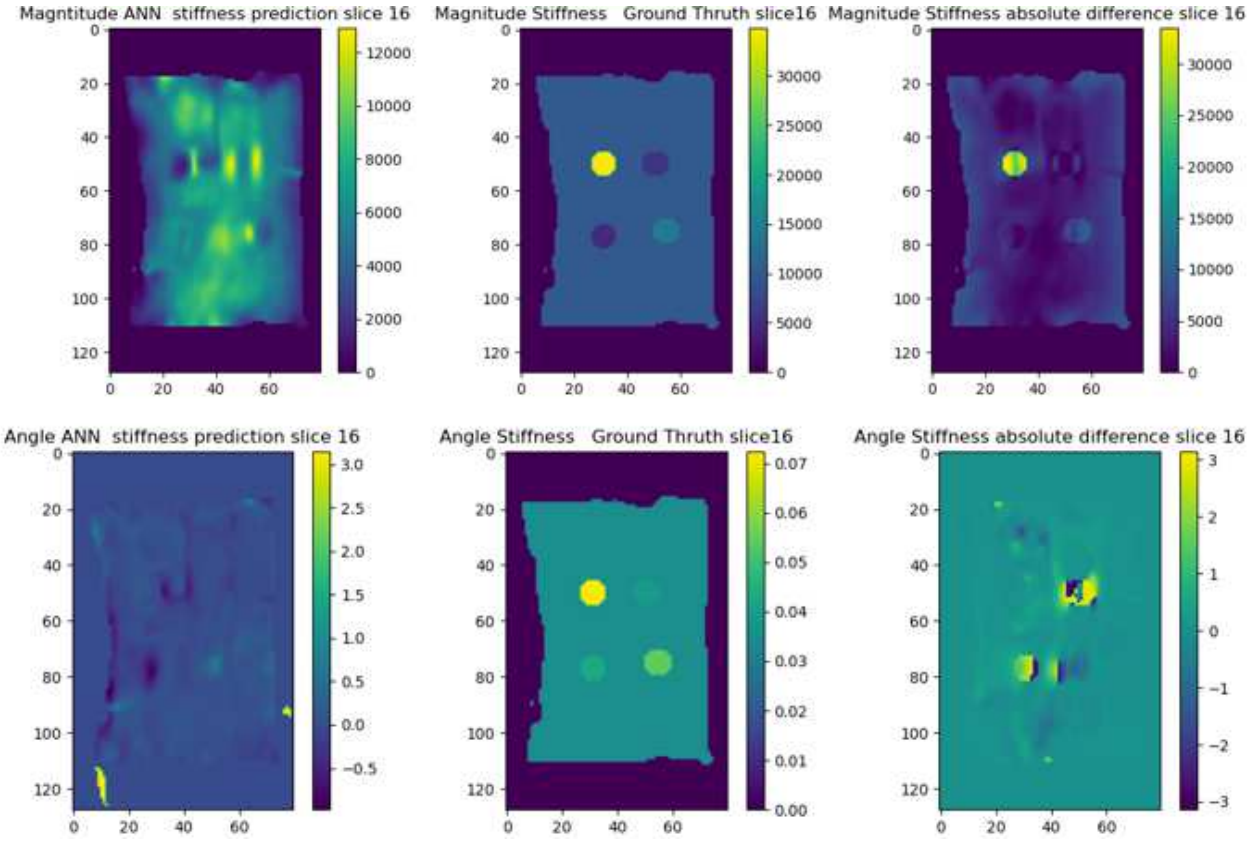

Figure 28: Magnitude and angle of complex shear modulus G^* estimates from PINN heterogeneous inversion: prediction (left), ground truth (middle) and residuals (right).

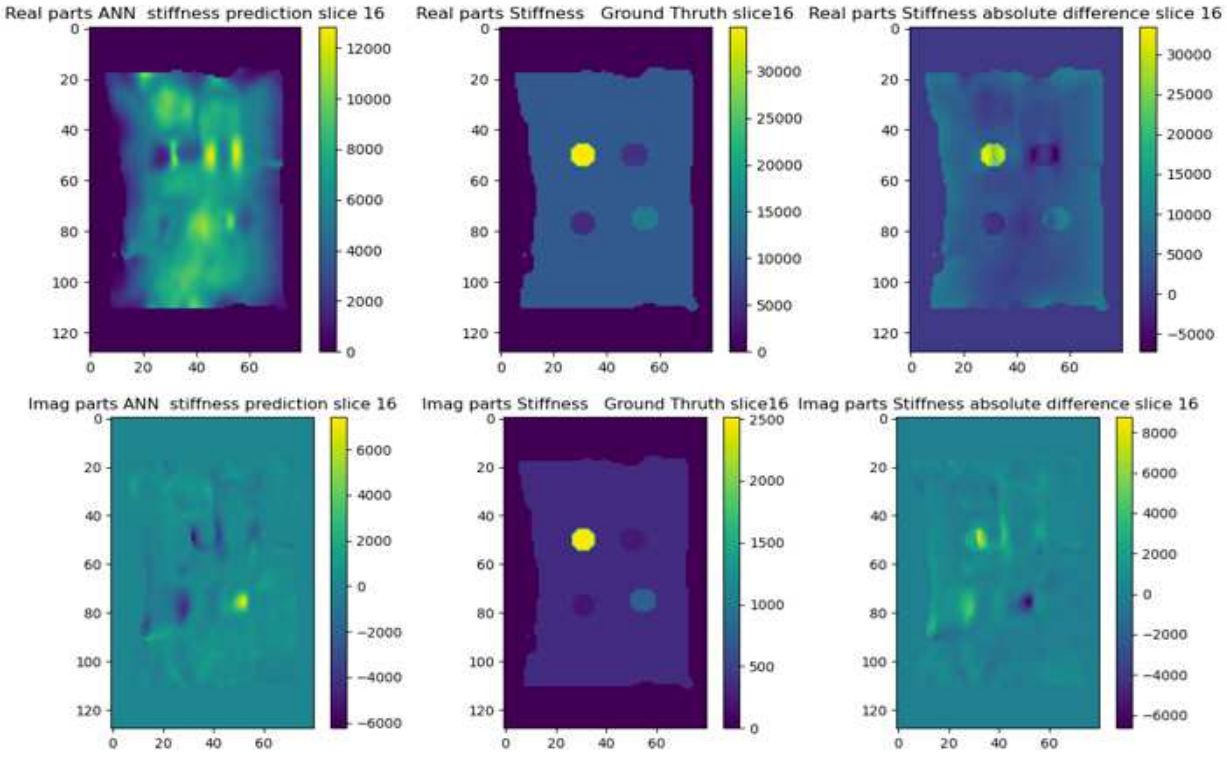

Figure 29: Real and imaginary parts of G^* estimates from PINN heterogeneous inversion: prediction (left), ground truth (middle) and residuals (right).

Figures 28 and 29 illustrate the performance of this inversion method in predicting all components of the complex shear modulus. While the technique shows potential in predicting the magnitude and real part, it fails significantly in accurately capturing the imaginar.

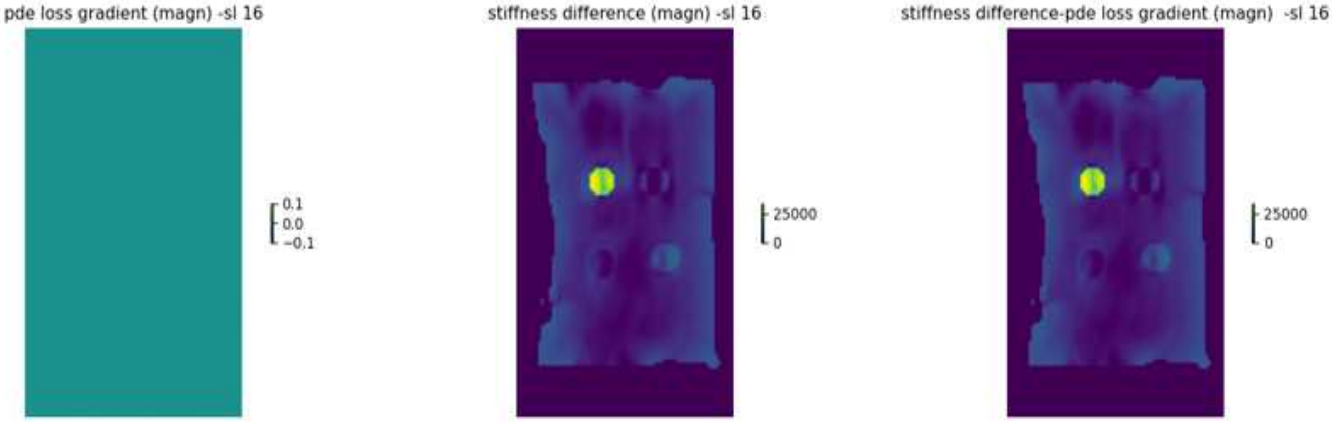

Figure 30: Spatial distribution of PDE loss gradient, difference between estimated and ground truth $|G^*|$ and relative difference between them.

To generate Figure 30, three components are calculated for one specific slice:

1. PDE loss gradient: pde_grad $= -(f_{\text{trac}} + f_{\text{body}}) \cdot \Delta\mu \cdot 2$, where $f_{\text{body}} = \rho\omega^2\mathbf{u}$ and $f_{\text{trac}} = G^*\nabla^2\mathbf{u} + (\nabla\mathbf{u} + \nabla\mathbf{u}^T)\nabla G^*$ for PINN (het), $f_{\text{trac}} = G^*\nabla^2\mathbf{u}$ for PINN (homo)
2. stiffness difference: $\mu_{\text{diff}} = \mu_{\text{true}} - \mu_{\text{pred}}$
3. difference between 1 and 2: pde_grad $- \mu_{\text{diff}}$

The purpose of computing these components is to assess the agreement between the PDE solution and errors in stiffness prediction. A zero gradient for the PDE loss should indicate that the PINN has found a solution that satisfies the PDE constraints across the entire domain. But this might also mean that PDE loss has a negligible effect on the overall loss term and doesn't significantly alter the stiffness prediction or the residuals: the model might not be sensitive to the PDE constraints, which means these are not strongly enforced during training.

Figure 32 presents estimates of magnitude and angle of G^* obtained from the PINN homogeneous inversion. It is evident that this prediction is more degraded compared to Figure 28, especially along the borders in areas of spatially varying stiffness.
PINN with heterogeneous equation has remarkably higher correlation and lower mean and maximum error values compared with the corresponding homogeneous model (Table 5).

The heterogeneous model shows clearer structures and better-defined boundaries between dif-

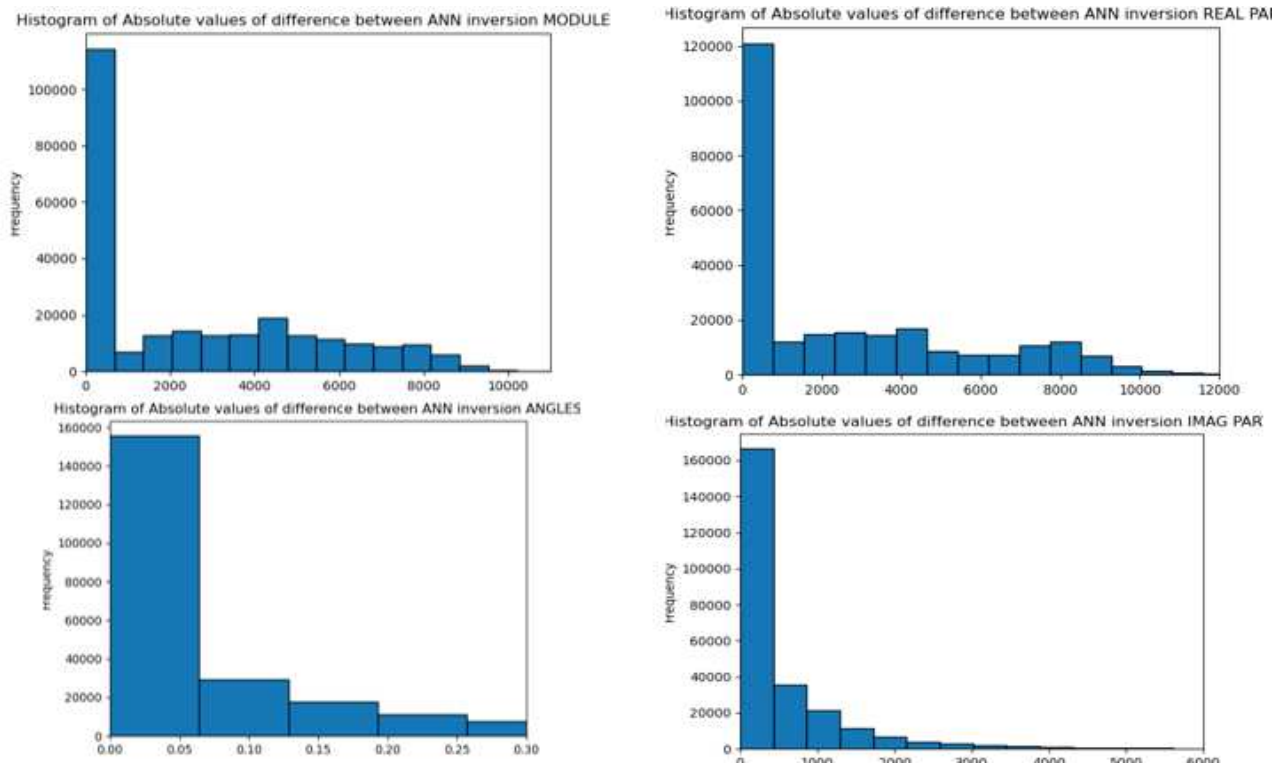

Figure 31: Histograms of differences between prediction and ground truth from homogeneous PINN: magnitude (left above), angle (left below), imaginary and real part(right above and right below) of complex shear modulus G*

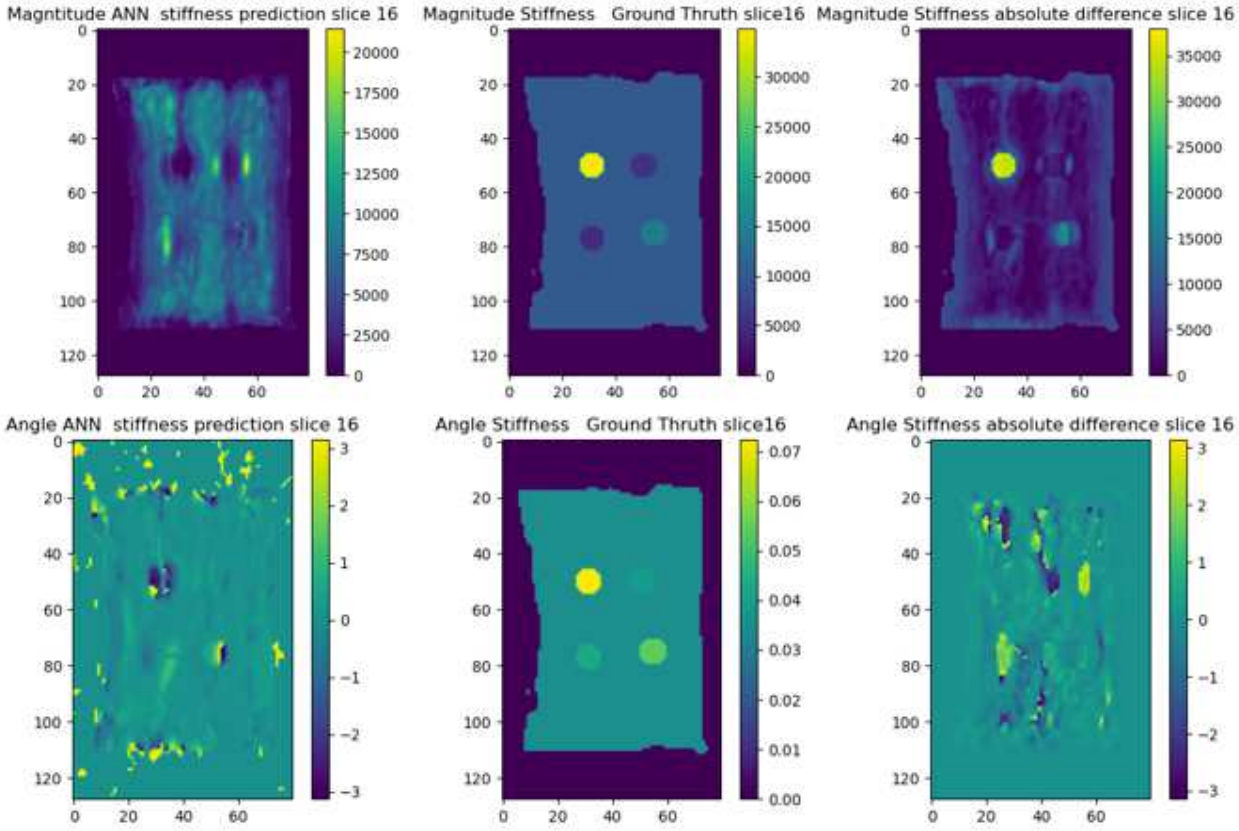

Figure 32: Magnitude and angle of *G** estimates from PINN homogeneous inversion: prediction (left), ground truth (middle) and residuals (right).

ferent regions. The magnitude prediction in Figure 27 shows more distinct regions and better corresponds to the ground truth.

5.3.2 Including prior Direct Inversions

With Direct Inversion as prior stiffness		
Magnitude(Pa)	**PINN (het)**	**PINN (homo)**
MAV	2686,06	2966,71
RMSE	4452,91	5157,05
MAXE	33876,61	38902,87
SSIM	0,59	0,44
PSNR	18,03	17,32
R^2	0,62	0,48
Real(Pa)		
MAV	2626,89	2814,16
RMSE	4397,02	5008,78
MAXE	33801,93	38799,23
Imaginary(Pa)		
MAV	307,32	548,86
RMSE	703,29	1227,7
MAXE	12055,47	23070,48
Angle(rad)		
MAV	0.022 π	0.060π
RMSE	0.076π	0.169
MAXE	2π	2π

Table 7: PINN Evaluation metrics with homogeneous and heterogeneous PDE, when including prior DI stiffness to guide training.

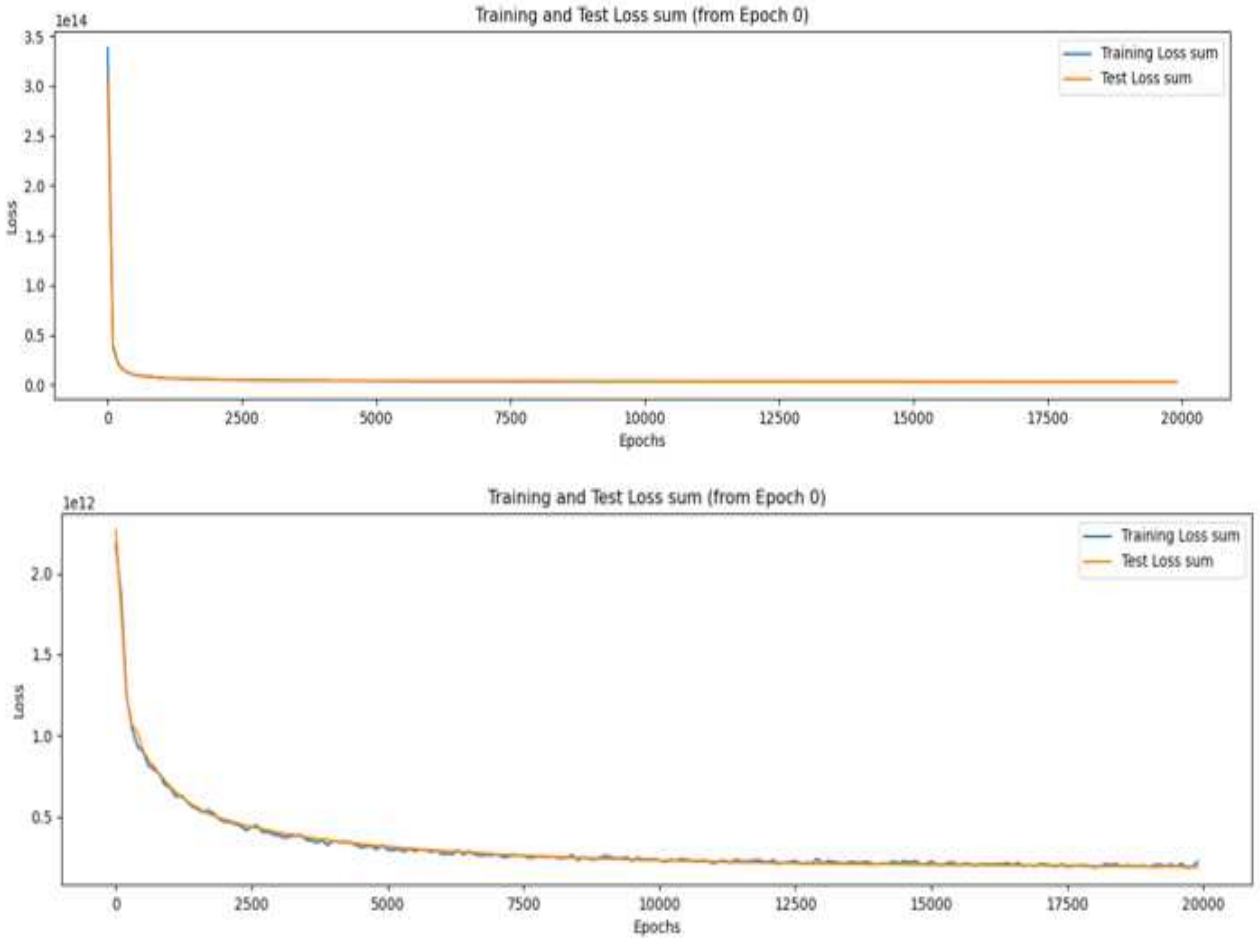

Figure 33: Loss decay (first epochs) when including (above) and not including (below) pre computed DI stiffness

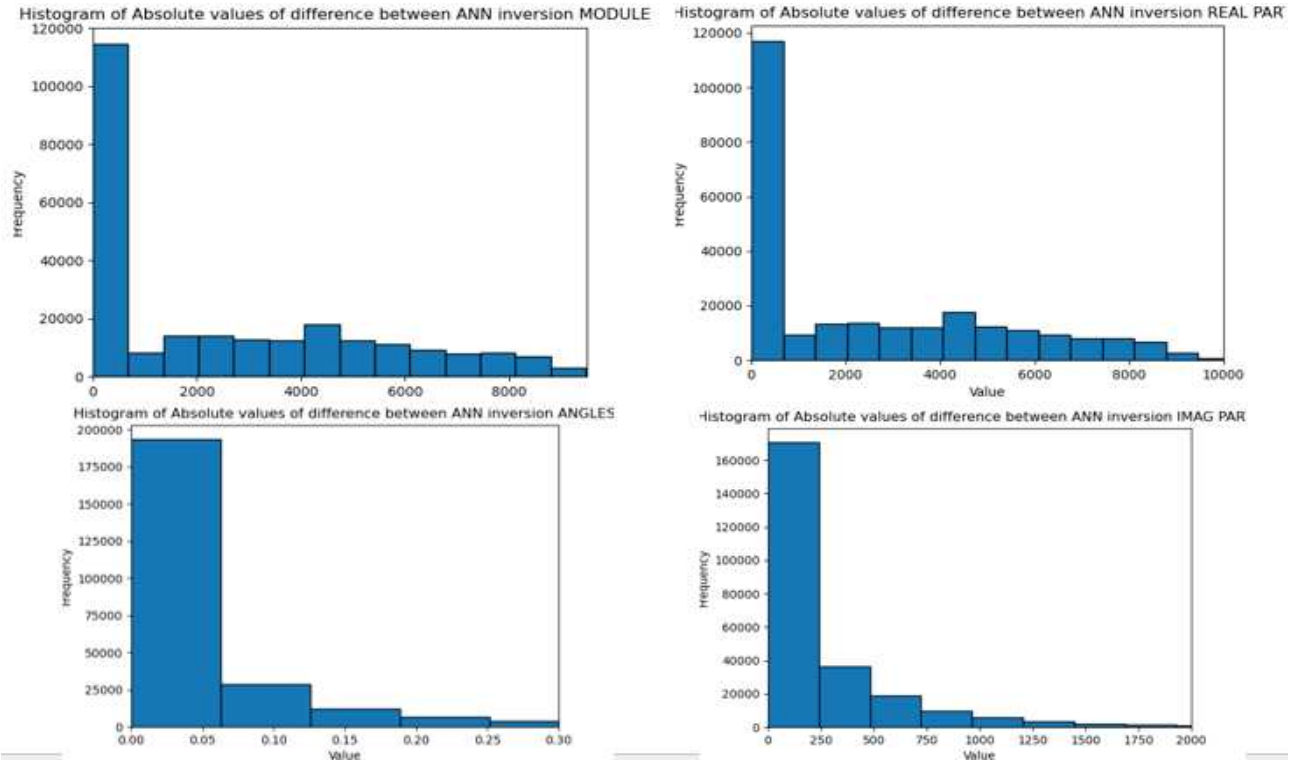

Figure 34: Histograms of differences between prediction and ground truth from heterogeneous PINN with DI prior inversion: magnitude (left above), angle (left below), imaginary and real part right above and right below) of complex shear modulus G*

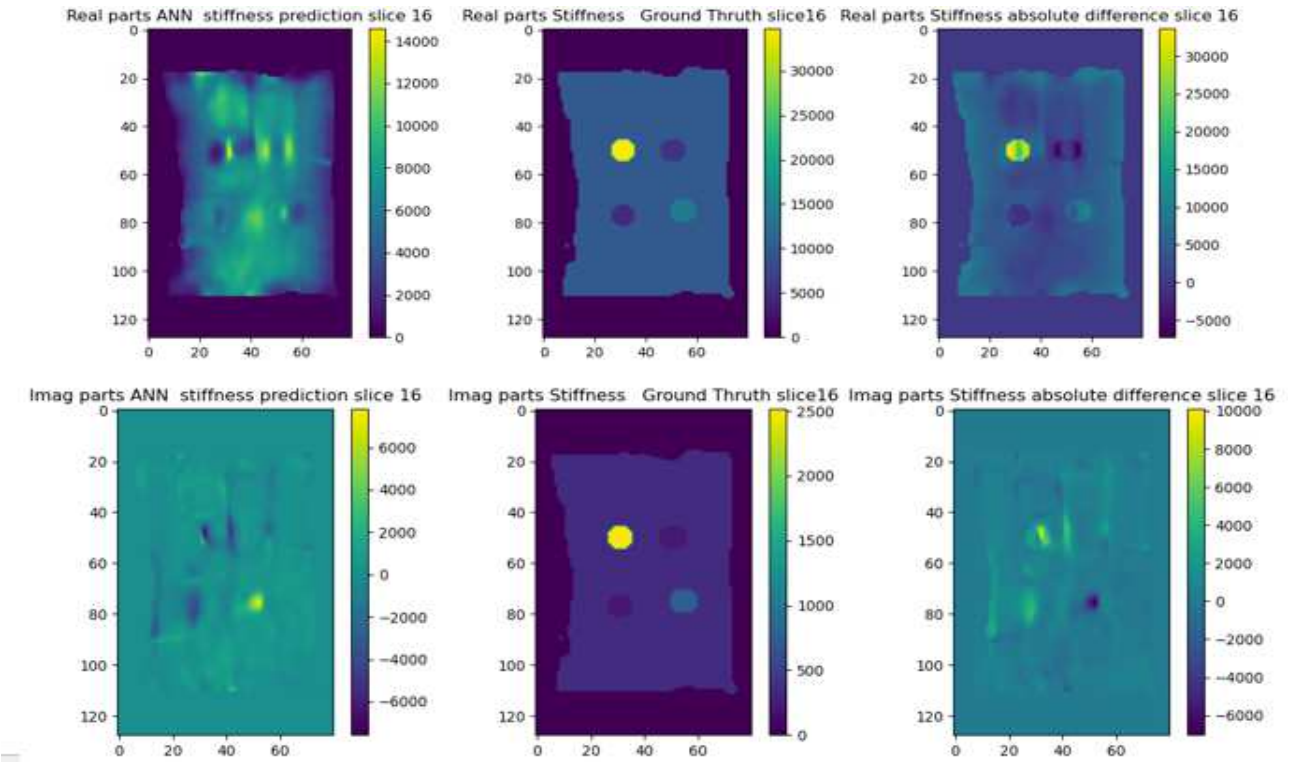

Figure 35: Magnitude and angle of *G** estimates from PINN heterogeneous inversion including DI as prior stiffness: prediction (left), ground truth (middle) and residuals (right).

Table 7 shows evaluation metrics for all the inversion methods when including DI pre computed

stiffness to guide the training process. As for homogeneous inversion, including an additional stiffness loss does not improve its performance metrics. For heterogeneous PINN, these presents a slight improvement but qualitatively the prediction (Figure 35) is almost unchanged compared to the PINN without DI inversion.

6 Testing study: Delaware Dataset

6.1 Dataset

The dataset used to test the model is publicly avaliable and provided by University of Delaware. Detailed acquisition of raw data can be found in [110], a project that collected and disseminated multiple brain datasets describing brain mechanical properties in order to provide a complete guide to develop computational Traumatic Brain Injury (TBI) brain models. Data collections made avaliable by the project should improve accuracy and utility of TBI prediction models and for this reason they also include a dataset acquired at US of whole-brain MRE displacement data obtained through a high-resolution sequence and spatially resolved maps of complex shear modulus, stiffness and damping ratio through NLI methods. MRE acquisitions allow to catch frequency-dependent behaviour of these properties in biomechanics map, that can be used to enhance subject -specific TBI models [110]. Image resolution is 1.5 mm and brain is whole covered ($240x240x120\text{mm}^3$). Images are acquired on a Siemens 3T Prisma scanner with a 64-channel head/neck coil. Vibration is introduced into brain tissues with a pneumatic actuator system and a soft pillow driver. The MRE protocol includes three actuation frequencies (30, 50, 70 Hz) but for this work only 50Hz dataset will be studies, which is standard in clinical practice.

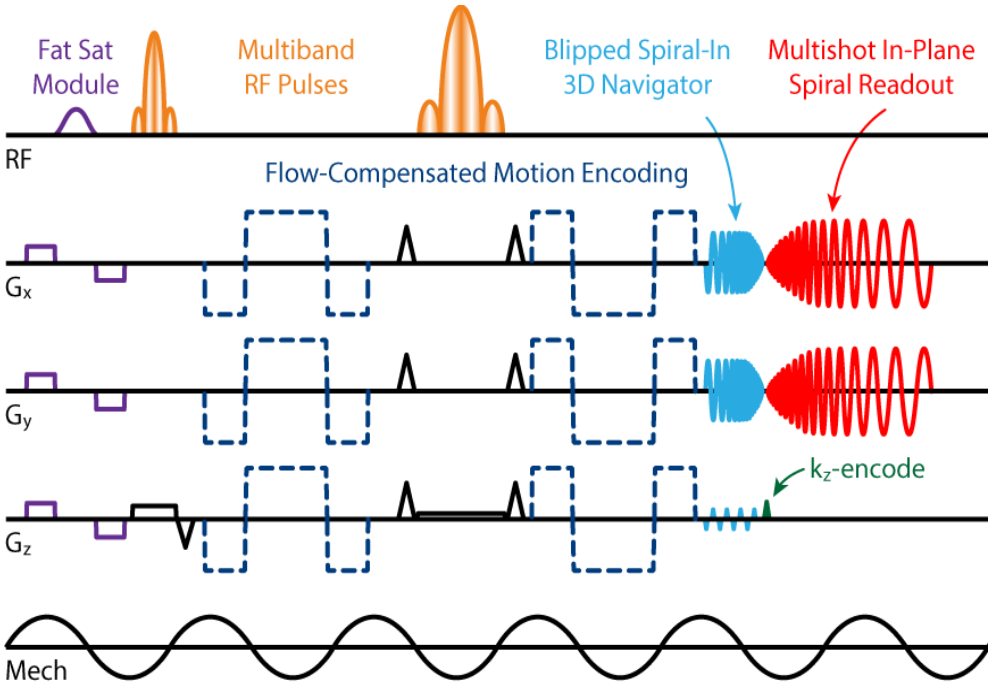

Figure 36: Proposed multiband, multishot spiral MRE pulse sequence. Adapted from "Brain MR elastography with multiband excitation and nonlinear motion-induced phase error correction" by Johnson et al, 2016, Proc. Intl. Soc. Mag. Reson. Med. 24. @2016 Proc. Intl. Soc. Mag. Reson. Med

MRE is carried out through a 3D multislab, multishot acquisition for fast, whole-brain imaging at high resolution with the protocol described in [111]. The whole volume is divided into multislice slabs, each of which is excited sequentially (a single k-space shot in a single TR) and multishot k-space sampling is accomplished through multiple TRs. This sequence grants to reach a high SNR efficiency [18], a metric that trades off repetition time TR and the number of excitations N_{ex}.

Features of the Delaware dataset MR sequence (Figure 36) are accurately explained in [111] and here briefly explained:

- multiband excitation and refocusing pulses (orange) that result in a reduced number of imaging volume and allows to reach a short TR and high SNR efficiency.
- flow-compensated motion encoding compensated for phase error correction (dashed blue). MRE multishot 3D k-space encoding need correction for motion-induced phase error arising from shot-to-shot variations in the acquired phase and causing artifacts when shots are combined; these acquisition need an appropriate navigator acquisition to correct for trajectory shifts in kx, ky, and kz.
- blipped spiral-in 3D navigator to perform nonlinear phase correction not handled by linear correction, like cardiac pulsation.
- multishot in-plane spiral readout describing k-space trajectory : in-plane k_z -blips followed by a 3D constant density stack-of-spirals.

Delaware dataset also provides, for each subject, a volume of computed storage modulus *G'* and loss modulus *G"*. These will be used in this work as the ground truth complex stiffness for all the networks tested. The viscoleastic parameters were estimated from the acquired MRE displacement data using NLI methods implemented in [112]. This work implements and evaluates a subzone based multiresolution FE that provides a flexible and robust framework where each estimated mechanical parameter can have its own resolution and stiffness estimates are extremely stable to noisy displacement data.

Hence for both the training phantom and the testing patient datasets, MRE displacement acquisition data are available as well as a reliably estimated stiffness map, adopted as ground truth to compute evaluation metrics and visually assess estimates. The results obtained from the training study on a simple phantom with four inclusions are expected to be reproducible for brain slices with a much more complex stiffness distribution. Only for Delaware dataset, conventional MRI anatomical images are also available and this allows to introduce in the model this information

in the training study.

In Figure 37, a comparison of displacements and stiffness data of the two studies of this work is shown.

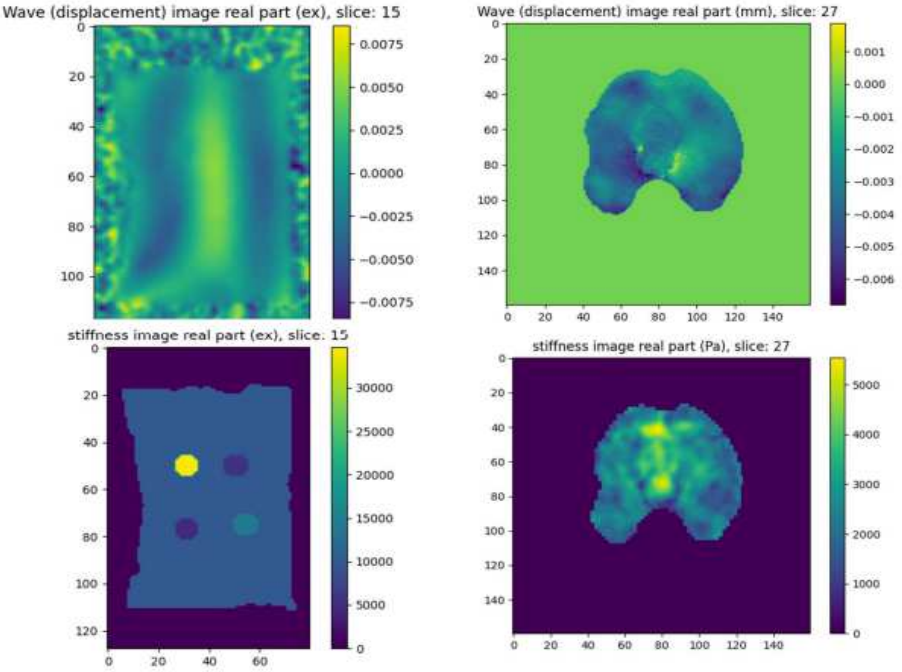

Figure 37: Comparison of training (left) and testing data (right). Displacement data(above) in mm and storage modulus ground truth (below) in kPa.

variable	compo-nent	dtype	count	mean	std	min	max
wave	y	complex64	2048000	(-0.718-0.394j)	1,83	(-12.319+1.999j)	(5.754-2.243j)
	x	complex64	2048000	(-1.312-2.749j)	6,58	(-16.209-12.848j)	(0.875-11.872j)
	z	complex64	2048000	(0.002+0.597j)	1,72	(-8.170-3.405j)	(10.725+0.515j)
mre	scalar	complex128	2048000	(405.219+188.399j)	1065,08	0j	(6670.603+1283.487j)
mre_mask	scalar	uint8	2048000	(16.789+0j)	44,71	0j	(207+0j)
anat	scalar	float64	2048000	(277.226+0j)	457,37	(-139.547+0j)	(4107.976+0j)
bin_mask	scalar	uint8	2048000	(0.172+0j)	0,38	0j	(1+0j)

Table 8: Table of first-order statistics of MRE data.

In all data-driven approaches it's important to get to know the data one is dealing with to identify bad samples in the dataset or track down outliers. In Table 8, first-order statical indices are presented for each variable:

- *wave*: complex displacement wave field. Each component indicated the direction of encoded displacement (three volumes 3D)

- *mre*: complex ground truth stiffness field (3D)
- *mre mask*: anatomical segmentation mask (3D)
- *anat*: T1w anatomical image (3D)
- *bin mask*: binary mask used during training to choose adequate training points not in the background (3D).

6.2 Testing Study: Methods

The same PINN structure and assumptions presented in the reference work will be adopted for this testing study. Training will be stopped manually when the total loss and each single loss term do not improve and are stable with little oscillation.
Both Helmholtz and heterogeneous equations will be used in the model PDE term (see Table 1). Results of this step will be compared with algorithms of FEM and direct methods, presented in sections 5.1.2 and 5.1.3 and implemented in the reference study. The same set of evaluation metrics presented for the previous step will be adopted. First-PDE strategy will be used (section 5.2.2) for all the PINN configurations investigated in this testing study. In addition, PINN structure will be adapted to include a further optional loss $\mathcal{L}_{\text{stiff}}$ designed to fit pre computed stiffness.
Conventional MRI anatomical images are also available for the testing dataset and this will allow to introduce them in the model in the testing study (section *Anatomical Imaging*) and assess the effect of including anatomical information through T1w MRI images. Moreover, two optimization algorithms different from original work Adam will be used in order to balance the different loss terms (section *Optimization algorithms*).

This work is a preliminary study to assess PINN feasibility to invert MRE data from brain tissues. An important simplification will be done when assuming incompressibility and linear isotropic relation to model brain biomechanics, which is also adopted in many related works [113] [63] [114], despite its limitations. Brain mechanical response is indeed exceptionally complex, characterized by nonlinearity, compression-tension asymmetry, conditioning effects and the measured modulus might depends on the loading mode, strain regime and rate, and length scale [61].

6.2.1 Optimization algorithms

The reference study adopts Adam optimization to train the model. But PINN is a multiobjective optimization problem with multiple loss terms that pose additional challenges to NN convergence due to unbalanced back propagated gradients during network training: in terms of computational cost, as observed also in the training study, PINN still cannot outperform DI and FEM methods. Using the same weight for each term leads to disparate rate of convergence among them [81], while more refined weighting approach could enhance the overall convergence.
In [96] it is shown that adopting a multi-task learning approach, which weights differently the loss objectives , improves significantly PINN performances with accelerated convergence by

introducing only a small number of additional learnable parameters, consistent with the number of loss terms. The same strategy will be applied in this work by developing and testing two existing successful weight-adaptive algorithms: Multiadam [13] and Learning Rate annealing to mitigate gradients pathologies [14].

1) Multiadam

The recent work implemented in [13] addresses the challenges of training PINNs when dealing with imbalanced loss terms. PDE and data loss functions might differ by several orders of magntitude and discrepancy is observed between the PINN's loss fucntion and actual performance: these issues arise from the inherent differences in scales between PDEs and boundary conditions. After a theoritical analysis on the effect of domain scaling on loss balancing, the authors propose a new scale-invariant optimizer, MultiAdam.

This optimizer leverages the observation that the second momentum of Adam is an excellent indicator of gradient scale, and adjusts the scale of gradients by maintaining separate second momentum terms for different scales of losses. This adjustment balances better the training process across different loss scales. Pseudocode for this algorithm is shown in Figure 38: PINN losses are divided into several groups partitioning the PDE loss into a separate group; the first and the second momentum are computed independently for each group ($m_{t,i}$ and $v_{t,i}$ in Figure 38) and updates are averaged separately for each group ($\hat{m}_{t,i}$ and $\hat{v}_{t,i}$ in Figure 38).

Algorithm 2 MultiAdam

Require: learning rate γ, betas β_1, β_2, max epoch M, objective functions $f_1(\theta), f_2(\theta), \cdots, f_n(\theta)$

for all $t = 1$ to M **do**
  for all $i = 1$ to n **do**
    $g_{t,i} \leftarrow \nabla_\theta f_i(\theta_{t-1})$
    $m_{t,i} \leftarrow \beta_1 m_{t-1,i} + (1-\beta_1) g_{t,i}$
    $v_{t,i} \leftarrow \beta_2 v_{t-1,i} + (1-\beta_2) g_{t,i}^2$
    $\hat{m}_{t,i} \leftarrow m_{t,i}/(1-\beta_1^t)$
    $\hat{v}_{t,i} \leftarrow v_{t,i}/(1-\beta_2^t)$
  end for
  $\theta_t \leftarrow \theta_{t-1} - \frac{\gamma}{n} \sum_{i=1}^{n} \hat{m}_{t,i}/(\sqrt{\hat{v}_{t,i}} + \varepsilon)$
end for
return θ_t

Figure 38: Pseudocode for Multiadam optimization. Adapted from "Multiadam: Parameter-wise scale-invariant optimizer for multiscale training of physics-informed neural networks" Jiachen et al., International Conference on Machine Learning, PMLR, 2023.

Extensive experiments across various PDE problems demonstrate that MultiAdam significantly

improves the predictive accuracy of PINNs, outperforming traditional optimizers by 1-2 orders of magnitude, exhibits remarkable stability and high convergence rates.

The code where this optimizer is constructed is released and available on Github [10]. In this work, an instance of the MultiAdam optimizer with the parameters of the PINN model is created and the only optimizer-specific options specified is a list of loss group indices indicating how to group them.

2) Learning rate annealing to mitigate gradients pathologies

The study [14] identified and analyzed a fundamental mode of failure in the effectiveness of PINN in discovering hidden patterns from noisy data. They related this problem to numerical stiffness leading to unstable magnitude of back-propagated gradients during model training when using gradient descent. They presented a learning rate annealing algorithm that utilizes gradient statistics during model training to balance the interplay between different terms in composite loss functions and trades off data fitting and equations satisfaction. The basic idea behind Adam to keep track of the first- and second-order moments of the back-propagated gradients is reproposed in a similar spirit and can be read in Figure 39 (Pseudocode) : an adaptive rule is derived for automatically λ_i weights online during training by utilizing mean and maximum values of loss gradients.

[10] `https://github.com/i207M/MultiAdam`

Algorithm 1: Learning rate annealing for physics-informed neural networks

Consider a physics-informed neural network $f_\theta(\boldsymbol{x})$ with parameters θ and a loss function

$$\mathcal{L}(\theta) := \mathcal{L}_r(\theta) + \sum_{i=1}^{M} \lambda_i \mathcal{L}_i(\theta),$$

where $\mathcal{L}_r(\theta)$ denotes the PDE residual loss, the $\mathcal{L}_i(\theta)$ correspond to data-fit terms (e.g., measurements, initial or boundary conditions, etc.), and $\lambda_i = 1$, $i = 1, \ldots, M$ are free parameters used to balance the interplay between the different loss terms. Then use S steps of a gradient descent algorithm to update the parameters θ as:

for $n = 1, \ldots, S$ **do**

(a) Compute $\hat{\lambda}_i$ by

$$\hat{\lambda}_i = \frac{\max_\theta\{|\nabla_\theta \mathcal{L}_r(\theta_n)|\}}{\overline{|\nabla_\theta \mathcal{L}_i(\theta_n)|}}, \quad i = 1, \ldots, M,$$

where $\overline{|\nabla_\theta \mathcal{L}_i(\theta_n)|}$ denotes the mean of $|\nabla_\theta \mathcal{L}_i(\theta_n)|$ with respect to parameters θ.

(b) Update the weights λ_i using a moving average of the form

$$\lambda_i = (1 - \alpha)\lambda_i + \alpha \hat{\lambda}_i, \quad i = 1, \ldots, M.$$

(c) Update the parameters θ via gradient descent

$$\theta_{n+1} = \theta_n - \eta \nabla_\theta \mathcal{L}_r(\theta_n) - \eta \sum_{i=1}^{M} \lambda_i \nabla_\theta \mathcal{L}_i(\theta_n)$$

end

The recommended hyper-parameter values are: $\eta = 10^{-3}$ and $\alpha = 0.9$.

Figure 39: Pseudocode for Learning Rate annealing algorithm. Adapted from Wang, Sifan, Yujun Teng, and Paris Perdikaris. "Understanding and mitigating gradient pathologies in physics-informed neural networks." arXiv preprint arXiv:2001.04536 (2020).

The proposed method was tested on various benchmark problems in computational physics, showing a substantial improvement in predictive accuracy (by a factor of 50-100x) over conventional PINNs and suggesting that addressing gradient pathologies is crucial for improving the reliability and accuracy of these models.

6.2.2 Anatomical Imaging

In Ragoza's study [10], liver anatomical information is incorporated in the PINN prediction model of hepatic complex shear modulus. Prior work had demonstrated a great potential of tissue elasticity prediction from anatomical MRI. In [91], a DL algorithm was developed to generate entire 3D-reconstructed images of hepatic stiffness using only MRI derived inputs when MRE hardware and software is not available, in patients with NAFLD. Nine conventional MRI sequences, clinical and demographic data were used to train a CNN to reconstruct stiffness images at voxel-level and, after testing various configurations, the model that achieved the best predictive performance was the one informed solely by four standard MRI image sequences and clinical features, yielding a voxel-level correlation of 0.34 ± 0.03. The structure of the model taking in input MRI data and predicting stiffness values showed relevant differences with Ragoza's implemented PINN: first, a convolutional neural network was implemented instead of a feedforward one; secondly, the combination of more MRI sequences was used as it outperformed individual ones providing a more complete set of necessary information. In the end, the model integrated also radiomic, US, and clinical data to improve its capability. Despite this was just a preliminary study presenting the aforementioned limitations, the proposed CNN model showed feasibility of generation of DL-automated virtual elastographic images from MRI sequences.

Another similar research work [115] implemented a Support Vector Machine (SVM) machine learning model that incorporates clinical and nonelastographic MRI T2-weighted radiomic features, for categorization of liver disease through liver stiffness cutoff values. The model was trained on pediatric and young adult patients and was successful (accuracy 75 %, AUC 0.80), but needs further investigations and more robust external validation. These preliminary studies support Ragoza's study discoveries, where the introduction of MRI anatomical features into the PINN model improves its performances.

Same considerations were applied to MRI-derived bone porosity index (PI) [116], a non invasive biomarker that is used to assess disease variations of bone porosity and relative treatment responses. In fact, data analysis from this study showed porosity index alone accounts for 63 % of stiffness variability, making it a moderate predictor of bone stiffness. PI derived from skull tissue MR imaging could then provide relevant information for characterizing its stiffness.
A recent work developed a feedforward DL model to estimate myocardial stiffness properties from hemodynamic measures and heart geometric and fiber-orientation features derived from routinetly avaliable MR cardiac imaging [115]. The model showed excellent performances and encouraged the idea of using neural networks to output stiffness values from MRI-derived fea-

tures.

Similar findings emerged in brain studies. A group in [117] investigated pairing of high-resolution maps of both cerebrospinal fluid (CBF) measured in vivo in MRI acquisitions and MRE viscoelasticity measures, which likely integrate both solid and vascular properties because they reflect medium properties. A linear regression analysis found a strong correlation between CBF measured by MRI perfusion and viscoelastic brain constants ($|G^*|$) in deep GM tissues.
Another group tried to understand the complex link between changes in microstructural components and the corresponding mechanical response of human brain tissue combining in a DL model results from tension, compression experiments and enzyme assays[61]. They found a high relevance of extracellular matrix protein fibronectin for elastic behaviour in almost all brain regions; cellular components resulted to be the most relevant components for viscoelastic response, remarking the idea that tissues anatomical microconstituents are relevant for characterizing tissues mechanics.

A recently published study has thoroughly examined the effectiveness of conventional MRI in pre-operatively in predicting the consistency of meningiomas (also referred to as firmness or texture of a tumor) reviewing all the related works. Despite it is still not a validated method by multicenter imaging studies, there have been multiple articles showing the promise of T2w MRI images to predict consistency, valuable biomarker for neurosurgical planning.

All these results provide an exhaustive rationale for including anatomical information in the PINN model of the current work.

This will be incorporated adding as model inputs T1w anatomical MR images (see Figure 17), which are standard to collect in clinical practice when MR elastography is performed. Delaware dataset provides T1w anatomical data, registered rigidly and downsampled to the MRE space. These images allow for a one-to-one correspondence between the voxels in the MRE data and the anatomical segmentations. The rigid transformation from the fixed image to the moving image is provided in a Matlab file, which is generated from Advanced Normalization Tools (ANTs). The T1w images are then transformed using 5th order B-spline interpolation. For a detailed description of MR images processing, please consult Delaware Datasets documentation [11].
This term will be included also with an additional output head $\hat{\mathbf{a}}(\mathbf{x}, \theta^{\mu})$ on the second NN and another optional loss function $\mathcal{L}_{\text{anat}}$ that takes into account anatomical features and forces the model to fit and gain information from anatomical data, exactly as in [10]. This term is multiplied

[11] `https://www.nitrc.org/frs/?group_id=1390`.

by its relative anatomical weight λ_{anat} and its inclusion in the model is set simply by adjusting the anatomical weight to be different from zero. .

This work will compare both heterogeneous and Helmholtz PDE models, with and without the anatomical loss term, to determine whether the T1-w MRI anatomical image enhances stiffness prediction also in the brain, as expected.

6.2.3 PINN on Delaware dataset

Without Direct Inversion as prior stiffness				
Magnitude(Pa)	DIRECT	FEM	PINN (het)	PINN (homo)
MAV	1117,870	561,190	277,000	277,350
RMSE	3208,700	1587,390	727,650	730,110
MAXE	45634,130	31267,320	5254,870	5659,850
SSIM	0,800	0,830	0,840	0,840
PSNR	7,590	18,370	19,860	20,140
R^2	0,580	0,660	0,870	0,830
Real(Pa)				
MAV	571,700	418,050	191,940	183,120
RMSE	1837,470	1271,090	554,170	543,650
MAXE	34585,710	31144,280	5119,910	5358,000
Imaginary(Pa)				
MAV	871,210	297,520	175,710	180,470
RMSE	2630,480	950,860	471,560	487,350
MAXE	41336,550	18659,110	2877,410	3294,920
Angle(rad)				
MAV	0,048π	0,076π	0,022π	0,022π
RMSE	0,137π	0,226π	0,057π	0,064π
MAXE	0,959π	1,363π	0,761π	1,191π

Table 9: Evaluation metrics for Direct, FEM, PINN with heterogeneous and homogeneous PDE, including the anatomical loss

Table 9 shows evaluation metrics of with included anatomical loss. PINN (het) shows a slightly improved correlation of $R^2 = 0.87$ versus $R^2 = 0.83$ for compared to PINN (homo) but for all the other metrics there is no enhancement of stiffness prediction when changing PDE associated with the model.

Computational time required	Direct	FEM	PINN
(s)	3.814	576.22	99.509.219
(h)	0.001	0.16	27.641

Table 10: Computational time required for the inversion methods.

Table 10 shows evaluation computational times required for computing direct inversion, for extraction of FEM stiffness and for training the network. As expected and as in the phantom, PINN training is the most time-consuming operation.

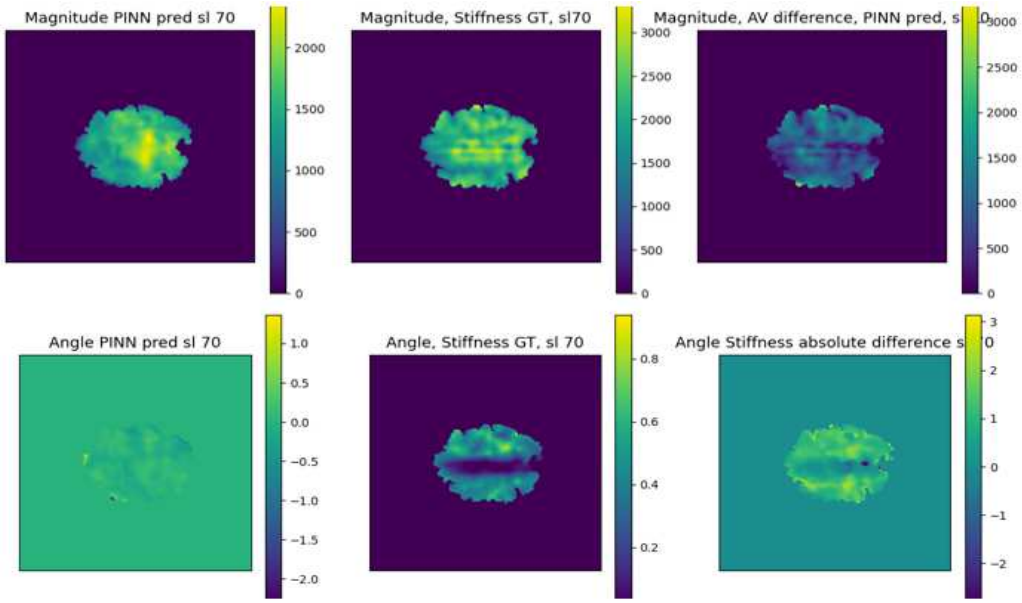

Figure 40: Magnitude and angle of G^* estimates from PINN heterogeneous inversion: prediction (left), ground truth (middle) and residuals(right).

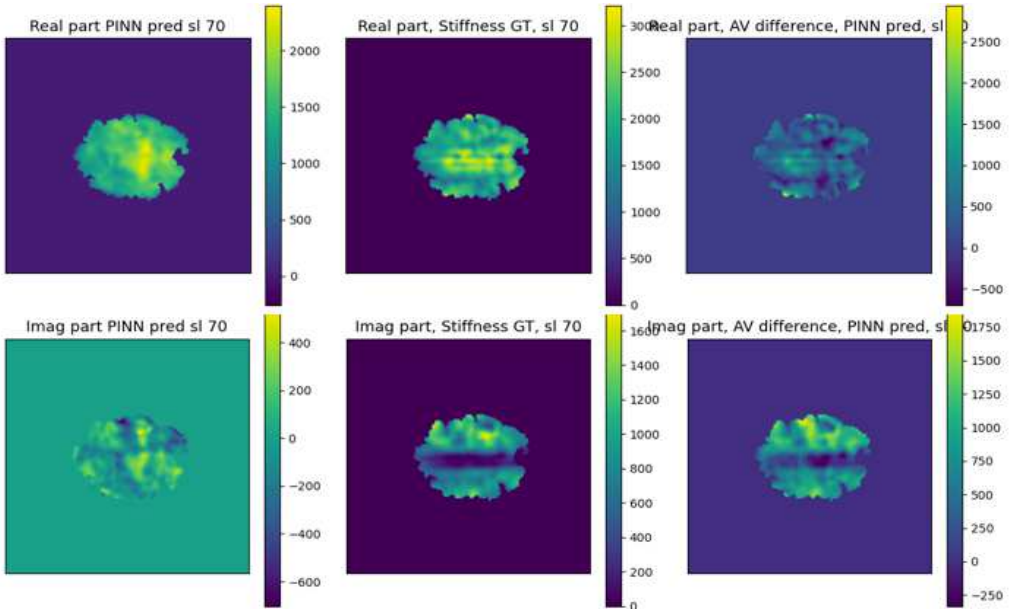

Figure 41: Real and imaginary part of G^* estimates from PINN heterogeneous inversion: prediction (left), ground truth (middle) and residuals(right).

Figures 40 and 41 illustrate the performance of this inversion method in predicting all components of the complex shear modulus for one brain slice. Similarly to the phantom, only the real part and magnitude components show reasonable stiffness estimates.

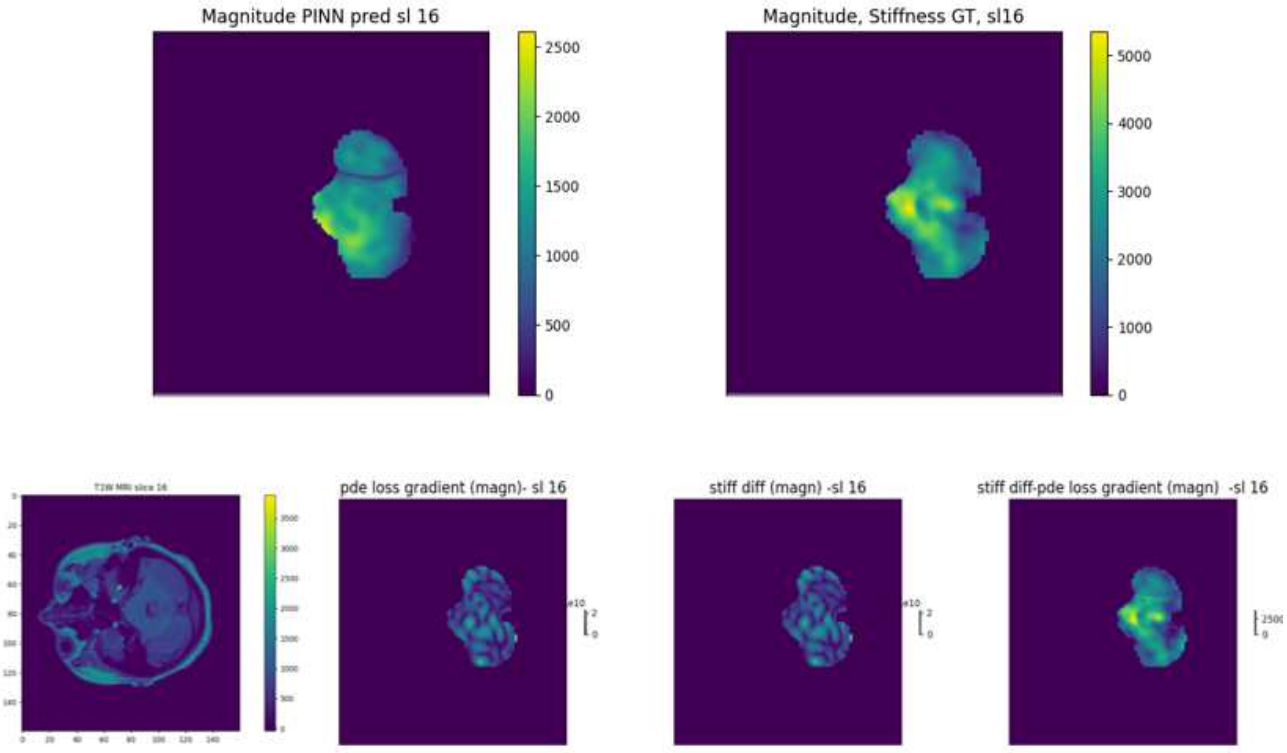

Figure 42: Stiffness heterogeneous PINN $|G^*|$ prediction and ground truth (above) for slice 16 (out of 80) when including the anatomical term; correspondent anatomical slice (left below). Gradient of PDE loss and relative diffences (right below).

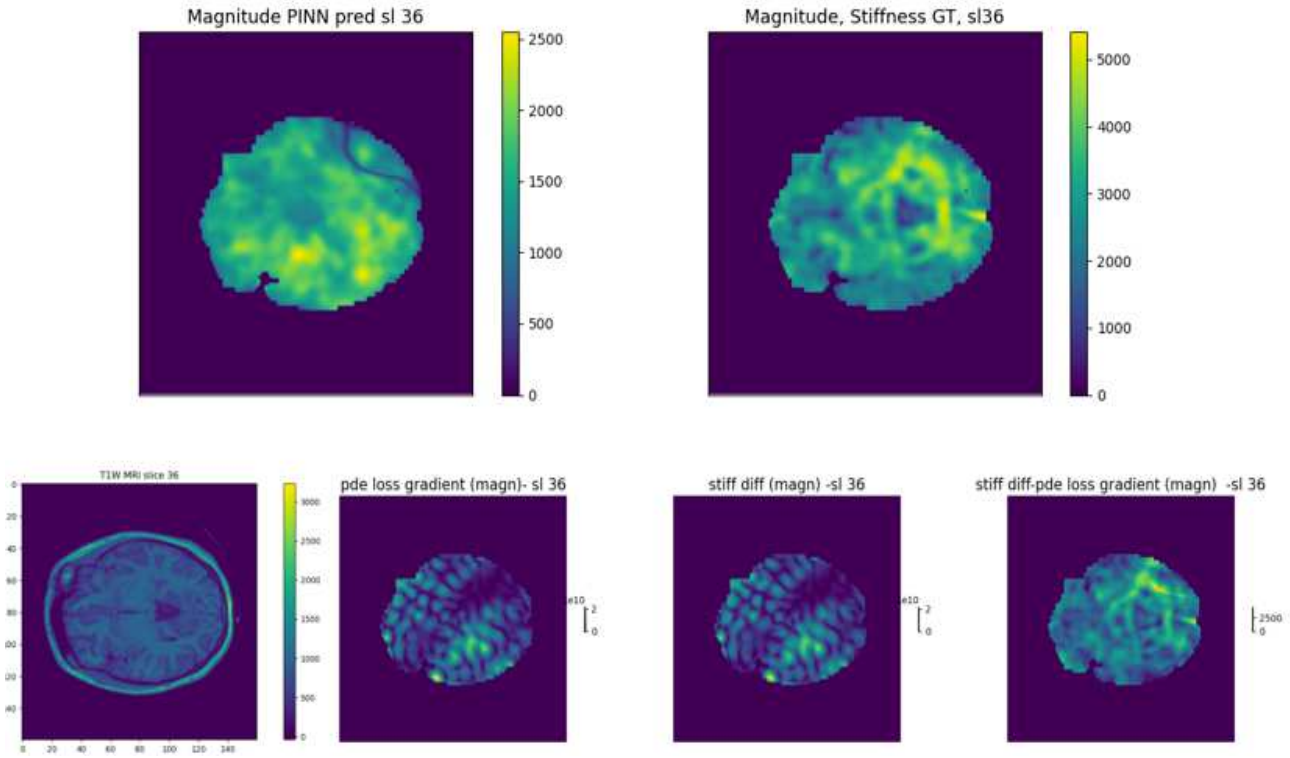

Figure 43: Stiffness heterogeneous PINN |*G**| prediction and ground truth (above) for slice 36 (out of 80) when including the anatomical term; correspondent anatomical slice (left below). Gradient of PDE loss and relative diffences (right below).

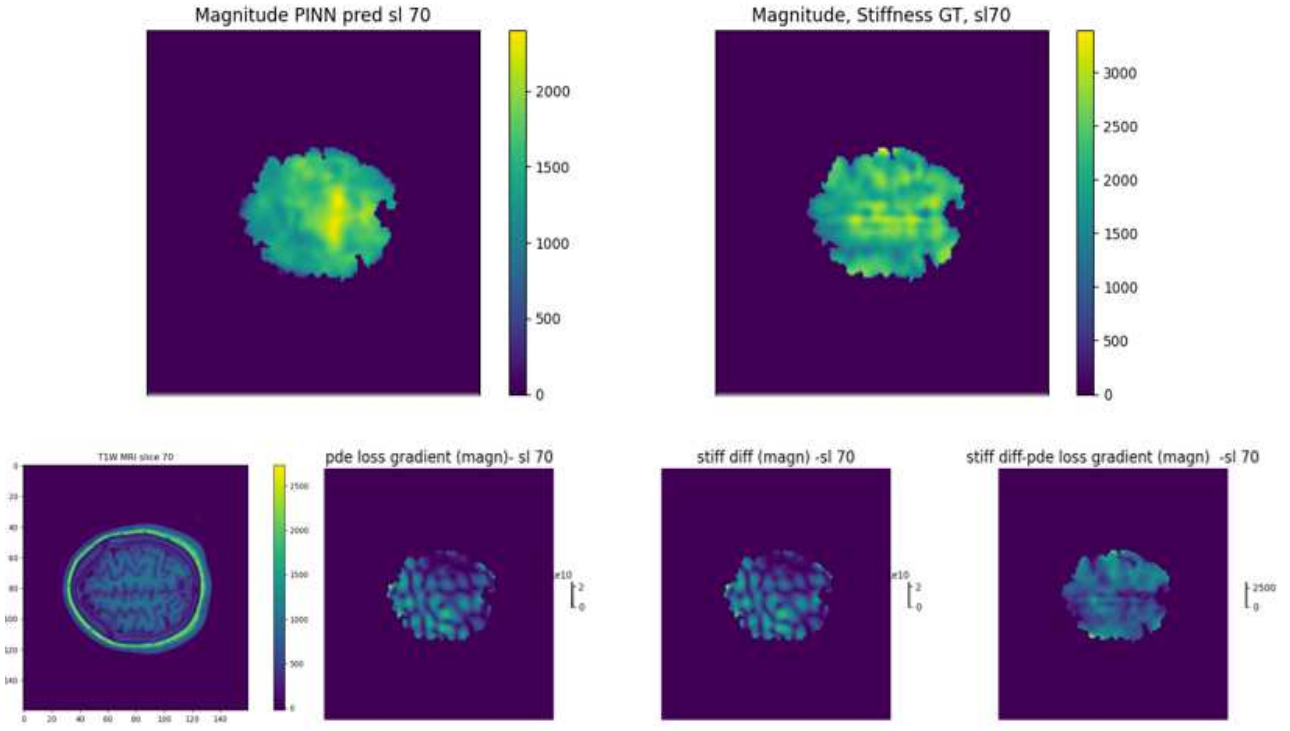

Figure 44: Stiffness heterogeneous PINN |*G**| prediction and ground truth (above) for slice 70 (out of 80) when including the anatomical term; correspondent anatomical slice (left below). Gradient of PDE loss and relative diffences (right below).

Figures 42,43,44 show PINN |G^*| prediction and Ground truth (above), the referred anatomical slice (below, left) and three pictures representing PDE loss gradient, stiffness difference and relative difference between these two terms (below, right). to assess the agreement between the PDE solution and the actual data. Each figure refers to one slice. For each of them, gradient of the PDE loss indicates that the PINN was not able not find a stiffness solution that satisfies the PDE constraints across the entire domain.

6.2.4 Anatomical Imaging

Without Direct Inversion as prior stiffness		
Magnitude(Pa)	**PINN (het)**	**PINN (homo)**
MAV	390.64	270.94
RMSE	1213.17	713.62
MAXE	13107.18	5428.83
SSIM	0.83	0.84
PSNR	15.43	20.50
R^2	0.62	0.82
Real(Pa)		
MAV	316.62	173.75
RMSE	1118.06	522.62
MAXE	13099.57	5131.25
Imaginary(Pa)		
MAV	171.48	179.87
RMSE	470.87	485.93
MAXE	3428.56	3053.14
Angle(rad)		
MAV	0,022π	0,022π
RMSE	0,073π	0,064π
MAXE	1,334π	1,236π

Table 11: PINN evaluation metrics with heterogeneous and homogeneous PDE, excluding the anatomical loss

Table 11 shows performance metrics of PINN with heterogeneous and homogeneous PDE, without anatomical term (Table 9). Without this information, PINN (het) is even less accurate than PINN (homo).

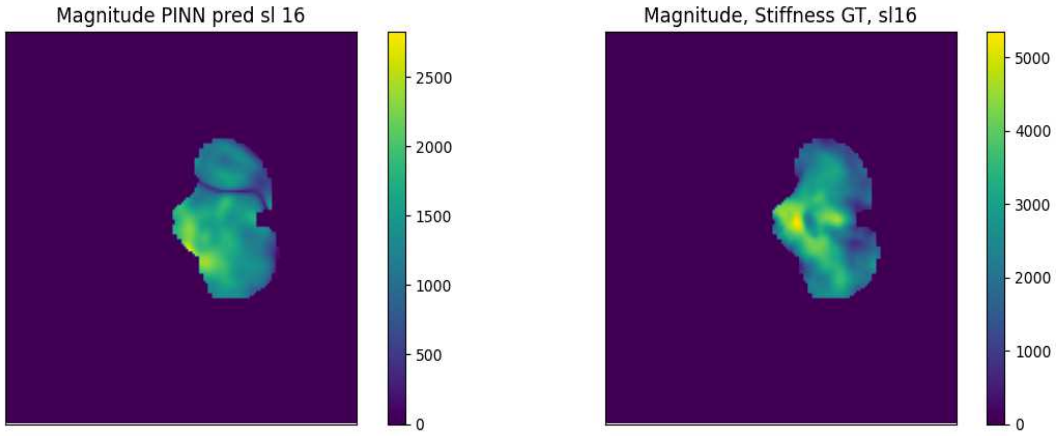

Figure 45: Stiffness PINN $|G^*|$ prediction and ground truth for slice 16 (out of 80) without including the anatomical term.

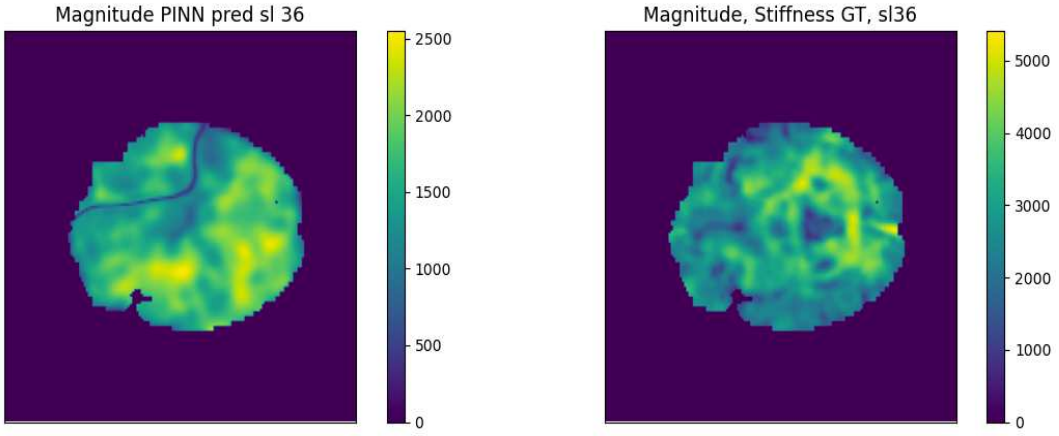

Figure 46: Stiffness PINN $|G^*|$ prediction and ground truth for slice 36 (out of 80) without including the anatomical term.

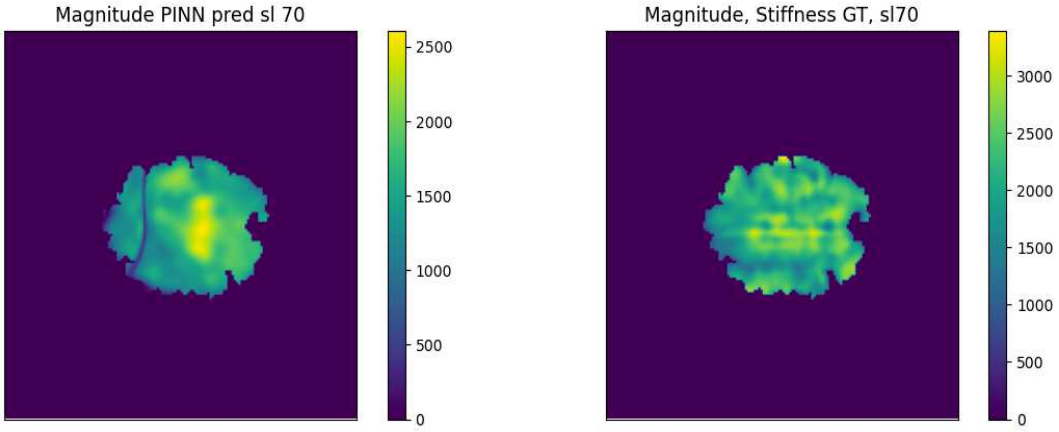

Figure 47: Stiffness PINN |G^*| prediction and ground truth for slice 70 (out of 80) without including the anatomical term.

Figures 45,46 and 47 display |G^*| predictions and reference standard for three brain slices when inversion is performed not including the anatomical loss.

6.2.5 Including prior Direct Inversions

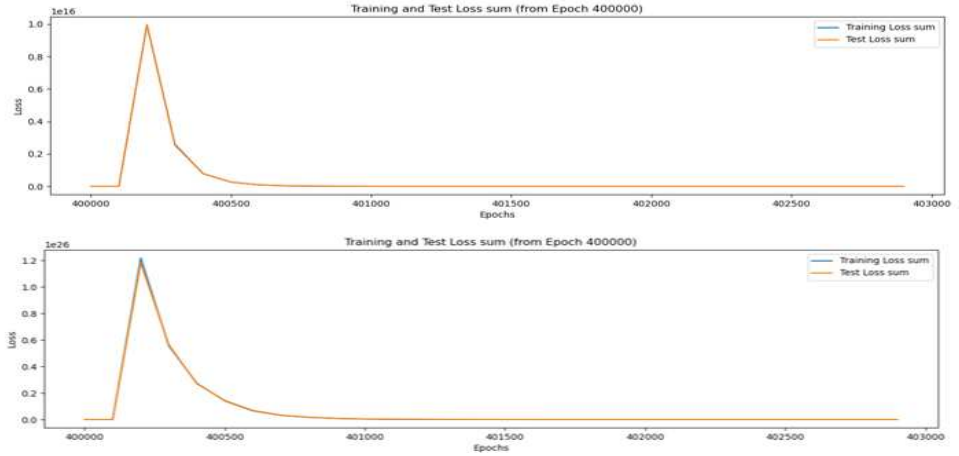

Figure 48: Loss decay (first epochs) when including (above) and not including (below) pre computed DI stiffness

With Direct Inversion as prior stiffness	
Magnitude(Pa)	**PINN (het)**
MAV	286,260
RMSE	738,050
MAXE	6792,960
SSIM	0,820
PSNR	20,400
R^2	0,840

Real(Pa)	
MAV	194,610
RMSE	558,240
MAXE	6670,600

Imaginary(Pa)	
MAV	183,610
RMSE	482,780
MAXE	2857,550

Angle(rad)	
MAV	0,025π
RMSE	0,067π
MAXE	1,287π

Table 12: PINN evaluation metrics when including prior DI stiffness to guide training

The benefit of including a precomputed stiffness was more evident for the MRE phantom: neither the loss accelerates convergence (Figure 48) nor performance metrics of Table 12 are better than the model without this term (Table 9).

6.2.6 Optimization algorithms

	Adam	Multiadam	LR annealing
Magnitude(Pa)			
MAV	300,66	276,64	299,84
RMSE	788,69	726,56	786,25
MAXE	5948,97	5215,69	5958,39
SSIM	0,83	0,84	0,83
PSNR	19,22	19,9	19,2
R^2	0,71	0,87	0,8
Real(Pa)			
MAV	221,23	190,59	220,61
RMSE	636,12	551,42	633,44
MAXE	5843,38	5083,71	5854,47
Imaginary(Pa)			
MAV	172,54	176,32	172,48
RMSE	466,23	473,11	465,78
MAXE	2771,78	2907,64	2756,96
Angle(rad)			
MAV	0,029π	0,022π	0,029π
RMSE	0,096π	0,057π	0,089π
MAXE	1,318π	0,92π	1,299π

Table 13: PINN evaluation metrics with different optimization algorithms

Computational time required			
total seconds	86.667	30.944	76.678.967
total hours	**24.074**	**8.596**	**21.300**
second/epoch	0.85	1.628	0.78

Table 14: Computational time required for PINN training with different optimization algorithms.

Table 13 shows that no optimization algorithm is able to enhance PINN performances. On the other side, PINN convergence shows acceleration when learning rate annealing optimization is adopted (Figure 49).

7 Discussion

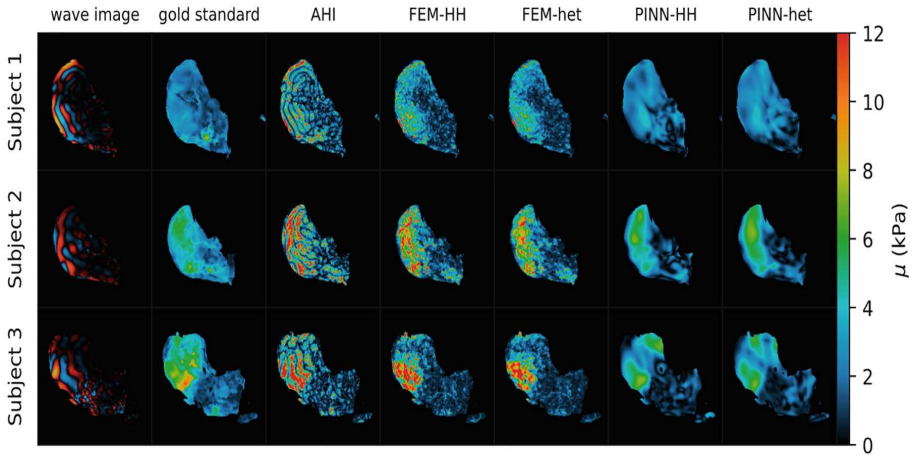

Figure 49: Elasticity reconstructions examples from liver images of three patients, from the reference study [10] from "Physics-Informed Neural Networks for Tissue Elasticity Reconstruction in Magnetic Resonance Elastography" from Ragoza et al, 2023 Springer eBook. @2023 Springer Nature. Used with permission.

Despite for both the studies PINN outperforms two state-of-the art inversion methods (Tables 5 and 9) for all the components of the complex shear modulus, results are different between the MRE phantom and the human dataset. For the phantom, magnitudes of stiffness estimates from PINN (het) and PINN (homo) (Figure 28 and 32) and corresponding histograms (Figures 27 and 31) visibly show that the first one better captures the complex structure of the phantom, providing more accurate and detailed stiffness estimates in both magnitude and angle, which is consistent because homogeneous PINN does not allow local variations of stiffness properties. This agrees with results from Ragoza's liver study (Figure 49) where PINN (het) has the highest correlations with gold standard elasticity, and with Murphy's ANN inversion [11]. For phantom and liver mediums, the homogeneity assumption degradates estimates, as expected. On the other side, for Delaware data, PINN (het) and PINN (homo) do not differ significantly in performance metrics evaluation. This might suggest that the fundamental equation used to derive both heterogeneous and homogeneous models is inconsistent with the actual laws governing wave propagation in the brain. This discrepancy suggests that the theoretical framework could be misaligned with the brain's real wave propagation dynamics.

It is also important to consider the differing reliability of the reference standards used to compute metrics for the phantom and the brain. The phantom's reference standard benefits from the known true stiffness parameters, while the Delaware dataset relies on an NLI inversion method for multiresolution elastography [112], which has several limitations. For instance, estimates of the loss modulus are less accurate and challenging than the storage modulus, possibly because

the loss modulus does not reflect the tissue's physical properties as accurately. Another limitation is the traded-off resolution: while subsampling can stabilize estimates for challenging parameters like the loss modulus, it reduces resolution, potentially obscuring small-scale variations in mechanical properties. Additionally, in some cases, discretization errors can become significant, degrading the accuracy of the inversion.

However, this novel method shows great promise, because it significantly outperforms two notable state-of-the-art inversion algorithms in both studies, as shown for liver data (Figure 49). The main challenge remains the computational time for PINN training (Tables 6 and 10), but once the network is trained, predicting a new volume only requires a forward pass through the network (approximately 1 minute). Moreover, the proposed strategy of including a DI prior estimate in PINN inversion does not improve significantly performances but accelerates training remarkably in the phantom (Figure 48). Future research on this inversion method should focus on two goals; first, improving the speed and efficiency of the inversion process, secondly, increase the model generalization and reusability across different subjects and scanners, providing techniques of transfer learning and statistical equalization of input data such that the model does not have to be retrained but just predicted. Ideally, evaluation in an actual clinical setting could be performed in a standard desktop personal computer [91], without requiring the high processing units used for PINN training.

The magnitude and real part of the complex shear modulus G^* are clearly the best-performing components for both the phantom (Figures 27, 28, 29) and the brain (Figures 40, 41). The real part of G^*, representing elasticity, generally has a stronger effect on the behavior of the system than the imaginary part, representing viscosity: waves are more sensitive to changes in the real part of G^* than in the imaginary part, making it easier for the neural network to learn and estimate the real part. Moreover, the MSE stiffness loss $\mathcal{L}_\mu$ minimizes the magnitude of G^*, making the training parameters directed toward this objective. It is also important to note that the real component is more reliably estimated than the imaginary component because the real component is orders of magnitude higher than the imaginary component, making it more similar to the overall modulus.

For Delaware dataset, in a few slices the stiffness reconstruction presents some lines where the model does not provide an estimate (Figures 42,43,45,46,47). From the corresponding anatomical image, one can notice these blue lines often appear at the boundaries of different regions within the tissue. This could be due to the model struggling with smoothly transition between areas of different stiffness.

Comparing tables 9 and 10, the improvement seen when incorporating anatomical information is only apparent when the model assumes heterogeneous stiffness. This suggests that the model is flexible enough to represent local discontinuities of tissue properties and anatomical features correspond to real variations in tissue stiffness. Furthermore, it is essential to explore how to transfer effectively a PINN model trained on one subject to other subjects and datasets, in order to leverage this high-performing technique. Visually observing in the images, the anatomically-informed slices (Figures 42,43,44) present less lines where the model does not provides estimate and show more distinct internal structures and boundaries, compared to the slices with no anatomical features (Figures 45,46,47).

The image of PDE loss gradient (pde grad, left) for the phantom is nearly uniform, suggesting that the PINN has learned to satisfy the governing equations well across the domain (Figure 30). Stiffness difference (mu diff, middle) variations indicate areas where the prediction deviates from the ground truth, with some localized regions of higher difference. The third image (pde grad-mu diff, right) is very similar to the stiffness difference, indicating that the errors in stiffness prediction are not correlated with the PDE loss gradient. For the three slices of brain results with the anatomical term (Figures 42,43,44), PDE loss gradients show high values and vary a lot across one slice, indicating that the PINN is struggling to satisfy the governing equations uniformly across the complex biological tissue. Stiffness difference images show larger and more widespread differences between predicted and true stiffness and a stronger correlation between areas where the PDE is not well-satisfied and areas of stiffness prediction errors. This means that improving the PINN's ability to satisfy the governing equations could lead to better stiffness predictions and enforces the previous hypothesis that that brain data are not described by these physics equation, which characterize more appropriately phantom physics laws. Complex brain distribution of heterogeneity cannot be expected to behave like a phantom and more complex training data or more elaborated phantoms should be necessary before applying to human data the PINN model.

Finding a suitable modulus distribution that generates the observed deformation relies on capturing the hidden mapping between the two fields and DL has unique potential in handling inverse problem of elasticity in a data-driven way [89]. But with these physics *soft constraints*, there is no guarantees that the non-linear optimization will make the additional loss term R actually reach zero during training, with convergence to reliable solutions. The benefits of this method depends in fact on the physical information available from differential equations, and an important simplification was done in this work when assuming incompressibility and linear

isotropic relation to model wave propagation in brain tissues. A theoretical extension to cases of anisotropic or tranversely isotropic solids incompressible materials might be a more suitable way of modeling wave propagation in brain tissues; but in the brain nerve fibers follow curved paths and additional information about fiber directions [33] should be necessary to apply the method to the displacement field. A reasonable possibility that could help the training of anisotropic models is to use features extracted from Diffusion Tensor Imaging (DTI), as tissue stiffness was shown to correlate negatively with the fractional anisotropy (FA) parameter. In [90], a poroelastic mechanical model is adopted instead of a viscoelastic one to simulate MRE data, i.e. a model describing a behaviour of a biphasic media composed of both a fluid and a solid phase that interact, which might be more suitable to characterize brain tissues. Nevertheless, in [118] it is stated that viscoelastic inversions, simpler with fewer unknown properties, are sufficient to capture mechanical behaviour of brain tissues. Additionally, performance assessment of different inversion methods should be made more robust and clinically relevant, for example by comparing biological effects detected by stiffness maps, instead of stiffness images similarity or correlation. For example, one can test PINN ability to classify fibrosis stage for liver data, or differentiate cerebral tumors, or detecting age effects.

As explained in [81], the use of the standard multi-layer neural network architecture could also be the reason for the observed lack of accuracy in capturing the hidden mapping. Different architectures and hyperparameters can yield vastly different solutions [12], which may result in insufficient accuracy even with optimal configurations and long training times and this is still an open field of research. An hyperparameter search methodology in [12] revealed that PINNs are much sensitive to network architecture, i.e. the depth of hidden layers and number of parameters, but generally a shallow network with ~5 layers and ~neurons per layer is chosen to obtain fast backpropagation [12] and good accuracy [92]. Sampling techniques of collocation points and suitable activation functions can also impact on training: in [92], it is suggested ReLu is an optimal choice for solving elasticity problems and advancing sampling procedure may vary drastically PINNs performances. Finally, convolutional architectures might be more suitable to invert MRE data thanks to their ability of learning efficiently large and small-scale images features. This choice is adopted in [90], where a CNN model with a encoder-decoder architecture generates elastograms from displacement data comparable with those from NLI methods, and in [91], where generation of elastographic images through the CNN DeepLabv3+ improves expert-assessment of hepatic stiffness.

Along with MRI features, clinical information contains predictive power that is not contained in

an anatomical image alone and further improves evaluation metrics of stiffness predictions [91]. An additional input-output head and clinical loss term could force the PINN model to learn and incorporate also this knowledge.

The unbalanced back-propagated gradients during network training pose a big challenge to PINN convergence [96]. In some studies, the choice of advanced optimization algorithms improves the performance of multiobjective PINNs [96] [13] [14]. In this work, the attempts to optimize the training steps do not enhance significantly final performance metrics (Table 13), but accelerates PINN convergence (Table 14), showing higher efficiency because these optimization choices provide the same performances with faster convergence by introducing only a small number of additional learnable parameters. In particular, Multiadam greatly outperforms two other optimization techniques in computational time required to reach a stable performance, taking only 8 hours to reach good estimates. Despite a lack of accuracy, it's promising that good stability was observed on the numerical values of inferred parameters with different configurations.
The difficulty of reducing the PINN loss to a sufficiently low value, even with optimal algorithms, underscores the PINN difficulty to satisfy simultaneously both the displacement data fit and the physics constraints..

Despite the limitations of this work, the PINN method still is a favorable option compared to traditional methods and the strategies of incorporating in it a prior DI estimate to improve computational time, or to choose proper weight-adaptive algorithms, is promising to address the growing demand for real-time solutions to inverse elasticity problems and their numerous clinical applications. As concluded in [92] which similarly tests the same technique in solid mechanics problems, future research should prioritize quantifying the computational gains of the PINNs approach compared to conventional numerical methods. This analysis will be crucial for fully understanding the efficiency and potential advantages of PINNs, guiding their application in MRE elastography problems.

8 Conclusion

In this work, a PINN method is employed to invert MRE brain data with the objective of obtaining in fast times accurate and high resolution maps of viscoelastic properties, a diagnostic biomarker applicable to multiple clinical applications.
This inversion method and PINN structure have shown great potential in the liver data (previous study) [10] and in a MRE phantom (current study), but, even optimizing its configuration, it struggles more to accurately estimate brain parameters and there is inconsistency with previous studies as concerns the homogeneity stiffness assumption. The most plausible assumption is that a more suitable model to describe wave propagation in brain mechanics should be defined to match with displacement data provided by a MRE acquisition and more appropriate phantoms reflecting the complex nature of the brain should be used to pre-train these models. Another option is that the network architecture, parameters, and sampling techniques should be varied in order to suit this particular brain MRE inversion problem.

Despite this, results on MRE phantom and on in vivo brain data show that this method still outperforms remarkably traditional techniques like DI or FEM inversions, although training is extremely time-consuming. Moreover, the inclusion of brain anatomical information improves significantly the model containing a heterogeneous PDE that admits local stiffness gradients, which encourages including always anatomical images, when available in such models.
Research in this field should prioritize improving computational efficiency and addressing time-related challenges. Additionally, it is essential to explore how to effectively transfer a PINN model trained on one subject to other subjects and datasets in order to leverage this high-performing techniques.

References

[1] Daniel Fovargue, David Nordsletten, and Ralph Sinkus. “Stiffness reconstruction methods for MR elastography”. eng. In: *NMR in biomedicine* 31.10 (Oct. 2018), e3935. ISSN: 1099-1492. DOI: 10.1002/nbm.3935.

[2] Matthew C. Murphy et al. “Decreased brain stiffness in Alzheimer’s disease determined by magnetic resonance elastography”. eng. In: *Journal of magnetic resonance imaging: JMRI* 34.3 (Sept. 2011), pp. 494–498. ISSN: 1522-2586. DOI: 10.1002/jmri.22707.

[3] Axel Lipp et al. “Cerebral magnetic resonance elastography in supranuclear palsy and idiopathic Parkinson’s disease”. In: *NeuroImage : Clinical* 3 (Sept. 2013), pp. 381–387. ISSN: 2213-1582. DOI: 10.1016/j.nicl.2013.09.006. URL: https://www.ncbi.nlm.nih.gov/pmc/articles/PMC3814959/ (visited on 03/05/2024).

[4] Arvin Arani et al. “Harnessing brain waves: a review of brain magnetic resonance elastography for clinicians and scientists entering the field”. eng. In: *The British Journal of Radiology* 94.1119 (Mar. 2021), p. 20200265. ISSN: 1748-880X. DOI: 10.1259/bjr.20200265.

[5] T. E. Oliphant et al. “Complex-valued stiffness reconstruction for magnetic resonance elastography by algebraic inversion of the differential equation”. eng. In: *Magnetic Resonance in Medicine* 45.2 (Feb. 2001), pp. 299–310. ISSN: 0740-3194. DOI: 10.1002/1522-2594(200102)45:2<299::aid-mrm1039>3.0.co;2-o.

[6] S. Papazoglou et al. “Algebraic Helmholtz inversion in planar magnetic resonance elastography”. eng. In: *Physics in Medicine and Biology* 53.12 (June 2008), pp. 3147–3158. ISSN: 0031-9155. DOI: 10.1088/0031-9155/53/12/005.

[7] Matthew McGarry et al. “A heterogenous, time harmonic, nearly incompressible transverse isotropic finite element brain simulation platform for MR elastography”. eng. In: *Physics in Medicine and Biology* 66.5 (Feb. 2021). ISSN: 1361-6560. DOI: 10.1088/1361-6560/ab9a84.

[8] Matthew C. Murphy et al. “Artificial neural networks for stiffness estimation in magnetic resonance elastography”. eng. In: *Magnetic Resonance in Medicine* 80.1 (July 2018), pp. 351–360. ISSN: 1522-2594. DOI: 10.1002/mrm.27019.

[9] Sebastian Hirsch, Jurgen Braun, and Ingolf Sack. *Magnetic Resonance Elastography | Wiley Online Books*. © 2017 WILEY-VCH Verlag GmbH & Co. KGaA, Boschstr. 12, 69469 Weinheim, Germany, Nov. 2016. URL: https://onlinelibrary.wiley.com/doi/book/10.1002/9783527696017 (visited on 01/30/2024).

[10] Matthew Ragoza and Kayhan Batmanghelich. “Physics-Informed Neural Networks for Tissue Elasticity Reconstruction in Magnetic Resonance Elastography”. en. In: *Medical Image Computing and Computer Assisted Intervention – MICCAI 2023*. Ed. by Hayit Greenspan et al. Lecture Notes in Computer Science. Cham: Springer Nature Switzerland, 2023, pp. 333–343. ISBN: 978-3-031-43999-5. DOI: 10.1007/978-3-031-43999-5_32.

[11] Jonathan M. Scott et al. “Artificial neural networks for magnetic resonance elastography stiffness estimation in inhomogeneous materials”. In: *Medical Image Analysis* 63 (July 2020), p. 101710. ISSN: 1361-8415. DOI: 10.1016/j.media.2020.101710. URL: https://www.sciencedirect.com/science/article/pii/S136184152030075X (visited on 01/30/2024).

[12] Félix Fernández de la Mata et al. “Physics-informed neural networks for data-driven simulation: Advantages, limitations, and opportunities”. en. In: *Physica A: Statistical Mechanics and its Applications* 610.C (2023). Publisher: Elsevier. URL: https://ideas.repec.org//a/eee/phsmap/v610y2023ics0378437122009736.html (visited on 08/21/2024).

[13] Jiachen Yao et al. *MultiAdam: Parameter-wise Scale-invariant Optimizer for Multi-scale Training of Physics-informed Neural Networks*. arXiv:2306.02816 [cs, math]. June 2023. DOI: 10.48550/arXiv.2306.02816. URL: http://arxiv.org/abs/2306.02816 (visited on 07/26/2024).

[14] Sifan Wang, Yujun Teng, and Paris Perdikaris. *Understanding and mitigating gradient pathologies in physics-informed neural networks*. arXiv:2001.04536 [cs, math, stat]. Jan. 2020. DOI: 10.48550/arXiv.2001.04536. URL: http://arxiv.org/abs/2001.04536 (visited on 07/26/2024).

[15] Lucy V. Hiscox et al. “Magnetic resonance elastography (MRE) of the human brain: technique, findings and clinical applications”. eng. In: *Physics in Medicine and Biology* 61.24 (Dec. 2016), R401–R437. ISSN: 1361-6560. DOI: 10.1088/0031-9155/61/24/R401.

[16] *Vibration safety limits for magnetic resonance elastography - PMC*. URL: https://www.ncbi.nlm.nih.gov/pmc/articles/PMC2868320/ (visited on 03/02/2024).

[17] John Zhang et al. “Viscoelastic properties of human cerebellum using magnetic resonance elastography”. eng. In: *Journal of Biomechanics* 44.10 (July 2011), pp. 1909–1913. ISSN: 1873-2380. DOI: 10.1016/j.jbiomech.2011.04.034.

[18] Curtis L Johnson et al. “3D Multislab, Multishot Acquisition for Fast, Whole-Brain MR Elastography with High SNR Efficiency”. In: *Magnetic resonance in medicine : official journal of the Society of Magnetic Resonance in Medicine / Society of Magnetic Resonance in Medicine* 71.2 (Feb. 2014), pp. 477–485. ISSN: 0740-3194. DOI: 10.1002/mrm.25065. URL: https://www.ncbi.nlm.nih.gov/pmc/articles/PMC4061282/ (visited on 01/30/2024).

[19] Curtis L. Johnson et al. “Magnetic Resonance Elastography of the Brain using Multi-Shot Spiral Readouts with Self-Navigated Motion Correction”. In: *Magnetic resonance in medicine : official journal of the Society of Magnetic Resonance in Medicine / Society of Magnetic Resonance in Medicine* 70.2 (Aug. 2013), pp. 404–412. ISSN: 0740-3194. DOI: 10.1002/mrm.24473. URL: https://www.ncbi.nlm.nih.gov/pmc/articles/PMC3529970/ (visited on 03/07/2024).

[20] *Simultaneous multislice rapid magnetic resonance elastography of the liver - PubMed*. URL: https://pubmed.ncbi.nlm.nih.gov/31971301/ (visited on 03/07/2024).

[21] Wang Huifang et al. “A Three-dimensional quality-guided phase unwrapping for MR elastography”. In: *Physics in medicine and biology* 56 (July 2011), pp. 3935–52. DOI: 10.1088/0031-9155/56/13/012.

[22] Dennis C. Ghiglia and Mark D. Pritt. *Two-dimensional phase unwrapping: theory, algorithms, and software*. eng. OCLC: 37579779. New York: Wiley, 1998. ISBN: 978-0-471-24935-1. URL: http://catdir.loc.gov/catdir/toc/onix01/97038034.html (visited on 08/17/2024).

[23] Thomas J. Flynn. “Two-dimensional phase unwrapping with minimum weighted discontinuity”. EN. In: *JOSA A* 14.10 (Oct. 1997). Publisher: Optica Publishing Group, pp. 2692–2701. ISSN: 1520-8532. DOI: 10.1364/JOSAA.14.002692. URL: https://opg.optica.org/josaa/abstract.cfm?uri=josaa-14-10-2692 (visited on 08/17/2024).

[24] Ingolf Sack et al. “MR elastography of the human heart: noninvasive assessment of myocardial elasticity changes by shear wave amplitude variations”. eng. In: *Magnetic Resonance in Medicine* 61.3 (Mar. 2009), pp. 668–677. ISSN: 1522-2594. DOI: 10.1002/mrm.21878.

[25] Marvin A. Schofield and Yimei Zhu. “Fast phase unwrapping algorithm for interferometric applications”. EN. In: *Optics Letters* 28.14 (July 2003). Publisher: Optica Publishing Group, pp. 1194–1196. ISSN: 1539-4794. DOI: 10.1364/OL.28.001194.

URL: https://opg.optica.org/ol/abstract.cfm?uri=ol-28-14-1194 (visited on 08/17/2024).

[26] A. Manduca et al. “Magnetic resonance elastography: Non-invasive mapping of tissue elasticity”. In: *Medical Image Analysis* 5.4 (Dec. 2001), pp. 237–254. ISSN: 1361-8415. DOI: 10.1016/S1361-8415(00)00039-6. URL: https://www.sciencedirect.com/science/article/pii/S1361841500000396 (visited on 02/01/2024).

[27] Ralph Sinkus et al. “Elasticity reconstruction: Beyond the assumption of local homogeneity”. en. In: *Comptes Rendus. Mécanique* 338.7-8 (July 2010), pp. 474–479. ISSN: 1873-7234. DOI: 10.1016/j.crme.2010.07.014. URL: https://comptes-rendus.academie-sciences.fr/mecanique/articles/10.1016/j.crme.2010.07.014/ (visited on 08/01/2024).

[28] Eunyoung Park and Antoinette M. Maniatty. “Shear modulus reconstruction in dynamic elastography: time harmonic case”. eng. In: *Physics in Medicine and Biology* 51.15 (Aug. 2006), pp. 3697–3721. ISSN: 0031-9155. DOI: 10.1088/0031-9155/51/15/007.

[29] Jerrold Marsden and Anthony Tromba. *Vector_Calculus*. 6th. Macmillan learning, 2012. URL: https://www.cds.caltech.edu/~marsden/books/Vector_Calculus.html (visited on 08/18/2024).

[30] Ralph Sinkus et al. “Viscoelastic shear properties of in vivo breast lesions measured by MR elastography”. eng. In: *Magnetic Resonance Imaging* 23.2 (Feb. 2005), pp. 159–165. ISSN: 0730-725X. DOI: 10.1016/j.mri.2004.11.060.

[31] Daniel Fovargue et al. “Robust MR elastography stiffness quantification using a localized divergence free finite element reconstruction”. eng. In: *Medical Image Analysis* 44 (Feb. 2018), pp. 126–142. ISSN: 1361-8423. DOI: 10.1016/j.media.2017.12.005.

[32] A. J. Romano, J. J. Shirron, and J. A. Bucaro. “On the noninvasive determination of material parameters from a knowledge of elastic displacements theory and numerical simulation”. eng. In: *IEEE transactions on ultrasonics, ferroelectrics, and frequency control* 45.3 (1998), pp. 751–759. ISSN: 0885-3010. DOI: 10.1109/58.677725.

[33] Sebastian Hirsch et al. “MR elastography of the liver and the spleen using a piezoelectric driver, single-shot wave-field acquisition, and multifrequency dual parameter reconstruction”. eng. In: *Magnetic Resonance in Medicine* 71.1 (Jan. 2014), pp. 267–277. ISSN: 1522-2594. DOI: 10.1002/mrm.24674.

[34] Meng Yin et al. “Assessment of hepatic fibrosis with magnetic resonance elastography”. eng. In: *Clinical Gastroenterology and Hepatology: The Official Clinical Practice Jour-*

nal of the American Gastroenterological Association 5.10 (Oct. 2007), 1207–1213.e2. ISSN: 1542-7714. DOI: 10.1016/j.cgh.2007.06.012.

[35] Jurgen H. Runge et al. “Comparison of interobserver agreement of magnetic resonance elastography with histopathological staging of liver fibrosis”. eng. In: *Abdominal Imaging* 39.2 (Apr. 2014), pp. 283–290. ISSN: 1432-0509. DOI: 10.1007/s00261-013-0063-z.

[36] Laurent Huwart et al. “Liver fibrosis: non-invasive assessment with MR elastography”. eng. In: *NMR in biomedicine* 19.2 (Apr. 2006), pp. 173–179. ISSN: 0952-3480. DOI: 10.1002/nbm.1030.

[37] Laurent Huwart et al. “Liver Fibrosis: Noninvasive Assessment with MR Elastography versus Aspartate Aminotransferase–to-Platelet Ratio Index”. In: *Radiology* 245.2 (Nov. 2007). Publisher: Radiological Society of North America, pp. 458–466. ISSN: 0033-8419. DOI: 10.1148/radiol.2452061673. URL: https://pubs.rsna.org/doi/10.1148/radiol.2452061673 (visited on 08/01/2024).

[38] Laurent Huwart et al. “Magnetic Resonance Elastography for the Noninvasive Staging of Liver Fibrosis”. English. In: *Gastroenterology* 135.1 (July 2008). Publisher: Elsevier, pp. 32–40. ISSN: 0016-5085, 1528-0012. DOI: 10.1053/j.gastro.2008.03.076. URL: https://www.gastrojournal.org/article/S0016-5085(08)00572-6/fulltext (visited on 08/01/2024).

[39] Rolf Reiter et al. “Wideband MRE and static mechanical indentation of human liver specimen: sensitivity of viscoelastic constants to the alteration of tissue structure in hepatic fibrosis”. eng. In: *Journal of Biomechanics* 47.7 (May 2014), pp. 1665–1674. ISSN: 1873-2380. DOI: 10.1016/j.jbiomech.2014.02.034.

[40] Jing Guo et al. “In vivo abdominal magnetic resonance elastography for the assessment of portal hypertension before and after transjugular intrahepatic portosystemic shunt implantation”. eng. In: *Investigative Radiology* 50.5 (May 2015), pp. 347–351. ISSN: 1536-0210. DOI: 10.1097/RLI.0000000000000136.

[41] Jun Chen et al. “Early Detection of Nonalcoholic Steatohepatitis in Patients with Nonalcoholic Fatty Liver Disease by Using MR Elastography”. In: *Radiology* 259.3 (June 2011), pp. 749–756. ISSN: 0033-8419. DOI: 10.1148/radiol.11101942. URL: https://www.ncbi.nlm.nih.gov/pmc/articles/PMC3099044/ (visited on 08/01/2024).

[42] Sung Ui Shin et al. “Prediction of esophageal varices in patients with cirrhosis: usefulness of three-dimensional MR elastography with echo-planar imaging technique”.

eng. In: *Radiology* 272.1 (July 2014), pp. 143–153. ISSN: 1527-1315. DOI: 10.1148/radiol.14130916.

[43] Michael J. Korsmo et al. “Magnetic resonance elastography noninvasively detects in vivo renal medullary fibrosis secondary to swine renal artery stenosis”. eng. In: *Investigative Radiology* 48.2 (Feb. 2013), pp. 61–68. ISSN: 1536-0210. DOI: 10.1097/RLI.0b013e31827a4990.

[44] Nihar S. Shah et al. “Evaluation of renal parenchymal disease in a rat model with magnetic resonance elastography”. eng. In: *Magnetic Resonance in Medicine* 52.1 (July 2004), pp. 56–64. ISSN: 0740-3194. DOI: 10.1002/mrm.20101.

[45] Maja Cikes and Scott D. Solomon. “Beyond ejection fraction: an integrative approach for assessment of cardiac structure and function in heart failure”. eng. In: *European Heart Journal* 37.21 (June 2016), pp. 1642–1650. ISSN: 1522-9645. DOI: 10.1093/eurheartj/ehv510.

[46] Amil M. Shah et al. “Cardiac structure and function and prognosis in heart failure with preserved ejection fraction: findings from the echocardiographic study of the Treatment of Preserved Cardiac Function Heart Failure with an Aldosterone Antagonist (TOPCAT) Trial”. eng. In: *Circulation. Heart Failure* 7.5 (Sept. 2014), pp. 740–751. ISSN: 1941-3297. DOI: 10.1161/CIRCHEARTFAILURE.114.001583.

[47] Adomas Bunevicius et al. “REVIEW: MR elastography of brain tumors”. eng. In: *NeuroImage. Clinical* 25 (2020), p. 102109. ISSN: 2213-1582. DOI: 10.1016/j.nicl.2019.102109.

[48] S.K. Kyriacou et al. “Nonlinear elastic registration of brain images with tumor pathology using a biomechanical model [MRI]”. In: *IEEE Transactions on Medical Imaging* 18.7 (July 1999). Conference Name: IEEE Transactions on Medical Imaging, pp. 580–592. ISSN: 1558-254X. DOI: 10.1109/42.790458. URL: https://ieeexplore.ieee.org/abstract/document/790458 (visited on 08/19/2024).

[49] Joshua D. Hughes et al. “Higher-Resolution Magnetic Resonance Elastography in Meningiomas to Determine Intratumoral Consistency”. eng. In: *Neurosurgery* 77.4 (Oct. 2015), 653–658, discussion 658–659. ISSN: 1524-4040. DOI: 10.1227/NEU.0000000000000892.

[50] Joshua D. Hughes et al. “Magnetic resonance elastography detects tumoral consistency in pituitary macroadenomas”. eng. In: *Pituitary* 19.3 (June 2016), pp. 286–292. ISSN: 1573-7403. DOI: 10.1007/s11102-016-0706-5.

[51] N. Sakai et al. “Shear Stiffness of 4 Common Intracranial Tumors Measured Using MR Elastography: Comparison with Intraoperative Consistency Grading”. eng. In: *AJNR.*

American journal of neuroradiology 37.10 (Oct. 2016), pp. 1851–1859. ISSN: 1936-959X. DOI: 10.3174/ajnr.A4832.

[52] Matthew C. Murphy et al. “Preoperative assessment of meningioma stiffness using magnetic resonance elastography”. eng. In: *Journal of Neurosurgery* 118.3 (Mar. 2013), pp. 643–648. ISSN: 1933-0693. DOI: 10.3171/2012.9.JNS12519.

[53] M. Simon et al. “Non-invasive characterization of intracranial tumors by magnetic resonance elastography”. en. In: *New Journal of Physics* 15.8 (Aug. 2013). Publisher: IOP Publishing, p. 085024. ISSN: 1367-2630. DOI: 10.1088/1367-2630/15/8/085024. URL: https://dx.doi.org/10.1088/1367-2630/15/8/085024 (visited on 03/05/2024).

[54] M. Reiss-Zimmermann et al. “High Resolution Imaging of Viscoelastic Properties of Intracranial Tumours by Multi-Frequency Magnetic Resonance Elastography”. eng. In: *Clinical Neuroradiology* 25.4 (Dec. 2015), pp. 371–378. ISSN: 1869-1447. DOI: 10.1007/s00062-014-0311-9.

[55] Ziying Yin et al. “Slip interface imaging based on MR-elastography preoperatively predicts meningioma-brain adhesion”. eng. In: *Journal of magnetic resonance imaging: JMRI* 46.4 (Oct. 2017), pp. 1007–1016. ISSN: 1522-2586. DOI: 10.1002/jmri.25623.

[56] Ingolf Sack et al. “The impact of aging and gender on brain viscoelasticity”. eng. In: *NeuroImage* 46.3 (July 2009), pp. 652–657. ISSN: 1095-9572. DOI: 10.1016/j.neuroimage.2009.02.040.

[57] Prateek Kalra et al. “Magnetic resonance elastography of brain: Comparison between anisotropic and isotropic stiffness and its correlation to age”. eng. In: *Magnetic Resonance in Medicine* 82.2 (Aug. 2019), pp. 671–679. ISSN: 1522-2594. DOI: 10.1002/mrm.27757.

[58] Arvin Arani et al. “Measuring the effects of aging and sex on regional brain stiffness with MR elastography in healthy older adults”. In: *NeuroImage* 111 (May 2015), pp. 59–64. ISSN: 1053-8119. DOI: 10.1016/j.neuroimage.2015.02.016. URL: https://www.sciencedirect.com/science/article/pii/S1053811915001172 (visited on 03/14/2024).

[59] Tomohiro Takamura et al. “Influence of Age on Global and Regional Brain Stiffness in Young and Middle-Aged Adults”. en. In: *Journal of Magnetic Resonance Imaging* 51.3 (2020). _eprint: https://onlinelibrary.wiley.com/doi/pdf/10.1002/jmri.26881, pp. 727–733. ISSN: 1522-2586. DOI: 10.1002/jmri.26881. URL: https://onlinelibrary.wiley.com/doi/abs/10.1002/jmri.26881 (visited on 03/14/2024).

[60] Curtis L. Johnson et al. “Local mechanical properties of white matter structures in the human brain”. eng. In: *NeuroImage* 79 (Oct. 2013), pp. 145–152. ISSN: 1095-9572. DOI: 10.1016/j.neuroimage.2013.04.089.

[61] Kevin Linka et al. “Unraveling the Local Relation Between Tissue Composition and Human Brain Mechanics Through Machine Learning”. eng. In: *Frontiers in Bioengineering and Biotechnology* 9 (2021), p. 704738. ISSN: 2296-4185. DOI: 10.3389/fbioe.2021.704738.

[62] Johannes Weickenmeier et al. “The mechanical importance of myelination in the central nervous system”. eng. In: *Journal of the Mechanical Behavior of Biomedical Materials* 76 (Dec. 2017), pp. 119–124. ISSN: 1878-0180. DOI: 10.1016/j.jmbbm.2017.04.017.

[63] S. Budday et al. “Mechanical characterization of human brain tissue”. eng. In: *Acta Biomaterialia* 48 (Jan. 2017), pp. 319–340. ISSN: 1878-7568. DOI: 10.1016/j.actbio.2016.10.036.

[64] Jing Guo et al. “Towards an Elastographic Atlas of Brain Anatomy”. en. In: *PLOS ONE* 8.8 (Aug. 2013). Publisher: Public Library of Science, e71807. ISSN: 1932-6203. DOI: 10.1371/journal.pone.0071807. URL: https://journals.plos.org/plosone/article?id=10.1371/journal.pone.0071807 (visited on 02/29/2024).

[65] Kaspar-Josche Streitberger et al. “In vivo viscoelastic properties of the brain in normal pressure hydrocephalus”. eng. In: *NMR in biomedicine* 24.4 (May 2011), pp. 385–392. ISSN: 1099-1492. DOI: 10.1002/nbm.1602.

[66] Florian Baptist Freimann et al. “Alteration of brain viscoelasticity after shunt treatment in normal pressure hydrocephalus”. eng. In: *Neuroradiology* 54.3 (Mar. 2012), pp. 189–196. ISSN: 1432-1920. DOI: 10.1007/s00234-011-0871-1.

[67] N. Fattahi et al. “MR Elastography Demonstrates Increased Brain Stiffness in Normal Pressure Hydrocephalus”. eng. In: *AJNR. American journal of neuroradiology* 37.3 (Mar. 2016), pp. 462–467. ISSN: 1936-959X. DOI: 10.3174/ajnr.A4560.

[68] Matthew C. Murphy et al. “Identification of Normal Pressure Hydrocephalus by Disease-Specific Patterns of Brain Stiffness and Damping Ratio”. eng. In: *Investigative Radiology* 55.4 (Apr. 2020), pp. 200–208. ISSN: 1536-0210. DOI: 10.1097/RLI.0000000000000630.

[69] F. H. Sklar et al. “Brain elasticity changes with ventriculomegaly”. eng. In: *Journal of Neurosurgery* 53.2 (Aug. 1980), pp. 173–179. ISSN: 0022-3085. DOI: 10.3171/jns.1980.53.2.0173.

[70] M. E. Wagshul et al. “MR Elastography demonstrates reduced white matter shear stiffness in early-onset hydrocephalus”. eng. In: *NeuroImage. Clinical* 30 (2021), p. 102579. ISSN: 2213-1582. DOI: 10.1016/j.nicl.2021.102579.

[71] Kaspar-Josche Streitberger et al. “Brain viscoelasticity alteration in chronic-progressive multiple sclerosis”. eng. In: *PloS One* 7.1 (2012), e29888. ISSN: 1932-6203. DOI: 10.1371/journal.pone.0029888.

[72] Chloe M. Hall, Emad Moeendarbary, and Graham K. Sheridan. “Mechanobiology of the brain in ageing and Alzheimer’s disease”. eng. In: *The European Journal of Neuroscience* 53.12 (June 2021), pp. 3851–3878. ISSN: 1460-9568. DOI: 10.1111/ejn.14766.

[73] Xue Li et al. “Perineuronal Nets in the CNS: Architects of Memory and Potential Therapeutic Target in Neuropsychiatric Disorders”. In: *International Journal of Molecular Sciences* 25.6 (Mar. 2024), p. 3412. ISSN: 1422-0067. DOI: 10.3390/ijms25063412. URL: https://www.ncbi.nlm.nih.gov/pmc/articles/PMC10970535/ (visited on 08/25/2024).

[74] Matthew C. Murphy et al. “Regional brain stiffness changes across the Alzheimer’s disease spectrum”. en. In: *NeuroImage : Clinical* 10 (2016). Publisher: Elsevier, p. 283. DOI: 10.1016/j.nicl.2015.12.007. URL: https://www.ncbi.nlm.nih.gov/pmc/articles/PMC4724025/ (visited on 03/05/2024).

[75] Axel Lipp et al. “Progressive supranuclear palsy and idiopathic Parkinson’s disease are associated with local reduction of in vivo brain viscoelasticity”. eng. In: *European Radiology* 28.8 (Aug. 2018), pp. 3347–3354. ISSN: 1432-1084. DOI: 10.1007/s00330-017-5269-y.

[76] D. M. McGrath et al. “Evaluation of Wave Delivery Methodology for Brain MRE: Insights from Computational Simulations”. en. In: *Magnetic Resonance in Medicine* 78.1 (July 2017). Number: 1 Publisher: Wiley, pp. 341–356. ISSN: 0740-3194. URL: http://dx.doi.org/10.1002/mrm.26333 (visited on 01/30/2024).

[77] Yann LeCun, Yoshua Bengio, and Geoffrey Hinton. “Deep learning”. en. In: *Nature* 521.7553 (May 2015). Publisher: Nature Publishing Group, pp. 436–444. ISSN: 1476-4687. DOI: 10.1038/nature14539. URL: https://www.nature.com/articles/nature14539 (visited on 03/13/2024).

[78] Razvan Pascanu, Tomas Mikolov, and Yoshua Bengio. “On the difficulty of training recurrent neural networks”. en. In: *Proceedings of the 30th International Conference on*

Machine Learning. ISSN: 1938-7228. PMLR, May 2013, pp. 1310–1318. URL: https://proceedings.mlr.press/v28/pascanu13.html (visited on 03/13/2024).

[79] Tomasz Szandała. "Review and Comparison of Commonly Used Activation Functions for Deep Neural Networks". en. In: *Bio-inspired Neurocomputing*. Ed. by Akash Kumar Bhoi et al. Singapore: Springer, 2021, pp. 203–224. ISBN: 9789811554957. DOI: 10.1007/978-981-15-5495-7_11. URL: https://doi.org/10.1007/978-981-15-5495-7_11 (visited on 03/13/2024).

[80] Diederik P. Kingma and Jimmy Ba. *Adam: A Method for Stochastic Optimization*. arXiv:1412.6980 [cs]. Jan. 2017. DOI: 10.48550/arXiv.1412.6980. URL: http://arxiv.org/abs/1412.6980 (visited on 03/13/2024).

[81] Ehsan Haghighat et al. "A physics-informed deep learning framework for inversion and surrogate modeling in solid mechanics". In: *Computer Methods in Applied Mechanics and Engineering* 379 (June 2021), p. 113741. ISSN: 0045-7825. DOI: 10.1016/j.cma.2021.113741. URL: https://www.sciencedirect.com/science/article/pii/S0045782521000773 (visited on 03/11/2024).

[82] *Smoothing and Differentiation of Data by Simplified Least Squares Procedures. | Analytical Chemistry*. URL: https://pubs.acs.org/doi/10.1021/ac60214a047 (visited on 02/27/2024).

[83] Phillip R. Perriñez et al. "Magnetic Resonance Poroelastography: An Algorithm for Estimating the Mechanical Properties of Fluid-Saturated Soft Tissues". In: *IEEE transactions on medical imaging* 29.3 (Mar. 2010), pp. 746–755. ISSN: 0278-0062. DOI: 10.1109/TMI.2009.2035309. URL: https://www.ncbi.nlm.nih.gov/pmc/articles/PMC2865251/ (visited on 03/02/2024).

[84] *Suitability of poroelastic and viscoelastic mechanical models for high and low frequency MR elastography - PMC*. URL: https://www.ncbi.nlm.nih.gov/pmc/articles/PMC4312344/ (visited on 03/02/2024).

[85] *Biomedical Instrumentation: Technology and Applications*. URL: https://www.mhprofessional.com/biomedical-instrumentation-technology-and-applications-9780071447843-usa (visited on 01/30/2024).

[86] E. E. Van Houten et al. "An overlapping subzone technique for MR-based elastic property reconstruction". eng. In: *Magnetic Resonance in Medicine* 42.4 (Oct. 1999), pp. 779–786. ISSN: 0740-3194. DOI: 10.1002/(sici)1522-2594(199910)42:4<779::aid-mrm21>3.0.co;2-z.

[87] H. Knutsson, C.-F. Westin, and G. Granlund. “Local multiscale frequency and bandwidth estimation”. In: *Proceedings of 1st International Conference on Image Processing*. Vol. 1. Nov. 1994, 36–40 vol.1. DOI: 10.1109/ICIP.1994.413270. URL: https://ieeexplore.ieee.org/document/413270 (visited on 03/02/2024).

[88] Sebastian Papazoglou et al. “Multifrequency inversion in magnetic resonance elastography”. en. In: *Physics in Medicine & Biology* 57.8 (Mar. 2012). Publisher: IOP Publishing, p. 2329. ISSN: 0031-9155. DOI: 10.1088/0031-9155/57/8/2329. URL: https://dx.doi.org/10.1088/0031-9155/57/8/2329 (visited on 03/01/2024).

[89] Bo Ni and Huajian Gao. “A deep learning approach to the inverse problem of modulus identification in elasticity”. en. In: *MRS Bulletin* (Sept. 2020). Publisher: Cambridge University Press, pp. 1–7. ISSN: 0883-7694, 1938-1425. DOI: 10.1557/mrs.2020.231. URL: https://www.cambridge.org/core/journals/mrs-bulletin/article/deep-learning-approach-to-the-inverse-problem-of-modulus-identification-in-elasticity/54F6A432DA748815F70A68F42070D59A (visited on 01/30/2024).

[90] Ligin Solamen, Yipeng Shi, and Justice Amoh. *Dual Objective Approach Using A Convolutional Neural Network for Magnetic Resonance Elastography*. arXiv:1812.00441 [physics, stat]. Dec. 2018. DOI: 10.48550/arXiv.1812.00441. URL: http://arxiv.org/abs/1812.00441 (visited on 02/05/2024).

[91] Brian L. Pollack et al. “Deep Learning Prediction of Voxel-Level Liver Stiffness in Patients with Nonalcoholic Fatty Liver Disease”. eng. In: *Radiology. Artificial Intelligence* 3.6 (Nov. 2021), e200274. ISSN: 2638-6100. DOI: 10.1148/ryai.2021200274.

[92] Arunabha M. Roy et al. “Deep learning-accelerated computational framework based on Physics Informed Neural Network for the solution of linear elasticity”. eng. In: *Neural Networks: The Official Journal of the International Neural Network Society* 162 (May 2023), pp. 472–489. ISSN: 1879-2782. DOI: 10.1016/j.neunet.2023.03.014.

[93] Nils Thuerey et al. *Physics-based Deep Learning*. arXiv:2109.05237 [physics]. Apr. 2022. DOI: 10.48550/arXiv.2109.05237. URL: http://arxiv.org/abs/2109.05237 (visited on 01/30/2024).

[94] Xinhai Chen et al. “Transfer learning for deep neural network-based partial differential equations solving”. In: *Advances in Aerodynamics* 3.1 (Dec. 2021), p. 36. ISSN: 2524-6992. DOI: 10.1186/s42774-021-00094-7. URL: https://doi.org/10.1186/s42774-021-00094-7 (visited on 07/31/2024).

[95] Abdul Hannan Mustajab et al. *Physics-Informed Neural Networks for High-Frequency and Multi-Scale Problems using Transfer Learning*. arXiv:2401.02810 [cs, math]. Jan. 2024. DOI: 10.48550/arXiv.2401.02810. URL: http://arxiv.org/abs/2401.02810 (visited on 04/24/2024).

[96] Chen Xu et al. "Transfer learning based physics-informed neural networks for solving inverse problems in engineering structures under different loading scenarios". In: *Computer Methods in Applied Mechanics and Engineering* 405 (Feb. 2023). arXiv:2205.07731 [cs], p. 115852. ISSN: 00457825. DOI: 10.1016/j.cma.2022.115852. URL: http://arxiv.org/abs/2205.07731 (visited on 04/24/2024).

[97] Enrui Zhang, Minglang Yin, and George Em Karniadakis. *Physics-Informed Neural Networks for Nonhomogeneous Material Identification in Elasticity Imaging*. arXiv:2009.04525 [cond-mat]. Sept. 2020. DOI: 10.48550/arXiv.2009.04525. URL: http://arxiv.org/abs/2009.04525 (visited on 03/11/2024).

[98] *Physics-informed neural networks: A deep learning framework for solving forward and inverse problems involving nonlinear partial differential equations - ScienceDirect*. URL: https://www.sciencedirect.com/science/article/abs/pii/S0021999118307125 (visited on 02/29/2024).

[99] Jonathan M. Scott et al. "Impact of material homogeneity assumption on cortical stiffness estimates by MR elastography". eng. In: *Magnetic Resonance in Medicine* 88.2 (Aug. 2022), pp. 916–929. ISSN: 1522-2594. DOI: 10.1002/mrm.29226.

[100] Eric Barnhill et al. "Heterogeneous Multifrequency Direct Inversion (HMDI) for magnetic resonance elastography with application to a clinical brain exam". eng. In: *Medical Image Analysis* 46 (May 2018), pp. 180–188. ISSN: 1361-8423. DOI: 10.1016/j.media.2018.03.003.

[101] Vincent Sitzmann et al. *Implicit Neural Representations with Periodic Activation Functions*. arXiv:2006.09661 [cs, eess]. June 2020. DOI: 10.48550/arXiv.2006.09661. URL: http://arxiv.org/abs/2006.09661 (visited on 07/28/2024).

[102] Adam Paszke et al. *Automatic differentiation in pytorch.(2017)*. 2017. URL: https://scholar.google.com/scholar?cluster=11579329835932062709&hl=en&oi=scholarr (visited on 08/20/2024).

[103] Lu Lu et al. "DeepXDE: A deep learning library for solving differential equations". In: *SIAM Review* 63.1 (Jan. 2021). arXiv:1907.04502 [physics, stat], pp. 208–228. ISSN: 0036-1445, 1095-7200. DOI: 10.1137/19M1274067. URL: http://arxiv.org/abs/1907.04502 (visited on 08/20/2024).

[104] Abraham. Savitzky and M. J. E. Golay. “Smoothing and Differentiation of Data by Simplified Least Squares Procedures.” In: *Analytical Chemistry* 36.8 (July 1964). Publisher: American Chemical Society, pp. 1627–1639. ISSN: 0003-2700. DOI: 10.1021/ac60214a047. URL: https://doi.org/10.1021/ac60214a047 (visited on 07/30/2024).

[105] Matthew W. Scroggs et al. “Construction of arbitrary order finite element degree-of-freedom maps on polygonal and polyhedral cell meshes”. In: *ACM Transactions on Mathematical Software* 48.2 (June 2022). arXiv:2102.11901 [cs, math], pp. 1–23. ISSN: 0098-3500, 1557-7295. DOI: 10.1145/3524456. URL: http://arxiv.org/abs/2102.11901 (visited on 02/27/2024).

[106] Susanne C. Brenner and L. Ridgway Scott. *The Mathematical Theory of Finite Element Methods*. Ed. by J. E. Marsden, L. Sirovich, and S. S. Antman. Vol. 15. Texts in Applied Mathematics. New York, NY: Springer, 2008. ISBN: 978-0-387-75933-3 978-0-387-75934-0. DOI: 10.1007/978-0-387-75934-0. URL: http://link.springer.com/10.1007/978-0-387-75934-0 (visited on 08/22/2024).

[107] Heiko Tzschätzsch et al. “Tomoelastography by multifrequency wave number recovery from time-harmonic propagating shear waves”. eng. In: *Medical Image Analysis* 30 (May 2016), pp. 1–10. ISSN: 1361-8423. DOI: 10.1016/j.media.2016.01.001.

[108] Umme Sara, Morium Akter, and Mohammad Shorif Uddin. “Image Quality Assessment through FSIM, SSIM, MSE and PSNR—A Comparative Study”. en. In: *Journal of Computer and Communications* 7.3 (Mar. 2019). Number: 3 Publisher: Scientific Research Publishing, pp. 8–18. DOI: 10.4236/jcc.2019.73002. URL: https://www.scirp.org/journal/paperinformation?paperid=90911 (visited on 08/25/2024).

[109] Alain Horé and Djemel Ziou. “Image Quality Metrics: PSNR vs. SSIM”. In: *2010 20th International Conference on Pattern Recognition*. ISSN: 1051-4651. Aug. 2010, pp. 2366–2369. DOI: 10.1109/ICPR.2010.579. URL: https://ieeexplore.ieee.org/abstract/document/5596999 (visited on 08/25/2024).

[110] PV Bayly et al. “MR imaging of human brain mechanics in vivo: New measurements to facilitate the development of computational models of brain injury”. In: *Annals of biomedical engineering* 49.10 (Oct. 2021), pp. 2677–2692. ISSN: 0090-6964. DOI: 10.1007/s10439-021-02820-0. URL: https://www.ncbi.nlm.nih.gov/pmc/articles/PMC8516723/ (visited on 01/30/2024).

[111] C. L. Johnson et al. “Brain MR elastography with multiband excitation and nonlinear motion-induced phase error correction”. In: Proc. Intl. Soc. Mag. Reson. Med. 24 (2016) ().

[112] M. D. J. McGarry et al. “Multiresolution MR elastography using nonlinear inversion”. In: *Medical Physics* 39.10 (Oct. 2012), pp. 6388–6396. ISSN: 0094-2405. DOI: 10.1118/1.4754649. URL: https://www.ncbi.nlm.nih.gov/pmc/articles/PMC3477197/ (visited on 07/27/2024).

[113] Mark F. Horstemeyer, Matthew B. Panzer, and Raj K. Prabhu. “State-of-the-Art Modeling and Simulation of the Brain’s Response to Mechanical Loads”. en. In: *Annals of Biomedical Engineering* 47.9 (Sept. 2019), pp. 1829–1831. ISSN: 1573-9686. DOI: 10.1007/s10439-019-02351-9. URL: https://doi.org/10.1007/s10439-019-02351-9 (visited on 08/22/2024).

[114] Erik G. Takhounts et al. “Investigation of traumatic brain injuries using the next generation of simulated injury monitor (SIMon) finite element head model”. eng. In: *Stapp Car Crash Journal* 52 (Nov. 2008), pp. 1–31. ISSN: 1532-8546. DOI: 10.4271/2008-22-0001.

[115] Lili He et al. “Machine Learning Prediction of Liver Stiffness Using Clinical and T2-Weighted MRI Radiomic Data”. eng. In: *AJR. American journal of roentgenology* 213.3 (Sept. 2019), pp. 592–601. ISSN: 1546-3141. DOI: 10.2214/AJR.19.21082.

[116] Abigail L. Hong et al. “MRI-derived bone porosity index correlates to bone composition and mechanical stiffness”. In: *Bone Reports* 11 (June 2019), p. 100213. ISSN: 2352-1872. DOI: 10.1016/j.bonr.2019.100213. URL: https://www.ncbi.nlm.nih.gov/pmc/articles/PMC6660551/ (visited on 08/19/2024).

[117] Stefan Hetzer et al. “Perfusion alters stiffness of deep gray matter”. eng. In: *Journal of Cerebral Blood Flow and Metabolism: Official Journal of the International Society of Cerebral Blood Flow and Metabolism* 38.1 (Jan. 2018), pp. 116–125. ISSN: 1559-7016. DOI: 10.1177/0271678X17691530.

[118] M. D. J. McGarry et al. “Suitability of poroelastic and viscoelastic mechanical models for high and low frequency MR elastography”. In: *Medical Physics* 42.2 (Feb. 2015), pp. 947–957. ISSN: 0094-2405. DOI: 10.1118/1.4905048. URL: https://www.ncbi.nlm.nih.gov/pmc/articles/PMC4312344/ (visited on 07/31/2024).